Hybrid Quantum Systems in Cavity QED and Optomechanics

By

Daniel Lombardo

A thesis submitted to Macquarie University
for the degree of Master of Research
Department of Physics
March 2015

MACQUARIE UNIVERSITY
SYDNEY ~ AUSTRALIA

Typeset in LaTeX 2_ε.

Except where acknowledged in the customary manner, the material presented in this thesis is, to the best of my knowledge, original and has not been submitted in whole or part for a degree in any university.

Daniel Lombardo

Acknowledgements

Over the past year I have thoroughly enjoyed working on not only this thesis but other work which has been offered to me by many of the eQus personnel. Given the short time interval that was allowed to complete this work, I never imagined I would have made the progress that I have. For the most part the progress I have made throughout the year would not have been possible without the continuous guidance and support of my supervisor Jason Twamley. Even at extremely inconvenient times Jason continued to keep in contact with not only me but the whole department. I am very appreciative for the time he has spent making sure that my work made sense and continually thinking up new ideas to either improve current work or establish new projects. Thank you Jason! I would also like to thank James Cresser who has always kept his door open for arbitrary questions, happily taking time out of his day to both decipher and answer my questions honestly.

Throughout the year I was given the opportunity to both join Thomas Volz and his group in their weekly meetings and work in parallel with them on projects outside of this thesis. I am very thankful to Thomas for giving me this opportunity as it has not only given me a preview of the experimental side of research but encouraged me to learn concepts which I would have otherwise never known. In addition to Thomas I would also like to thank Benjamin Besga and Carlo Bradac for taking the time to discuss a range different problems, teaching me a lot of physics in the process. Other opportunities were also presented to me by Keyu Xia, Peter Rhode and Keith Motes, who have invited me into projects on several occasions and have happily shared their knowledge with me. To be so kindly invited into projects significantly improved my enthusiasm and confidence towards research. Thank you Keyu, Peter and Keith!

Most importantly, I would like to thank my family. Without the unconditional support of my father, Corrado, I would have never made it this far. Words cannot describe how thankful and appreciative I am for everything he has done for me. My brother, Paul, and partner, Jessica, have also significantly helped in the development of this thesis as they both took the time to proof read it, despite having no background in physics. Thank you Dad, Paul and Jessica, I look forward to spending many more beach filled summers together!

Last but not least I would like to thank all of my friends in both the department of physics and the department of mathematics. Without a group of friendly and kind people to talk and laugh with, day to day life would have been much less enjoyable.

List of Publications

- Daniel Lombardo and Jason Twamley. *Optical-Coupling of distant spins via collective enhancement in multi-mode whispering gallery resonators.* Optics Express, **23**, 2945 (2015).
- Daniel Lombardo and Jason Twamley. *Deterministic Creation of Macroscopic Cat States.* (submitted to Scientific Reports)

Abstract

Quantum mechanics has been demonstrated on many experimental platforms which include super conducting cavities, trapped ions and atomic systems. However, each of these platforms have attributes which make them suitable under certain conditions and applicable to only specific tasks. By combining these quantum systems it is possible to create hybrids which benefit from each of the individual advantages of the comprising subsystems. Such combined systems are referred to as hybrid quantum systems and can be used to reach regimes, observe behaviours and results which are otherwise impossible to achieve. In this thesis two hybrid quantum systems are studied with the intentions of both creating a practical quantum system for applications in quantum technologies and creating macroscopic quantum states for fundamental studies of quantum mechanics.

The first hybrid quantum system which is studied focuses on light-matter interactions between spins and an optical resonator. Achieving strong light-matter interactions is one of the focal points of modern quantum mechanics as such strengths not only allow for the transportation of quantum information via photons but also for the generation of entangled quantum states. These are traits that are intensively sought after in almost every field of quantum science for both fundamental studies and the development of practical quantum technologies. Fabry-Pérot resonators have been most commonly used to study light-matter interactions due to their simplicity and compatibility with many experimental configurations. Here, however, an alternative type of resonator is considered, otherwise referred to as a Whispering Gallery resonator. Such hybrid resonators have more recently become popular due to their potentially more favourable scalability, in comparison with Fabry-Pérot resonators. In particular, this work focuses on the interaction between spins and the Whispering Gallery Modes (WGMs) of a fused silica microsphere with the intention of achieving effective interactions between distant spins. The spherical symmetry of the resonator is utilised to show that such resonators are capable of supporting an ensemble of degenerate optical modes which can result in a collective enhancement to the light-matter interaction strength. It is shown that enhanced interaction strengths on the order of GHz can be achieved, allowing for strong effective interactions to be attained between distant spins. These interaction strengths would

allow for the construction of large arrays of coupled spherical resonators/spins which can be used to create quantum networks, perform quantum simulations of many-body systems and of course, as a platform for quantum computation.

The second hybrid system focuses on the creation of macroscopic quantum states which are analogous to the Schrödinger cat state. The creation of such states is currently one of the most attractive goals in quantum mechanics as they can resemble states which reside at the borders of the classical and quantum worlds, allowing for the study of how quantum states become classical. Despite current technological advances, the largest Schrödinger cat states which have been observed to date still lie within atomic scales. With the intentions of achieving quantum superpositions of macroscopic objects many researchers have directed their attention to the field of optomechanics. Here interactions between light and mechanical oscillators are exploited to concoct schemes in which quantum superpositions of the mechanical oscillator's position can be created. While the creation of cat states can be somewhat guaranteed after entangling the position of the oscillator with a single photon or qubit, creating such states using larger systems requires measurement thus making the creation process probabilistic. In this work a novel, completely deterministic method of macroscopic cat state creation is proposed. Here cat states are created by exploiting properties in the optomechanical Membrane In The Middle model where a mechanical oscillator, or membrane, is placed within a Fabry-Pérot cavity. It is shown that by controlling the membrane's opacity its position can be driven to achieve large spatial displacements. This process is used to deterministically grow the spatial extent of a cat state of the membrane's position. It is found that by using a Bose-Einstein condensate as a membrane high fidelity cat states with spatial separations of up to $\sim$300 nm can be achieved. These cat states are significantly larger than any which have been observed to date and are created in a completely deterministic manner.

Contents

Abbreviations

QED ..... Quantum Electrodynamics.

cQED ..... Cavity Quantum Electrodynamics.

WGM ..... Whispering Gallery Mode.

JC ..... Jaynes-Cummings.

TC ..... Tavis-Cummings.

MM ..... Multi-Mode.

MMTC ..... Multi-Mode Tavis-Cummings.

VSH ..... Vector Spherical Harmonics.

TE ..... Transverse Electric.

TM ..... Transverse Magnetic.

CW ..... Clockwise.

CCW ..... Counter-Clockwise.

ZPL ..... Zero-Phonon Line.

ND ..... Nanodiamond.

NV ..... Nitrogen-Vacancy.

MITM ..... Membrane In The Middle.

BEC ..... Bose-Einstein Condensate.

EC ..... Entangled Coherent.

ESC ..... Entangled Squeezed Coherent.

CSS..... Coherent Superposition State.

MLJC ..... Multi-Level Jaynes-Cummings.

EOP ..... Electro-Optic Plate.

Chapter 1

Introduction

Quantum mechanics was originally developed to explain otherwise unexplainable phenomena such as the black body spectrum, wave particle duality and the nature of atomic transitions. However, with it came completely bizarre and unavoidable theoretical predictions. Until more recent decades these predictions were somewhat ignored due to their completely counter intuitive nature. These intrinsic properties of the theory are now the focal point of quantum science. Originally thought to be inapplicable to any practical applications, such quantum mechanical effects are now intensively sought after to develop the technologies of the future.

The seemingly unnatural phenomena predicted by quantum theory include quantum superposition, entanglement, tunnelling and teleportation. These phenomena form the basis for the potential improvements quantum technology may be capable of achieving over current technologies. At present, practical implementation of these phenomena has yet to be achieved, however, over the past few decades remarkable steps have been made towards the creation, observation and implementation of such quantum mechanical effects. Theory has also been established underlying many aspects of quantum science, from proposals regarding the creation and observation of such effects to algorithms designed specifically for quantum computation. Currently, at the forefront of quantum science, researchers are searching for methods to construct quantum mechanical systems which can be coherently controlled with high precision and can be readily scaled for practical applications in quantum technologies.

Practical quantum technology will require the efficient implementation of a range of quantum mechanical effects. Depending on the application, these requirements include the ability to generate and manipulate quantum mechanical states, such as superpositions or entangled states, the efficient storage and transportation of quantum information over long distances and the ability to maintain quantum coherence for large system sizes at practical temperatures. There has been significant progress made towards individually reaching the

majority of these goals, such as the storage of quantum information [1–3], long coherence times at room temperatures [4–9] and the transfer of quantum states [10–13]. However, integration of each of these attributes to create practical quantum technologies has yet to be achieved. Focus now lays on the development of hybrid quantum systems to create integrated systems which can be used in practical quantum technologies and to study quantum mechanics on large scales. As discussed above, the beginnings of practical applications of quantum mechanics has been demonstrated, however, each of these achievements require the use of specific quantum systems. These systems each have a unique set of attributes which make them suitable under certain conditions and applicable to only specific tasks. Hybrid quantum systems are systems which are comprised of several quantum mechanical subsystems. By combining several separate quantum systems it is possible to create hybrids which benefit from each of the individual advantages of the comprising subsystems. These hybrid quantum systems may provide the intensively sought after attributes required for the development of both practical quantum technologies and quantum science itself as they can be used to reach regimes, observe behaviours and results which are otherwise impossible to achieve. In this thesis two hybrid quantum systems will be studied with the intention of proposing experimental platforms which can be used either for the construction of practical quantum technologies or to observe quantum mechanical effects on macroscopic scales.

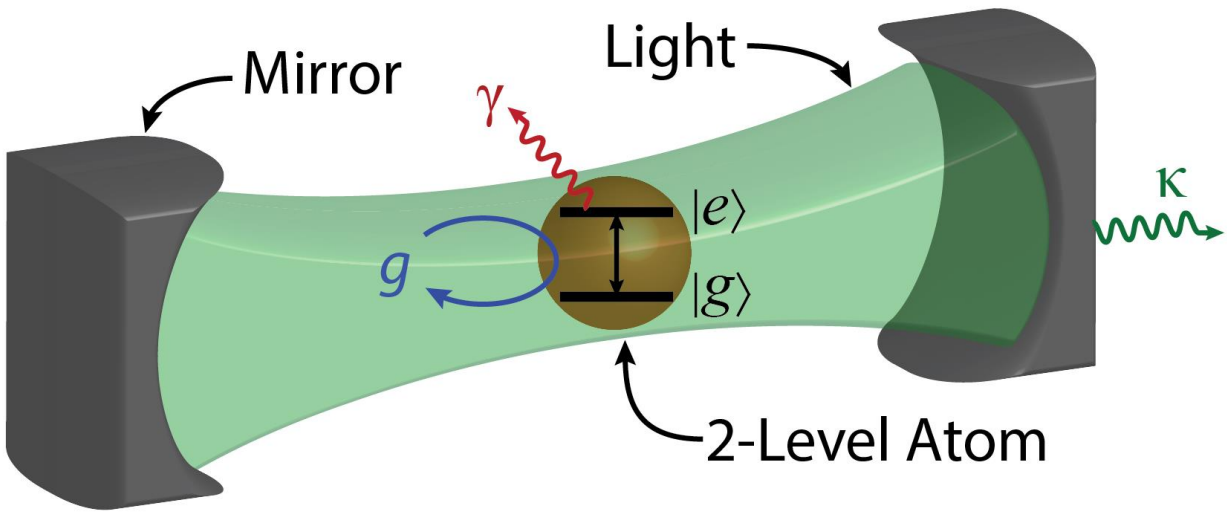

FIGURE 1.1: A Fabry-Pérot type cavity which contains a single 2-level atom. The excited and ground state energy levels of the atom are denoted by $|e\rangle$ and $|g\rangle$ respectively. Leakage of light out of the cavity is described by the loss rate κ and spontaneous emission of light from the atomic excited state into the environment by the rate γ. Interaction between the light and the atom is described by the interaction strength g.

Practical quantum systems - As mentioned above, for practical applications in quantum technologies a quantum system must be capable of creating, maintaining, manipulating and transporting quantum mechanical states. One of the most successful approaches to reaching this set of goals involves the study of light-matter interactions. The basic idea is that light can be used to effectively interact distant quantum systems. This can be interpreted by imagining that the light acts as an 'information bus' which can be used to transport information between the two distant systems. However, to realistically achieve this the strength of the light-matter interactions must be made much stronger than any dissipative effects present in the system, such as the leakage of light into the environment. For this reason the development of quantum systems which are capable of attaining strong light-matter interactions is one of the focal points of modern quantum mechanics as such strengths not only allow for the transportation of quantum information via photons but also for the generation of quantum states. Quantum systems with these capabilities have applications in almost every field of quantum science. To study light-matter interactions light must be confined within the system. This confinement is often achieved through the use of Fabry-Pérot type resonators, or cavities, which are essentially comprised from two opposing mirrors. Light-matter interactions can then be studied by introducing matter into the cavity, see Fig.1.1. Such systems fall into the field of cavity quantum electrodynamics (cQED). The simplest light-matter interaction which can be studied in cQED corresponds to the introduction of single two-level atoms into the cavity. This is because the only interaction that occurs corresponds to either the atom absorbing a photon from the cavity, exciting the atom into its higher energy state, or the emission of a photon from the atom into the cavity, relaxing the atom into its lower energy state. Many experiments have been performed using these types of quantum systems to show that relatively strong light-matter interaction rates can be achieved using optical frequency light [13–18]. Effective interactions between two separate atoms can also be achieved by introducing a second atom into the cavity. With the intention of maximising the distance between the two effectively interacting atoms, the consideration of alternative types of cavities has become increasingly popular. This popularity stems from many advantages such cavities have over the standard Fabry-Pérot type cavity, such as reduced photon leakage and the confinement of light within a smaller volume. These hybrid resonators include photonic crystal cavities and whispering gallery resonators. Of particular interest are whispering gallery resonators. These types of resonators correspond to objects such as disks, toroids and spheres which are capable of confining light via continuous total internal reflections.

The first hybrid quantum system which will be studied in this thesis focuses on achieving strong interactions between distant quantum systems through the use of a spherical

whispering gallery resonator. Here it will be shown that the spherical symmetry of the resonator allows for the achievement of an effective enhancement to the light-matter interaction strength. It is then shown that this enhancement allows for strong interactions to be attained between distant atoms which can be used to fashion large scale quantum networks.

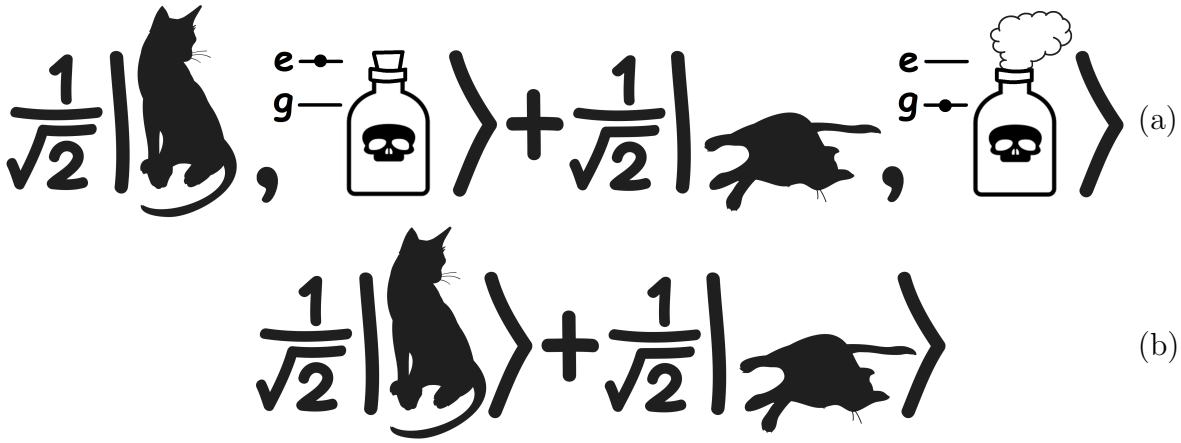

FIGURE 1.2: A depiction of two types of Schrödinger cat states. (a) depicts an entangled state where the cat's fate depends on the state of an atom. The first ket in (a) describes an alive cat while the atom is excited and the poison bottle is closed while the second ket describes a dead cat with the atom in its ground state and the poison bottle opened. The lower image (b) depicts a superposition state where the cat's fate does not depend on any other quantum systems.

Macroscopic quantum states - The quantum mechanical world is typically imagined to lie within nanoscopic length scales where quantum mechanics only effects systems as large as atoms, or ensembles of atoms. While it is true that, to date, such effects have only been observed on these scales, there is currently no fundamental postulate that confines quantum mechanical effects to the nanoscopic realm. The main limitation in the observation of such effects is currently thought to be due to experimentation. For this reason the observation of quantum mechanical effects on much larger scales is currently one of the most attractive goals in quantum science. Such observations would allow researchers to study how quantum mechanical systems become classical and determine whether or not experimentation is the only limitation. One approach that has been commonly made is to create and study quantum states of macroscopic objects. A simple example of this would be to create a quantum state that corresponds to a macroscopic object in a superposition of being located at two completely separate positions at the same time. Of these states the most popular are those analogous to the famous Schrödinger's cat state. The Schrödinger's cat state is an entangled state which describes a cat that has been placed inside a box, with its fate determined by the state of a radioactive particle. Using terms mentioned above, this state can be analogously described by replacing the radioactive particle with a two level atom, see Fig.1.2a. If the

atom is excited, then the cat remains alive, however, if the atom spontaneously emits a photon, the photon is detected causing poison to be released inside the box, killing the cat. Alternately, analogous to the spatial superposition state discussed above, the creation of states that correspond to the cat in a superposition of being both alive and dead at the same time, independent of any other system, is also intensively pursued, see Fig.1.2b. Such superpositions are often referred to as 'cat states'. At present some of the largest states analogous to either of the two types of Schrödinger cat states that have been created correspond to either an entangled spatial superposition of a single atom's position or a superposition of the state of the electromagnetic field inside a cavity [19, 20]. With the intention of creating quantum states of macroscopic objects, many researchers have directed their attention towards the field of optomechanics. This field focuses on the interactions between light and mechanical oscillators, such as Fabry-Pérot type cavities where one of the mirrors can move or cavities which contain a mechanical oscillator. These interactions have been routinely exploited to propose experimental protocols for the creation of macroscopic quantum states [21–29]. However, if the oscillator is entangled with more than a single photon or qubit, cat state creation requires measurements to be made on the system making many of the proposed protocols completely probabilistic.

The second half of this thesis focuses on the proposal of a completely deterministic macroscopic cat state creation protocol through the use of an optomechanical system. The system which will be used corresponds to the placement of a mechanical oscillator into a Fabry-Pérot resonator. This type of system is often referred to as 'Membrane in the Middle' (MITM) where the mechanical oscillator is referred to as the membrane. Here it will be shown that a cat state of a macroscopic membrane's position can be deterministically created and grown by controlling its opacity.

This thesis will be split into two main chapters. The first hybrid quantum system will be discussed in Chapter 2. This chapter will focus on achieving strong interactions between light that is confined within a spherical Whispering Gallery Mode (WGM) resonator and distant two-level atomic systems, or spins. It will be shown that an enhancement to the interaction strength can be achieved by taking advantage of the spherical symmetry of the WGM resonator which can be used to effectively couple distant spins. To do so, this chapter will begin by individually studying the theory which gives rise to enhancement and the physics behind the spherical WGMs. This work will then be combined to perform simulations of the interaction between spins and the WGMs. The second hybrid system will be discussed in Chapter 3. This chapter will focus on the creation of macroscopic superposition states using the MITM setup. Here it will be shown that light-matter interactions can be manipulated to deterministically generate spatial superpositions of a membrane's position.

To do so, this chapter will be separated into several sections, each describing different aspects of the cat state creation protocol. The chapter will be concluded with the proposal for an experimental platform which could be used to realise the proposed protocol and the analysis of simulations.

Chapter 2

Enhanced Optical Coupling in Whispering Gallery Resonators

2.1 Introduction

Achieving strong light-matter interactions, or coupling, has been one of the focal points of modern quantum science for the past four decades. As mentioned above, this regime of interaction has many potential applications in quantum science. More specifically, strong interactions can be applied in single photon nonlinear optics [30–33] , quantum simulations of many body systems [34–38], quantum networks [39–41], quantum repeaters [42], and of course, in quantum computation [43–46]. The current focus is now on engineering quantum systems with the largest possible light-matter interaction strengths. In particular, achieving strong interaction between optical photons and atomic systems has heralded significant interest due to the compatibility with fibres. In cQED, however, achieving strong interaction with optical photons has proven to be extremely experimentally challenging requiring either individual spins and ultra-small cavities or an ensemble of identical spins coupled to larger cavities, see Fig.2.1a and b.

At present, the best results in regard to both the realisation and implementation of strong interactions have been through the use of superconducting qubits and microwave photons in circuit QED based experiments. Here effective interaction of qubits separated by millimetre lengths has been achieved [47–49]. These experiments have been extended to show that simple quantum gates can be efficiently applied to several qubits with high fidelity, providing a promising platform for quantum computation [50–53]. They have also been used to generate quantum states [54] and to demonstrate quantum state teleportation over millimetre lengths [55]. Though, these superconducting qubit systems are limited to

cryogenic temperatures and are not easily scalable for practical use in quantum technology. They also depend on microwave photons which pose difficulties in scalability and integration with current technological infrastructure. Due to the compatibility with current technologies, such as fibres, achieving the above results with optical photons is now being intensively pursued.

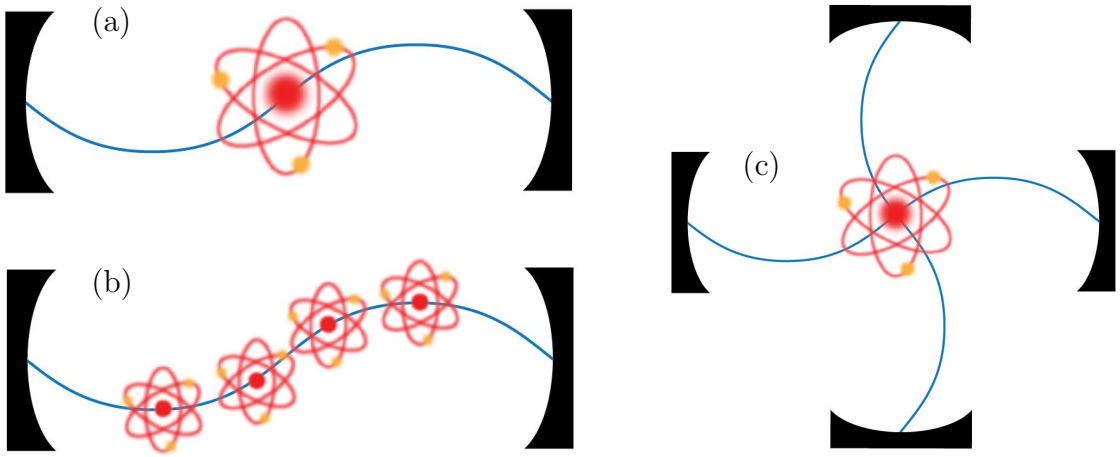

FIGURE 2.1: A simple depiction of the traditional approaches, (a) and (b), to achieving strong light-matter interactions. Here (a) shows a simple Fabry-Pérot cavity where a single atom interacts with a single mode of light while (b) shows many atoms interacting with a single mode of light. An alternative approach to achieving strong interactions is shown in (c) where instead two modes of light interact with a single atom.

The strongest optically based interactions have been demonstrated through the use of cQED based experiments. As a wide variety of spins can be implemented in such systems, these experiments are compatible with a broad band of frequencies. However, achieving strong coupling in these systems is no less of a challenge. As mentioned above, traditional approaches to achieving strong interactions in cQED involve either single spins in tiny cavities (Fig.2.1a), or many identical spins in slightly larger cavities (Fig.2.1b), where Fabry-Pérot type cavities are typically used. The reason that interaction between optical light and many identical spins is considered is because under special conditions a collective enhancement to the interaction strength can be attained, which is proportional to the square root of the number of spins in the system. This enhancement is the result of a constructive quantum interference which stems from the indistinguishability of the spins with respect to the light [56]. To date, only a small number of experiments have successfully observed strong light-matter interactions using these traditional cQED techniques [13, 15–18]. As a consequence, only very few have demonstrated effective interaction of distant spins via optical photons [13]. The largest optical interaction strengths achieved using traditional techniques reside on the scales of MHz for single spins and GHz for ensembles of identical spins [15, 18].

However, while it has been shown that these approaches can be used to demonstrate strong light-matter interactions, they are each extremely experimentally challenging, requiring cryogenic temperatures and very complex system configurations. These demanding conditions make such techniques somewhat problematic to scale up for applications within quantum technologies.

Due to the wide range of applications and the constraints which hinder traditional cQED methods, enormous effort has been directed towards the implementation of hybrid cavities in cQED. In particular, photonic crystal and whispering gallery type cavities have been recently used to achieve relatively strong coupling [57–74]. Whispering gallery resonators have become increasingly popular due to their relatively small mode volumes, large quality factors and their potential to strongly couple distant spins within the same mode [72]. While not yet demonstrated, it has been theorised that with such systems strong interactions and hence quantum entanglement can be achieved between distant spins with less demanding system configurations and temperatures compared to traditional techniques [75–81].

There are three main types of whispering gallery resonators that are most commonly studied in cQED. These include the toroidal, spherical and micro-disk resonators, shown in Fig.2.2. Interaction strengths on sub-GHz scales have been achieved using micro-disc/ring resonators in the infrared band [65], however, for practical applications a lot of work has focused on toroidal and spherical resonators due to their huge quality factors ($Q \sim 10^{10}$) [82, 83], and their capability to reach strong coupling at optical wavelengths. Optical coupling strengths on the order of MHz have been reached between several spins and a single WGM of a slightly oblate microsphere resonator [70], and also between a single spin and a toroidal resonator [67]. In the case of spherical resonators the slight oblateness in the resonator is introduced to ensure that spins interact with only a single WGM [64, 70, 71]. While the optical interaction strengths achieved using these non-traditional cavities have yet to significantly overcome those demonstrated via traditional approaches these hybrid cavities offer slightly less demanding experimental conditions. In this chapter it will be shown that non-oblate spherical resonators can be used to reach interaction strengths orders of magnitude larger than traditional techniques and provide a scalable architecture to fashion large scale strongly-coupled cQED arrays.

To achieve strong interactions using spherical resonators a collective enhancement very similar to that demonstrated with many spins will be considered. As mentioned above, if N spins interact with a single optical cavity mode the interaction strength is enhanced by a factor of $\sqrt{N}$, provided that no "which path" information exists that can be used to differentiate between which spin emits/absorbs into/from the cavity mode. If, instead, a set of N degenerate optical modes interact with a single spin an identical factor of $\sqrt{N}$

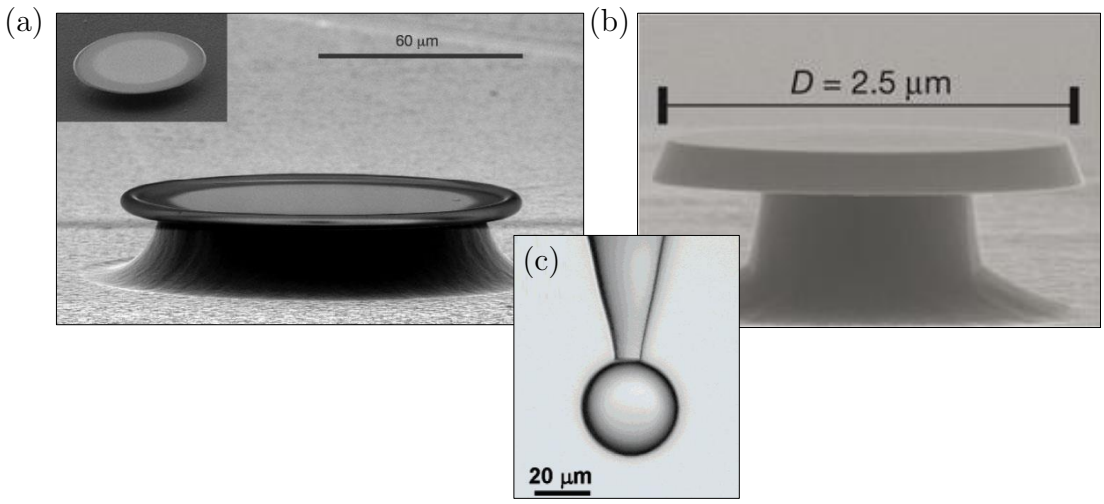

FIGURE 2.2: Published images of three different types of WGM resonators. A SEM image of a toroidal resonator is shown in (a) and that of a micro-disk in (b) [65, 83]. The lower picture, (c), shows an optical image of a slightly deformed microsphere resonator attached to a fibre taper [70]. The resonators shown in (b) and (c) were coupled to spins, while the first, (a), was used to demonstrate the high Q-factors toroidal resonators are capable of achieving.

enhancement to the interaction strength can be achieved, provided that the spin interacts with each of the modes identically to remove any "which path" information. This type of enhancement has been very rarely studied and in fact demonstrated only once where it was shown that by considering the spatial cavity mode profile it was possible to engineer $N \leq 5$ near-degenerate cavity modes, yielding only a minor collective enhancement [84–87]. The difficulty in demonstrating this type of enhancement stems from the experimental limitations in creating degenerate multi-mode systems using traditional Fabry-Pérot cavities. The largest number of modes achievable using Fabry-Pérot type cavities is essentially two. This is because, to ensure that each of the modes are orthogonal and intersect the spin, introduction of more than two cavities requires increasing the size of each cavity, see Fig.2.1c, in turn significantly reducing the overall interaction strength. It will be shown in this chapter that a particular subset of the WGMs in spherical resonators form an excellent platform for the implementation of a multi-mode system, where the number of modes can range from tens to thousands, depending on the sphere's size. The proposed system is shown in Fig.2.3 where the spins are located at the antipodes of the spherical resonator and interact identically with an ensemble of WGMs. These modes correspond to rotated fundamental WGMs, which will be discussed further in Sections 2.3.1.2 and 2.3.3. It will be shown that this system is capable of achieving strong effective interactions between two distant spins which are separated by 66 μm and provides a scalable and experimentally accessible platform for application in quantum technologies.

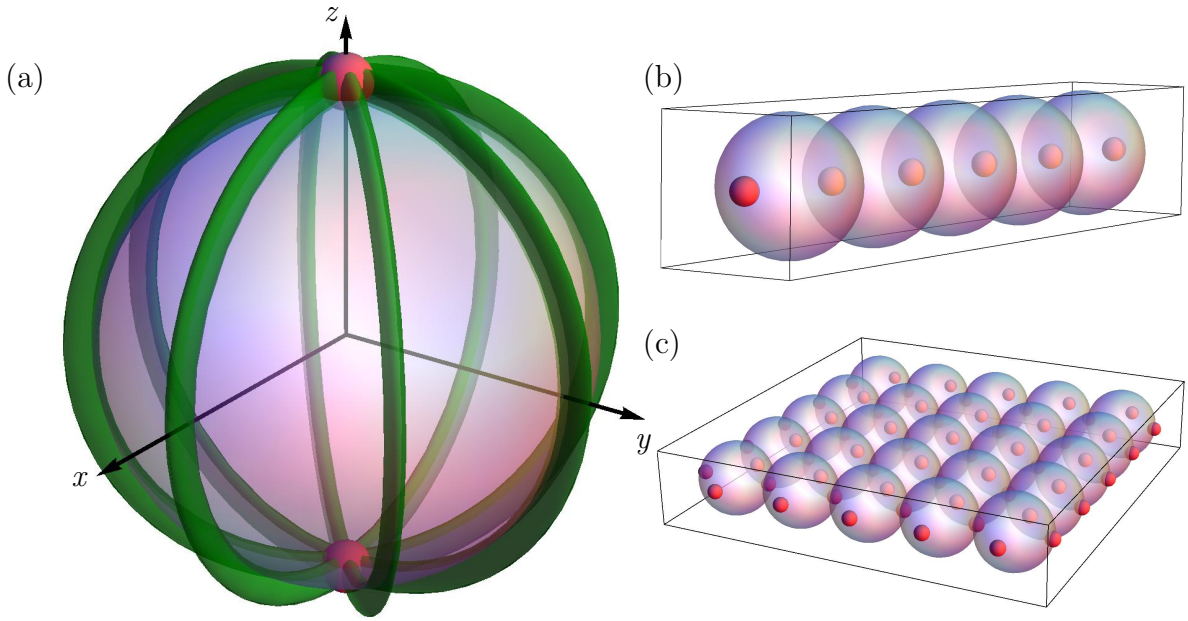

Figure 2.3: (a) A spherical resonator supporting many degenerate rotated WGMs (green tubes) coupled to two antipodal spins (red spheres) and (b) a depiction of the extension of the model into one and (c) two dimensional arrays.

This chapter will be split into four sections. The first will focus on studying the multi-mode system to assure that a factor of $\sqrt{N}$ enhancement can be achieved. To do so, the multi-mode system will be compared against the thoroughly studied multi-spin system. In this section it will also be shown that a further enhancement can be achieved by considering both multiple spins and multiple modes and the dynamics of a single excitation will be solved for. The next section of this chapter will focus on the physics behind WGMs in spherical resonators. Expressions for the electric fields will be derived and studied for each of the rotated fundamental WGMs and the number of such modes which can be sustained by the spherical resonator will be calculated. Section 2.3 will focus on the nature of the interactions between a single spin and the ensemble of WGMs. In this section it will be determined whether or not a constructive quantum interference can be achieved yielding a useful collective enhancement. The final section of this chapter will provide numerical simulations of the dynamics of several different systems, including a single spin interacting with many modes, two antipodal spins effectively interacting with one another via the modes, and clusters of antipodal spins effectively interacting with one another.

2.2 The Enhanced Jaynes-Cummings Model

In this section several cQED systems will be considered to study the effects that constructive quantum interference can have on the light-matter interaction strength. The most simple model in cQED will first be introduced briefly to establish some foundations. Two separate extensions of this model will then be focused on where it will be shown that an effective enhancement to the interaction strength can be achieved. These extensions correspond to the introduction of either many spins or many modes into the system. One final extension will then be studied which corresponds to a system comprised from an ensemble of spins and cavity modes. In the first three sections the dynamics of the system will be solved with no consideration of dissipative effects. These dissipative effects will then be incorporated in the final section, where the most general, multi-spin multi-mode, system will be studied.

2.2.1 The Jaynes-Cummings Model

Aside from an empty cavity the simplest system in cQED involves a single two-level atom, or spin, confined within a cavity containing at least a single photon. The Hamiltonian of such a system can be expressed as the sum of three separate energies, $\hat{H}_a$, the self energy of the spin, $\hat{H}_M$, the self energy of the cavity mode and $\hat{H}_I$ the interaction energy. The self energy terms are given by,

$$\hat{H}_a = \frac{\hbar}{2}\omega_a\hat{\sigma}_z, \tag{2.1}$$

$$\hat{H}_M = \hbar\omega_c\hat{a}^\dagger\hat{a}, \tag{2.2}$$

where $\hat{\sigma}_z = \hat{\sigma}_{ee} - \hat{\sigma}_{gg} = |e\rangle\langle e| - |g\rangle\langle g|$, $\hat{a}^\dagger(\hat{a})$ are the creation(annihilation) operators associated to the mode and ω_a/ω_c the spin/cavity resonance frequencies. Calculation of the interaction term, however, is not as straight forward, requiring several approximations. It is the electric dipole interaction which produces the coupling between the spin and the cavity mode. This means that $\hat{H}_I$ corresponds to dipole interaction energy,

$$\hat{H}_I = -\hat{\mathbf{d}}\cdot\hat{\mathbf{E}}, \tag{2.3}$$

where $\hat{\mathbf{d}}$ is the dipole operator of the spin and $\hat{\mathbf{E}}$ the electric field operator of the cavity mode. By assuming the cavity is a box of volume V the electric field can be quantised giving,

$$\hat{\mathbf{E}} = i\mathbf{E}_0\left(\hat{a}e^{i\mathbf{k}\cdot\mathbf{r}} - \hat{a}^\dagger e^{-i\mathbf{k}\cdot\mathbf{r}}\right), \tag{2.4}$$

where $\mathbf{k}$ is the wavevector of the field, $\mathbf{r}$ the position vector and,

$$\mathbf{E}_0 = \sqrt{\frac{\hbar\omega_c}{2\epsilon_0 V}}\hat{e}, \tag{2.5}$$

for an electric field directed along $\hat{e}$ [88]. The interaction term, $\hat{H}_I$, can be reduced by making the dipole approximation, $e^{i\mathbf{k}\cdot\mathbf{r}} \approx 1$, then conveniently placing the identity operator, $\hat{I} = |e\rangle\langle e| + |g\rangle\langle g|$, around $\hat{\mathbf{d}}$,

$$\hat{H}_I = -\Big(|e\rangle\langle e|\hat{\mathbf{d}}|g\rangle\langle g| + |g\rangle\langle g|\hat{\mathbf{d}}|e\rangle\langle e|\Big) \cdot i\mathbf{E}_0\left(\hat{a} - \hat{a}^\dagger\right), \tag{2.6}$$

since $\langle e|\hat{\mathbf{d}}|e\rangle = \langle g|\hat{\mathbf{d}}|g\rangle = 0$ [89]. Introduction of the atomic raising and lowering operators, $\hat{\sigma}_+ = |e\rangle\langle g|$ and $\hat{\sigma}_- = |g\rangle\langle e|$ and relabelling the dipole operator matrix elements as $\mathbf{d}_{ge} = \frac{i}{\hbar}\langle g|\hat{\mathbf{d}}|e\rangle$ and $\mathbf{d}_{eg} = \mathbf{d}_{ge}^*$ allows Eq.(2.6) to be more neatly written as,

$$\hat{H}_I = \hbar g\left(\hat{\sigma}_+ - \hat{\sigma}_-\right)\left(\hat{a} - \hat{a}^\dagger\right), \tag{2.7}$$

where $g = \mathbf{d}_{eg}\cdot\mathbf{E}_0 = \mathbf{d}_{ge}\cdot\mathbf{E}_0$ denotes the interaction strength, which is commonly referred to as the coupling strength. To further reduce the total Hamiltonian of the system, $\hat{H} = \hat{H}_a + \hat{H}_M + \hat{H}_I$, one final approximation can be made. In the interaction picture two rapidly oscillating terms, associated with $\hat{\sigma}_+\hat{a}^\dagger$ and $\hat{\sigma}_-\hat{a}$, can be removed by the rotating wave approximation. This results in the famous Jaynes-Cummings Hamiltonian [90],

$$\hat{H}_{JC} = \hbar\omega_c\hat{a}^\dagger\hat{a} + \frac{\hbar}{2}\omega_a\hat{\sigma}_z + \hbar g(\hat{\sigma}_+\hat{a} + \hat{\sigma}_-\hat{a}^\dagger). \tag{2.8}$$

The dynamics which result from evolution under this Hamiltonian have been thoroughly studied and can be solved analytically both with and without the consideration of losses [88, 91]. Without the consideration of dissipative effects the system can be evolved by solving the Schrödinger equation in the interaction picture,

$$\hat{H}_{JC}^I = -\hbar\left(\omega_a - \omega_c\right)\hat{\sigma}_{gg} + \hbar g(\hat{\sigma}_+\hat{a} + \hat{\sigma}_-\hat{a}^\dagger), \tag{2.9}$$

with the arbitrary state,

$$|\psi_{JC}\rangle = \alpha(t)|e,n\rangle + C(t)|g,n+1\rangle, \tag{2.10}$$

where $\alpha(t)/C(t)$ are the probability amplitudes that the spin is excited and the cavity mode contains n photons or the spin is in its ground state with $n+1$ photons in the mode such

that $|\alpha(t)|^2 + |C(t)|^2 = 1$. Solving the Schrödinger equation with Eqs.(2.9, 2.10) yields a set of coupled first order differential equations,

$$\dot{\alpha}(t) = -ig\sqrt{n+1}C(t), \tag{2.11}$$

$$\dot{C}(t) = i\left(\omega_a - \omega_c\right)C(t) - ig\sqrt{n+1}\alpha(t), \tag{2.12}$$

which can be easily solved analytically, see Appendix A.2 for a general derivation of these equations. In particular, if the spin is on resonance with the mode of light, that is, for zero detuning, $\Delta_D = \omega_c - \omega_a = 0$, the solutions to Eqs.(2.11, 2.12) are,

$$\alpha(t) = \cos\left(\sqrt{n+1}gt\right), \tag{2.13}$$

$$C(t) = -i\sin\left(\sqrt{n+1}gt\right). \tag{2.14}$$

These solutions show that the oscillation frequency of the excitation transfer between the spin and the cavity mode is directly proportional to both the coupling rate, g, and the number of photons in the mode, n. This frequency is related to the renowned Rabi-frequency, where $\Omega_R^{JC} = 2g\sqrt{n+1}$, as the probabilities oscillate as $|\alpha(t)|^2$ and $|C(t)|^2$ respectively. The dynamics of this system are shown in Fig.2.4 where only a single photon is considered.

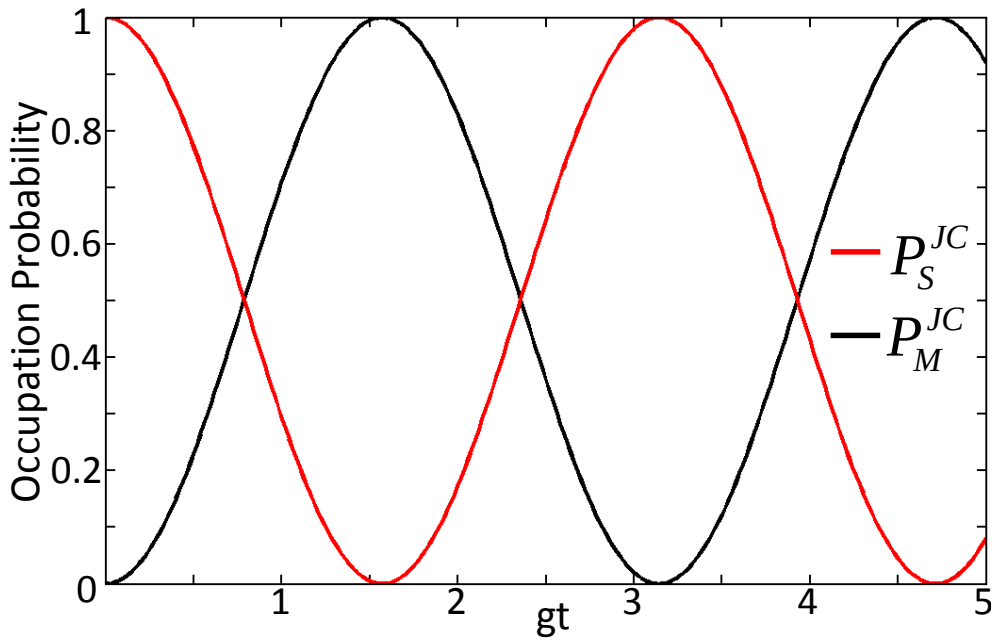

FIGURE 2.4: Rabi-oscillations between a single spin and a single photon ($n = 0$) in the Jaynes-Cummings model. The evolution shown was performed using $\Delta_D = 0$ in units of g and the initial state $|\psi(0)\rangle = |0\rangle|e\rangle$. Here $P_S = \mathrm{Tr}\left[\hat{\rho}\hat{\sigma}_{ee}\right]$ denotes the probability that the spin is excited and $P_M = \mathrm{Tr}\left[\hat{\rho}\hat{a}^\dagger\hat{a}\right]$ the probability the mode is excited.

2.2.2 The Tavis-Cummings Model

With some foundations established for light-matter interactions more complicated systems can now be studied. The first extension of the JC model which will be considered involves the introduction of an ensemble of spins into the system. The many spin extension of the JC model is more commonly known as the Tavis-Cummings (TC) model [56]. Extensive work has focused both theoretically and experimentally on exploring how such a system evolves [16, 18, 92]. The Hamiltonian for this system is generally established by simply extending Eq.(2.8) to describe an ensemble of spins,

$$\hat{H}_{TC}^{G} = \hbar\omega_c \hat{a}^\dagger \hat{a} + \frac{\hbar}{2}\sum_{i=1}^{N} \omega_i \hat{\sigma}_z^i + \hbar \sum_{i=1}^{N} g_i (\hat{\sigma}_+^i \hat{a} + \hat{\sigma}_-^i \hat{a}^\dagger), \tag{2.15}$$

where each spin has a unique resonance frequency, ω_i, and coupling rate with the light field, g_i. Due to the generality of the Hamiltonian, evolution of this system is not an easy task. Numerical simulations of the evolution are extremely difficult for realistic values of N and a large number of excitations in the system due to the enormous size of the Hilbert space. This means that several assumptions must be made in order to have any hope in performing an efficient evolution. The most effective assumption which is often made is to assume that the spins are all identical. This corresponds to $g_i = g$ and $\omega_i = \omega_a$ for all N spins, reducing Eq.(2.15) to,

$$\hat{H}_{TC} = \hbar\omega_c \hat{a}^\dagger \hat{a} + \frac{\hbar}{2}\omega_a \sum_{i=1}^{N} \hat{\sigma}_z^i + \hbar g \sum_{i=1}^{N} (\hat{\sigma}_+^i \hat{a} + \hat{\sigma}_-^i \hat{a}^\dagger). \tag{2.16}$$

Without the consideration of dissipative effects, evolution under $\hat{H}_{TC}$ with a large number of spins is still only possible numerically for special cases. In particular in the weak excitation regime, $\langle \hat{a}^\dagger \hat{a} \rangle + \sum_i^N \langle \hat{\sigma}_{ee}^i \rangle \approx 1$, evolution under $\hat{H}_{TC}$ can even be performed analytically, for zero detuning. The weak excitation regime also allows for the study of quantum interferences which arise through the interactions between the ensemble of spins and the single cavity mode. These interferences have been shown to provide a effective enhancement to the coupling rate, g [16, 18, 56]. The enhancement is the result of constructive quantum interference which arises from the indistinguishability of the spins with respect to the mode of light. For example, in the case of a single photon interacting with N identical spins, if the excitation initially resides in the cavity mode, naturally, it is absorbed by the spins. However, as the spins are indistinguishable, the photon is not absorbed by a single spin, but by all of them simultaneously. That is, once a photon has been absorbed from the cavity, the spins are in a quantum superposition of each being excited while the others are not, resulting

in a factor of $\sqrt{N}$ enhancement to the coupling rate. An alternative, and more comparative, approach to observing this enhancement involves the introduction of the collective operators,

$$\hat{\Sigma}_+ = \frac{1}{\sqrt{N}} \sum_{i=1}^{N} \hat{\sigma}_+^i \quad , \quad \hat{\Sigma}_- = \frac{1}{\sqrt{N}} \sum_{i=1}^{N} \hat{\sigma}_-^i . \tag{2.17}$$

By expressing the interaction picture Hamiltonian,

$$\hat{H}_{TC}^I = -\hbar \sum_{i=1}^{M} (\omega_a - \omega_c)\, \hat{\sigma}_{gg}^i + \hbar g \sum_{i=1}^{N} \left(\hat{\sigma}_+^i \hat{a} + \hat{\sigma}_-^i \hat{a}^\dagger \right), \tag{2.18}$$

in terms of these collective operators the factor of $\sqrt{N}$ enhancement can be observed. In the case of zero detuning, expression of Eq.(2.18) in terms of the collective operators gives,

$$\hat{H}_{TC}^I = \hbar g \sqrt{N} (\hat{\Sigma}_+ \hat{a} + \hat{\Sigma}_- \hat{a}^\dagger), \tag{2.19}$$

which is almost identical to the interaction picture JC Hamiltonian, Eq.(2.9), but with a factor of $\sqrt{N}$ enhancement to the coupling rate. Evolution under $\hat{H}_{TC}^I$ can now be performed in an almost identical manner to the JC model but with the replacement of g with $\sqrt{N}g$ and the consideration of normalisation. Also, as we are working within the weak excitation regime $n \approx 0$. The solutions obtained in this case are then,

$$\alpha_j(t) = \frac{1}{\sqrt{N}} \cos\left(\sqrt{N} g t\right), \tag{2.20}$$

$$C(t) = -i \sin\left(\sqrt{N} g t\right), \tag{2.21}$$

where $\alpha_j(t)$ is the probability amplitude that the jth spin is excited. These solutions make it clear that as a result of the introduction of many identical spins the Rabi-frequency is increased by a factor of $\sqrt{N}$, $\Omega_R^{TC} = 2\sqrt{N}g$. The evolution of this system is shown in Fig.2.5 where the enhancement in the Rabi-frequency, in comparison with the JC model (Fig.2.4), can be clearly observed.

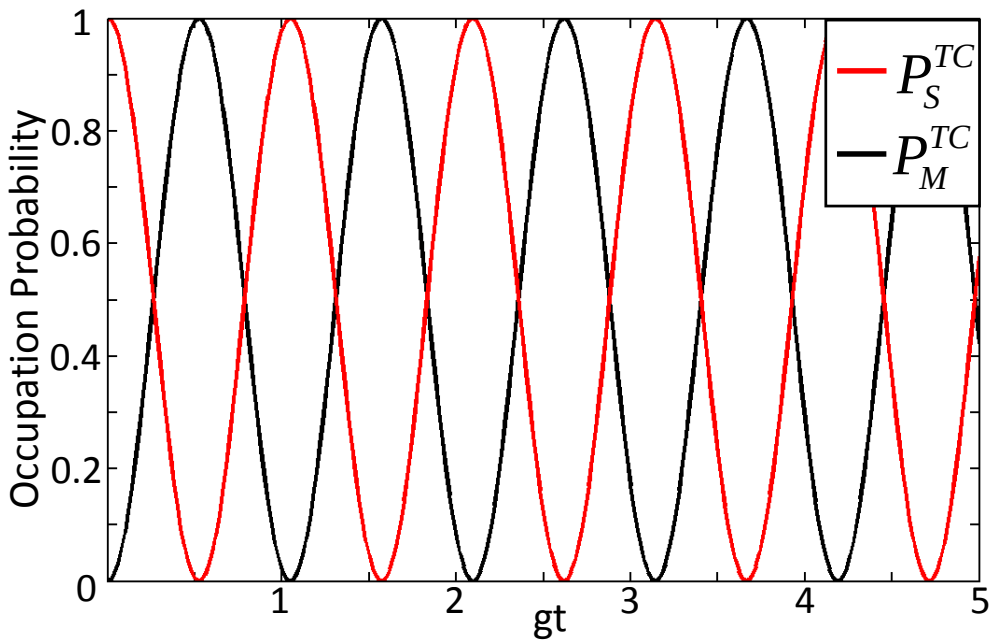

Figure 2.5: Rabi-oscillations between an ensemble of identical spins and a single photon in the Tavis-Cummings model. The evolution shown was performed for a system containing $N = 9$ spins with $\Delta_D = 0$ in units of g. Here $P_S = \mathrm{Tr}\left[\hat{\rho}\sum_{i=1}^{9}\hat{\sigma}_{ee}^{i}\right]$ denotes the probability that the spins are collectively excited and $P_M = \mathrm{Tr}\left[\hat{\rho}\hat{a}^{\dagger}\hat{a}\right]$ the probability the mode is excited. The system was initialised in the state $|\psi(0)\rangle = \frac{1}{3}\sum_{i=1}^{9}|0\rangle|e_i\rangle$ where $|0\rangle|e_i\rangle$ corresponds to the ith spin excited while the rest are in the ground state.

2.2.3 The Multi-Mode Jaynes-Cummings Model

While it has been shown an effective enhancement to the coupling strength can be achieved through the introduction of many identical spins, creating such a system experimentally is typically difficult as the spins must be confined within a cavity and interact identically with the cavity mode. This difficulty gives rise to the questions: Is there another, more practical method in which quantum interference could provide an enhancement to the coupling rate? As in the TC model the constructive quantum interference results from the indistinguishability of the spins with respect to the cavity mode, could such an interference be achieved if the roles were reversed? That is, would constructive quantum interference arise if an ensemble of indistinguishable modes interacted with a single spin? To determine if such an enhancement is in fact possible, the JC model will now be extended to consider an ensemble of degenerate modes. This extension of the JC model has very rarely been studied [84, 85, 87], typically due to the experimental difficulties in creating a system which can sustain many degenerate modes. As discussed earlier, Fabry-Pérot type cavities are traditionally used in cQED experiments and can not be advantageously scaled to consider multiple degenerate modes.

The main limitation stems from the inverse proportionality between the coupling rate and the mode volume, described in Eq.(2.7). For more than two Fabry-Pérot cavities the mode volume increases enormously in comparison to the small increase in the enhancement which means that overall the coupling strength decreases. An alternative type of cavity which can efficiently sustain many cavity modes will be discussed in Section 2.3. Beforehand, however, the dynamics of the multi-mode system must be studied to determine if the introduction of many modes can produce constructive quantum interference. The multi-mode extension of the JC Hamiltonian can be attained by extending Eq.(2.8) to consider N degenerate modes,

$$\hat{H}_{MM} = \hbar\omega_c \sum_{i=1}^{N} \hat{a}_i^\dagger \hat{a}_i + \frac{\hbar}{2}\omega_a \hat{\sigma}_z + \hbar \sum_{i=1}^{N} g_i(\hat{\sigma}_+ \hat{a}_i + \hat{\sigma}_- \hat{a}_i^\dagger). \tag{2.22}$$

By following an identical approach as in the previous section, where $g_i = g$ and assuming that there is only a weak excitation in the system, a factor of $\sqrt{N}$ enhancement can be observed. In the interaction picture Eq.(2.22) reduces to,

$$\hat{H}_{MM}^I = -\hbar\left(\omega_a - \omega_c\right)\hat{\sigma}_{gg} + \hbar g \sum_{i=1}^{N} \left(\hat{\sigma}_+ \hat{a}_i + \hat{\sigma}_- \hat{a}_i^\dagger\right). \tag{2.23}$$

Now, by the introduction of multi-mode collective operators,

$$\hat{A} = \frac{1}{\sqrt{N}} \sum_{i=1}^{N} \hat{a}_i \quad , \quad \hat{A}^\dagger = \frac{1}{\sqrt{N}} \sum_{i=1}^{N} \hat{a}_i^\dagger, \tag{2.24}$$

Eq.(2.23) can be rewritten, in the case of zero detuning, to give,

$$\hat{H}_{MM}^I = \hbar g \sqrt{N}(\hat{\sigma}_+ \hat{A} + \hat{\sigma}_- \hat{A}^\dagger), \tag{2.25}$$

showing that an identical $\sqrt{N}$ enhancement can be achieved in the multi-mode case. Again, in terms of the collective operators the above Hamiltonian resembles that of the JC model, Eq.(2.9), but with a factor of $\sqrt{N}$ increase to the coupling strength. This means that, if dissipative effects are ignored, the system can be evolved in an analogous manner to the TC model giving,

$$\alpha(t) = \cos\left(\sqrt{N} g t\right), \tag{2.26}$$

$$C_j(t) = -\frac{i}{\sqrt{N}} \sin\left(\sqrt{N} g t\right), \tag{2.27}$$

where here $C_j(t)$ denotes the probability amplitude that the jth mode is excited. These solutions show that as a result of the introduction of many identical modes the Rabi-frequency is increased by a factor of $\sqrt{N}$, $\Omega_R^{MM} = 2\sqrt{N}g$.

2.2.4 The Multi-Mode Tavis-Cummings Model with Loss

It has now been shown that enhancements to the coupling strength can be achieved by introducing either an ensemble of atoms, or an ensemble of modes into the system. The question which now remains is: is that the best we can do? In hope to achieve a larger enhancement the last extension to the JC model that will be considered is the multi-spin/multi-mode case. In this case only weak excitation will be considered and it will still be assumed that the coupling rate is uniform, however, unlike the previous sections, generality of the spin and mode resonant frequencies will be kept. The Hamiltonian of this system can be attained by either extension of Eq.(2.22) or Eq.(2.15),

$$\hat{H}_{MMTC} = \hbar \sum_{i=1}^{N} \omega_i \hat{a}_i^\dagger \hat{a}_i + \frac{1}{2}\hbar \sum_{i=1}^{M} \Omega_i \hat{\sigma}_z^i + \hbar g \sum_{j=1}^{M} \sum_{i=1}^{N} \left(\hat{\sigma}_+^j \hat{a}_i + \hat{\sigma}_-^j \hat{a}_i^\dagger \right), \tag{2.28}$$

where the resonant frequencies of the spins are now labelled Ω_i. Through the use of the collective operators, Eqs.(2.17, 2.24), it can be shown in an analogous manner that a factor of $\sqrt{MN}$ enhancement can be achieved in this case. As this is the most general of the three systems considered above the effects of dissipation on the system will be included here. The standard approach to incorporate decoherence into the evolution of a quantum system is to solve the master equation. Here it would require solving,

$$\dot{\hat{\rho}} = -\frac{i}{\hbar}\left[\hat{H}_{MMTC}, \hat{\rho}\right] + \sum_{k=1}^{M} \gamma_k \left[\hat{\sigma}_-^k \hat{\rho} \hat{\sigma}_+^k - \tfrac{1}{2}\left[\hat{\sigma}_+^k \hat{\sigma}_-^k, \hat{\rho}\right\}\right] + \sum_{j=1}^{N} \kappa_j \left[\hat{a}_j \hat{\rho} \hat{a}_j^\dagger + \tfrac{1}{2}\left\{\hat{a}_j^\dagger \hat{a}_j, \hat{\rho}\right\}\right], \tag{2.29}$$

which is not possible for the number of spins/modes that will be considered in later sections due to the enormous size of the Hilbert space. This means an alternative method of evolution must be used. An approximate approach which is often used to evolve large systems involves solving the Schrödinger equation with damping accounted for by a non-Hermitian Hamiltonian [93],

$$\hat{H}_C = \hbar \sum_{j=1}^{N} \left(\omega_j - \frac{i}{2}\kappa_j\right) \hat{a}_j^\dagger \hat{a}_j + \frac{\hbar}{2} \sum_{j=1}^{M} \left(\Omega_j \hat{\sigma}_z^j - i\gamma_j \hat{\sigma}_{ee}^j\right) + \hbar g \sum_{j=1}^{M} \sum_{k=1}^{N} \left(\hat{\sigma}_+^j \hat{a}_k + \hat{\sigma}_-^j \hat{a}_k^\dagger\right). \tag{2.30}$$

As this engineered Hamiltonian is not Hermitian, probability is not conserved under evolution. However, by restricting this system to the single excitation basis, $\sum_i^N \langle \hat{a}_i^\dagger \hat{a}_i \rangle + \sum_i^M \langle \hat{\sigma}_{ee}^i \rangle = 1$, and by assuming the loss of probability due to the non-unitary evolution corresponds to the population of the ground state $|0\rangle|g\rangle$, it can be proved that the dynamics given by the "conditional" Hamiltonian, Eq. (2.30), exactly matches the dynamics obtained by solving the full master equation, see Appendix A.1. The single excitation subspace for the M spin N mode system is spanned by the states,

$$|0\rangle|e_k\rangle \equiv |0_1, ..., 0_N\rangle|g_1, g_2, ..., g_{k-1}, e_k, g_{k+1}, ..., g_M\rangle, \tag{2.31}$$

$$|1_k\rangle|g\rangle \equiv |0_1, 0_2, ..., 0_{k-1}, 1_k, 0_{k+1}, ..., 0_N\rangle|g_1, ..., g_M\rangle, \tag{2.32}$$

$$|0\rangle|g\rangle \equiv |0_1, ..., 0_N\rangle|g_1, ..., g_M\rangle. \tag{2.33}$$

This system can now be evolved by solving the Schrödinger equation in the interaction picture,

$$\hat{H}_C^I = -\hbar \sum_{j=1}^{M} \left(\Omega_j - i\frac{\gamma_j}{2} - \bar{\omega}\right) \hat{\sigma}_{gg}^j - i\frac{\hbar}{2} \sum_{j=1}^{N} \kappa_j \hat{a}_j^\dagger \hat{a}_j + \hbar g \sum_{j=1}^{M} \sum_{k=1}^{N} \left(\hat{\sigma}_+^j \hat{a}_k + \hat{\sigma}_-^j \hat{a}_k^\dagger\right), \tag{2.34}$$

with the state,

$$|\psi(t)\rangle = \sum_{k=1}^{N} \alpha_k(t)|0\rangle|e_k\rangle + \sum_{k=1}^{N} C_k(t)|1_k\rangle|g\rangle, \tag{2.35}$$

where $\bar{\omega}$ is the average of all the mode frequencies. Substitution of Eqs.(2.34, 2.35) into the Schrödinger equation yields the following set of coupled first order equations,

$$i\dot{\alpha}_k(t) = -\sum_{j=1}^{M} \left(\Omega_j - i\frac{\gamma_j}{2} - \bar{\omega}\right) \alpha_k(t) + \left(\Omega_k - i\frac{\gamma_k}{2} - \bar{\omega}\right) \alpha_k(t) + g \sum_{j=1}^{N} C_j(t), \tag{2.36}$$

$$i\dot{C}_k(t) = -\sum_{j=1}^{M} \left(\Omega_j - i\frac{\gamma_j}{2} - \bar{\omega}\right) C_k(t) - i\frac{\kappa_k}{2} C_k(t) + g \sum_{j=1}^{M} \alpha_j(t), \tag{2.37}$$

which can be solved numerically. In the special case where there is no dissipation and the detuning is set to zero, for $M = N = 3$, the evolution essentially identical to that depicted in Fig.2.5, where in this case $P_M = \mathrm{Tr}\left[\hat{\rho} \sum_{i=1}^{3} \hat{a}_i^\dagger \hat{a}_i\right]$ and $P_S = \mathrm{Tr}\left[\hat{\rho} \sum_{i=1}^{3} \hat{\sigma}_{ee}^i\right]$. The benefit to leaving generality to the most complicated extension of the JC model is that the above equations can be easily reduced to consider either the TC or MM models more generally. Simulations of dissipative effects will be left for later sections where realistic values for κ, γ and g will be used.

2.2.5 Conclusion

In this section the Jaynes-Cummings model was studied along with three possible extensions. These extensions involved the introduction of many spins, or modes, into the system as well as the introduction of many spins and many modes. In each case the dynamics of the light-matter interactions were solved in the weak excitation regime while assuming that the coupling strength was uniform. It was found that each system exhibited essentially identical dynamics as the main effect of increasing the system size was to increase the effective coupling strength. In the many spin/mode extension of the JC model it was found the increase in the effective coupling strength was proportional to the square root of the number of spins/modes considered in the system. It was also found that a further enhancement could be achieved by considering a system which contained many spins as well as many modes. In this case the enhancement was proportional to the square root of the number of modes multiplied by the number of spins. To demonstrate the effective enhancements in each of the considered extensions the dynamics are presented in Fig.2.6 where the enhancement factor is identical for each extension. The results clearly show that identical Rabi-Oscillations are achieved in each of the enhanced cases, which oscillate at higher frequencies compared to the JC model.

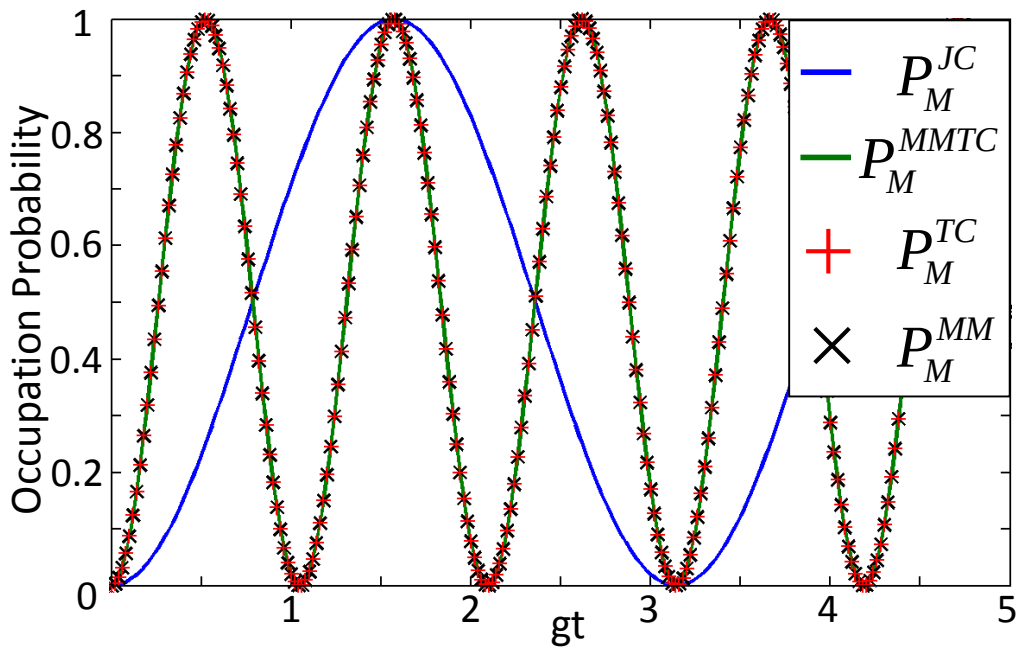

Figure 2.6: The Rabi-oscillations of the mode in the JC, TC, MM and MMTC models. These simulations were performed with $\Delta_D = 0$ in units of g under ideal conditions. The simulations of the TC/MM models were performed using 9 identical spins/modes and the initial states $|\psi(0)\rangle_{TC} = \frac{1}{3}\sum_{i=1}^{9}|0, e_i\rangle$ and $|\psi(0)\rangle_{MM} = |0, e\rangle$ respectively. In the MMTC simulation 3 identical spins and 3 identical modes were used with the initial state $|\psi(0)\rangle_{MMTC} = \frac{1}{\sqrt{3}}\sum_{i=1}^{3}|0\rangle|e_i\rangle$.

2.3 Whispering Gallery Modes in Microspheres

The basic theory describing the dynamics of a system consisting of an ensemble of cavity modes and an ensemble of spins has now been established. As mentioned previously, realisation of such a system is not trivial and is in fact not possible using traditional Fabry-Pérot type cavities. To date only one multi-mode system has been realised which was only capable of sustaining a maximum of five semi-degenerate modes [87]. In this section it will be shown that spherical resonators are capable of supporting a large number of degenerate modes. These modes are the result of total internal reflections within the spherical resonator which confine light producing an ensemble of optical modes. The resulting modes are called whispering gallery modes. A particular subset of these modes will be focused on which are confined close to the surface of the resonator, referred to as the fundamental mode. The ensemble of modes that will be considered correspond to rotated duplicates of the fundamental mode, as shown in Fig.2.3. The interaction between individual spins and the ensemble of the rotated WGMs will be investigated to determine if constructive quantum interference can be achieved. To do so, expressions for the electric fields within the resonator will first be established for each of the rotated WGMs to provide understanding of the field's intensity distribution, polarisation and frequency.

2.3.1 Fields in Spherical Whispering Gallery Resonators

2.3.1.1 Deriving the Electric Field

The electric fields of a dielectric sphere will first be derived. To begin, a sphere of radius a and refractive index n_1 which is suspended in a medium of refractive index n_2 will be considered. It will first be assumed that the fields within the dielectric sphere are harmonic, that is,

$$\mathbf{E} = \mathbf{E}_0 e^{i(kx-\omega t)} \quad , \quad \mathbf{H} = \mathbf{H}_0 e^{i(kx-\omega t)}, \tag{2.38}$$

where $\mathbf{E}$ is the electric field and $\mathbf{H}$ the magnetic vector potential which are related to the electric displacement vector and magnetic field, respectively, by,

$$\mathbf{H} = \frac{1}{\mu}\mathbf{B}, \tag{2.39}$$

$$\mathbf{D} = \varepsilon\mathbf{E}. \tag{2.40}$$

Now, through the use of Maxwell's equations,

$$\nabla \times \mathbf{E} = -\frac{\partial \mathbf{B}}{\partial t}, \tag{2.41}$$

$$\nabla \times \mathbf{B} = \frac{\partial \mathbf{D}}{\partial t}, \tag{2.42}$$

it can be shown that the electric field is governed by the vectorial Helmholtz equation. This can be shown by first performing a direct substitution of Eqs.(2.38, 2.39) into Eq.(2.41) to give,

$$\nabla \times \mathbf{E} = i\omega\mu\mathbf{H}. \tag{2.43}$$

Now, taking the curl of this equation on both the left and right hand sides gives,

$$\nabla \times \nabla \times \mathbf{E} = i\omega\mu\nabla \times \mathbf{H} = i\omega\mu\left(-i\omega\varepsilon\mathbf{E}\right), \tag{2.44}$$

after the substitution of Eqs.(2.42, 2.40 and 2.38). The left hand side of Eq.(2.44) can then be simplified through the use of a standard vector identity,

$$\nabla \times \nabla \times \mathbf{E} = \nabla\left(\nabla \cdot \mathbf{E}\right) - \nabla^2\mathbf{E} = -\nabla^2\mathbf{E}. \tag{2.45}$$

Finally, after substitution of Eq.(2.45) into Eq.(2.44), the vectorial Helmholtz equation is achieved,

$$\nabla^2\mathbf{E} + \omega^2\mu\varepsilon\mathbf{E} = 0. \tag{2.46}$$

This equation can be more practically expressed in terms of the wave vector, k, and the refractive index $n(r)$,

$$\nabla^2\mathbf{E} + k^2n^2(r)\mathbf{E} = 0, \tag{2.47}$$

where the refractive index is given by,

$$n(r) = \begin{cases} n_1 & \text{if } r < a, \\ n_2 & \text{if } r \geq a. \end{cases} \tag{2.48}$$

A general expression for the electric field within the spherical resonator can now be obtained by solving Eq.(2.47). The vectorial Helmholtz equation has been thoroughly studied previously where it has been found that analytic solutions exist in the form of vector spherical harmonics (VSH) [94]. The standard approach to arriving at these solutions is through the use of Debye potentials. To start this derivation, one must first notice that if ψ is a solution to the scalar Helmholtz equation, then $\hat{r}\psi$ is a solution to the vectorial Helmholtz equation,

Eq.(2.47). This implies that both, $\mathbf{M} = \nabla \times \hat{r}\psi$ and $\mathbf{N} = \frac{1}{k}\nabla \times \mathbf{M}$ are a pair of orthogonal solutions of Eq.(2.47) and hence that the general solution to this equation can be expressed as the linear combination,

$$\mathbf{E} = c_1\mathbf{M} + c_2\mathbf{N}, \tag{2.49}$$

where c_1 and c_2 are arbitrary constants. To arrive at an analytic expression for the electric field through the use of Eq.(2.49) the solutions to the scalar Helmholtz equation, ψ, must be determined. As a spherical resonator is of interest here, the Helmholtz equation in spherical coordinates,

$$\frac{2}{r}\frac{\partial\psi}{\partial r} + \frac{\partial^2\psi}{\partial r^2} + \frac{1}{r^2\sin\theta}\cos\theta\frac{\partial\psi}{\partial\theta} + \frac{1}{r^2}\frac{\partial^2\psi}{\partial\theta^2} + \frac{1}{r^2\sin^2\theta}\frac{\partial^2\psi}{\partial\phi^2} + k^2n^2(r)\psi = 0, \tag{2.50}$$

must be solved. This equation can be systematically solved using the separation of variables technique. That is, by assuming the solution can be written in the form $\psi = R(r)\Theta(\theta)\Phi(\phi)$. After substitution of ψ into Eq.(2.50) three separate differential equations arise by noting that each of the functions R, Θ and Φ are constant with respect to one another.

$$\frac{\partial}{\partial r}\left(r^2R'\right) + \left(r^2k^2n^2(r) - l(l+1)\right)R = 0 \tag{2.51}$$

$$\frac{1}{\sin\theta}\frac{\partial}{\partial\theta}\left(\Theta'\sin\theta\right) + \left(l(l+1) - \frac{m^2}{\sin^2\theta}\right)\Theta = 0 \tag{2.52}$$

$$\Phi'' + m^2\Phi = 0 \tag{2.53}$$

Each of these equations can now be individually solved to sequentially arrive at an analytic expression for ψ. The first of these differential equations, Eq.(2.51), resembles the spherical Bessel equation. Thus the solutions to the radial portion of ψ can be expressed in terms of the spherical Bessel functions j_l and y_l,

$$R_l(r) = c_3j_l(z) + c_4y_l(z), \tag{2.54}$$

where the arbitrary constants c_3 and c_4 depend on boundary conditions, $z(r) = n(r)kr$ and the spherical Bessel functions j_l/y_l are given by,

$$j_l(z) = \sqrt{\frac{\pi}{2z}}J_{l+\frac{1}{2}}(z), \tag{2.55}$$

$$y_l(z) = (-1)^{l+1}\sqrt{\frac{\pi}{2z}}J_{-l+\frac{1}{2}}(z), \tag{2.56}$$

in which J_k represents the Bessel function of the first kind. As the spherical Bessel function

$y_l(z)$ diverges at $r = 0$ this solution is typically split into two cases to maintain physical sense,

$$R_l(r) = \begin{cases} j_l(z) & \text{if } r < a, \\ B\chi_l(z) & \text{if } r \geq a, \end{cases} \tag{2.57}$$

where $B = c_4/c_3$ and $\chi_l(z)$ represents either j_l, y_l or the linear combinations $h_l^{(1)} = j_l + iy_l$, $h_l^{(2)} = j_l - iy_l$, otherwise known as Hankel functions.

The polar portion of ψ can now be attained by solving the second of the three equations, Eq.(2.52). This equation has the form of the associated Legendre equation and hence has the general solution,

$$\Theta(\theta) = c_5 P_l^m(\cos\theta) + c_6 Q_l^m(\cos\theta), \tag{2.58}$$

where P_l^m/Q_l^m are the associated Legendre polynomials of the first and second kind respectively and c_5/c_6 are arbitrary constants. The indices l and m are integers that satisfy $-l \leq m \leq l$. As in spherical coordinates, $0 \leq \theta \leq \pi$, the constant c_6 must be set to zero since Q_l^m is unbounded at $\cos(\theta) = \pm 1$. This reduces the solution to the polar portion of ψ to,

$$\Theta(\theta) = c_5 P_l^m(\cos\theta). \tag{2.59}$$

Finally, the azimuthal component of ψ can be derived by solving Eq.(2.53). This is an elementary second order differential equation which can be solved to attain the solution,

$$\Phi(\phi) = c_7 e^{im\phi}, \tag{2.60}$$

for $m = \pm 1, \pm 2, ..., \pm l$ [94].

With each of the components of ψ now established, the solution to the scalar Helmholtz equation can be written,

$$\psi_{lm}(r,\theta,\phi) = Ae^{im\phi} P_l^m(\cos\theta) R(r) = Y_l^m(\theta,\phi) R(r), \tag{2.61}$$

allowing for general expressions of the electric field within the spherical resonator to be achieved. Here Y_l^m denote spherical harmonics where $A = c_5 c_7$ is a normalisation constant. There are two polarisations of the field which must be taken into consideration; Transverse electric (TE) and transverse magnetic (TM). In the case of a TE polarised field there should be no radial electric field component. This means that for TE fields the constant c_2 in Eq.(2.49) must be set to zero, as $\mathbf{N} \cdot \hat{r} \neq 0$, giving,

$$\mathbf{E}^{TE} = \mathbf{M} = \nabla \times \mathbf{r}\psi = \frac{1}{\sin\theta}\frac{\partial\psi}{\partial\phi}\hat{\theta} - \frac{\partial\psi}{\partial\theta}\hat{\phi}. \tag{2.62}$$

For TM polarised fields a radial electric field component is expected which means as $\mathbf{N} \cdot \hat{r} \neq 0$ and $\mathbf{M} \cdot \hat{r} = 0$ the constant c_1 in Eq.(2.49) must be set to zero to obtain,

$$\begin{aligned} \mathbf{E}^{TM} &= \frac{1}{nk} \nabla \times \mathbf{M} \\ &= -\frac{1}{rnk} l(l+1)\psi\, \hat{r} + \left(\frac{1}{rnk} \frac{\partial \psi}{\partial \theta} + \frac{1}{nk} \frac{\partial \psi}{\partial r \partial \theta} \right) \hat{\theta} + \left(\frac{1}{rnk} \frac{1}{\sin\theta} \frac{\partial \psi}{\partial \phi} + \frac{1}{nk} \frac{1}{\sin\theta} \frac{\partial \psi}{\partial r \partial \phi} \right) \hat{\phi}. \end{aligned} \tag{2.63}$$

These solutions are most commonly expressed more compactly in terms of VSH, see Appendix B.1, however, written in the above manner each of the field components can be clearly observed. This allows for the polarisation of the field to be studied in a more efficient manner.

2.3.1.2 Mode Numbers and Boundary Conditions

With general expressions for the electric fields within a spherical resonator established the ensemble of different WGMs can be studied. These modes are typically characterised by three mode numbers, q, l and m the radial, polar and azimuthal mode numbers. The mode numbers can be interpreted as related to the number of intensity maxima in the; radial, polar and azimuthal directions, respectively. As seen in Eq.(2.61) the mode numbers m and l result from solving Eqs.(2.52, 2.53). The radial mode number, q, results from the application of the boundary conditions on $R(r)$. These conditions differ between the TE and TM modes. In the case of TE modes, $R(r)$ and $n(r)R'(r)$ must be continuous at the sphere's surface ($r = a$), while in the TM case, $R'(r)/n(r)$ must be continuous. These conditions can be used both to achieve an expression for the constant B in Eq.(2.57) and to calculate the resonant wavenumbers of the modes, k_{ql}. It is in the calculation of the resonant wavenumbers that the radial mode number comes into play. Before continuing, however, the boundary conditions will first be applied to determine B in Eq.(2.57). The first of the boundary conditions can be used to give,

$$R_{ql}(r) = \begin{cases} j_l(z) & \text{if } r < a, \\ \frac{j_l(z_1)}{\chi_l(z_2)} \chi_l(z) & \text{if } r \geq a, \end{cases} \tag{2.64}$$

where $z_1 = n_1 k_{ql} a$ and $z_2 = n_2 k_{ql} a$.

Now that B has been calculated, the continuity of $R'(r)$ can be used to achieve the resonance condition,

$$s \frac{j_l'(z_1)}{j_l(z_1)} = \frac{\chi_l'(z_2)}{\chi_l(z_2)}, \tag{2.65}$$

where,

$$s = \begin{cases} n_1/n_2 & \text{for TE modes,} \\ n_2/n_1 & \text{for TM modes,} \end{cases} \tag{2.66}$$

in which the wavenumbers k_{ql} are the solutions. The resonant wavenumbers can be calculated by either solving Eq.(2.65) numerically or through the use of the Schiller expansion, provided that $\lambda \ll a$,

$$z_{ql} \approx \frac{v}{t} + \frac{\zeta_q}{t}\left(\frac{v}{2}\right)^{1/3} - \frac{p^2}{\sqrt{t^2-1}} + \frac{3}{10}\frac{\zeta_q^2}{2^{2/3}tv^{1/3}} - \frac{2^{2/3}\zeta_q}{3\left(t^2-1\right)^{3/2}v^{2/3}}t^2p^3 + \frac{\zeta_q}{2^{1/3}\left(t^2-1\right)^{3/2}v^{2/3}}t^2p, \tag{2.67}$$

where $v = l + \frac{1}{2}$, ζ_q is the qth root of the Airy function, $t = n_1/n_2$ and $p = 1$ for TE modes or $1/t^2$ for TM [95].

With the boundary conditions applied and the three mode numbers established the final task is to determine which of these modes must be considered for the proposed configuration (Fig.2.3). As the intention is to place each of the spins near the surface of the sphere, we require a set of mode numbers that correspond to modes propagating around the equator of the sphere. That is, with large electric fields near the sphere's surface. This particular set of mode numbers is called the fundamental mode and occurs when $q = 1$ and $l = m = l_{max}$, where l_{max} can be approximated by [96],

$$l_{max} \approx \frac{2\pi a n_1}{\lambda}, \tag{2.68}$$

or, more accurately by solving Eq.(2.67) for v with an approximate resonant wavenumber.

The frequency of the WGMs essentially depends only on the q and l mode numbers. Modes with identical values of q and l but different azimuthal mode numbers, m, are degenerate for perfectly spherical resonators. However, if the eccentricity of the sphere, ϵ_s, is non-zero this degeneracy is broken resulting in a detuning between modes with different azimuthal mode numbers. The detuning can be approximated by,

$$\frac{\Delta\omega}{\omega} = \pm\frac{\epsilon_s^2\left(l^2-m^2\right)}{4l^2}, \tag{2.69}$$

where $\Delta\omega$ is the frequency difference between the fundamental WGM ($q = 1, l = m$) and a mode with the same q and l mode numbers but a different m. The sign depends on whether an oblate sphere (+) or a prolate sphere (-) is considered [96].

2.3.2 Properties of WGMs

As the physics behind the WGM electric fields has now been established several crucial properties of the fields can be focused on. These properties are either crucial to cQED, as they essentially determine whether or not strong spin-light interactions can be achieved, or are essential in achieving the collective enhancement discussed in Section 2.2. In this section the mode volume and polarisation of the WGMs will first be discussed as these parameters essentially define the light-matter interaction rate g. The quality factor of the WGMs will then be examined to achieve an understanding of the optical loss rate κ.

2.3.2.1 Mode Volume

The mode volume is quite possibly the most important parameter in cQED as it is inversely proportional to the square of the coupling strength, Eq.(2.7), and is one of the few controllable degrees of freedom in achieving strong coupling. The standard definition of the mode volume is,

$$V_{mode} = \frac{\left(\int |\mathbf{E}|^2 \, d^3\mathbf{r}\right)^2}{\int |\mathbf{E}|^2 \, |\mathbf{E}|^2 \, d^3\mathbf{r}}. \tag{2.70}$$

This can be either calculated numerically for TE or TM modes, through the use of Eqs.(2.62, 2.63), or approximated by,

$$V_M \approx 3.4\pi^{3/2} \left(\frac{\lambda}{2\pi n_1}\right)^3 l^{11/6} \sqrt{l - m - 1}, \tag{2.71}$$

for spherical resonators, which is only valid for $q = 1$ and $l = l_{max}$ [97]. Most importantly, the approximate form of the mode volume shows that, by recalling Eq.(2.68), it increases almost quadratically with the sphere's radius.

2.3.2.2 Polarisation of WGMs

In cQED applications of WGM resonators the polarisation of the fundamental WGM is either ignored or assumed to be perfectly orthogonal to the direction of propagation [75, 76, 98, 99]. However, this approximation is not entirely valid. It has been recently shown in both bottleneck and cylindrical resonators that the TM modes are not completely transversal [100, 101]. To address this assumption in microspheres the individual electric field components of the TE and TM modes can be calculated through the use of Eqs.(2.62, 2.63). The individual field components for TE and TM modes are presented in Fig.2.7. The results show, in the case of TE modes, that the electric field is predominately $\hat{\theta}$ directed, orthogonal to the direction

of propagation, $\hat{\phi}$. However, this is not the case for the TM modes. For the TM modes the electric field is comprised from an uneven proportion of both $\hat{r}$ and $\hat{\phi}$ components. This not only means that the electric field is not orthogonal to the direction of propagation, $\hat{\phi}$, but that the field itself is partially circularly polarised. This suggests that counter propagating modes will have different polarisations, that is, a clockwise (CW) propagating mode will have $\mathbf{E} \propto \hat{r} + i\hat{\phi}$ while a counter-clockwise (CCW) propagating mode will have $\mathbf{E} \propto \hat{r} - i\hat{\phi}$. Such polarisation means that TM modes will interact with $\Delta m_s = \pm 1$ optical transitions in an atom, depending on the direction of propagation [100]. This directional dependence is not desired in this work as to achieve constructive quantum interference the modes must be indistinguishable with respect to the spin. It is also important to note that these calculations were made in the center of an intensity maxima. Outside of this maxima the direction of both TE and TM electric fields become more complicated, directed along all three spherical-polar directions. These results also show that there is a particular depth within the sphere where the TM mode is perfectly transversal, that will now be referred as the transversal point.

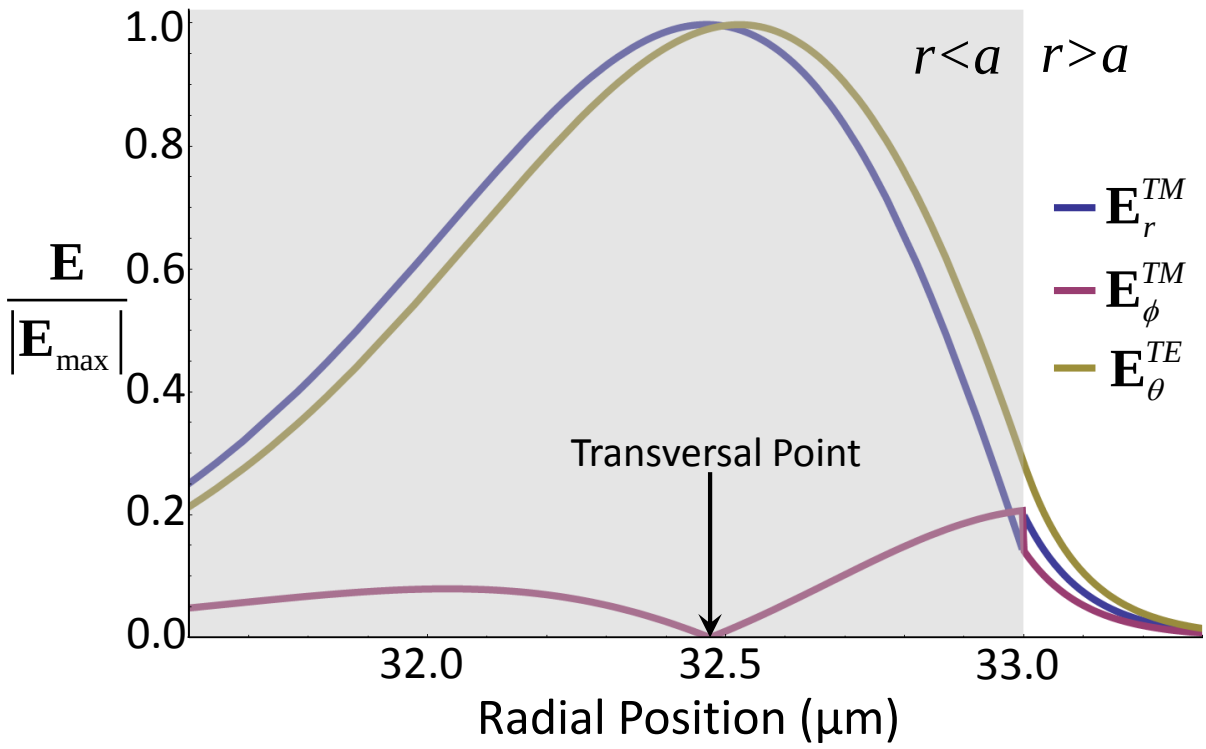

Figure 2.7: The norm of the TM and TE field components for a 33 μm sphere with $n_1 = 1.46$ suspended in air supporting a WGM of wavelength $\lambda = 637$ nm. A special radial position is depicted, 'Transversal Point', where the azimuthal component of the TM mode electric field is zero and the WGM is completely transversal.

2.3.2.3 Quality Factor

The quality factor is another crucial parameter in cQED which must be taken into consideration. It is a measure of how long a cavity can confine light, inversely proportional to the optical loss rate, κ. To calculate the quality factor all loss channels must be considered. In general there are many loss channels for WGMs in spherical resonators including, surface scattering, internal losses due to material absorption and Rayleigh scattering, diffraction losses and those due to surface contaminants [97, 102]. The quality factor of the WGMs can be expressed as the reciprocal sum of the Q factor associated to each of these loss channels,

$$Q_S^{-1} = Q_{SS}^{-1} + Q_{int}^{-1} + Q_{cont}^{-1} + Q_{diff}^{-1}, \tag{2.72}$$

where Q_{SS}, Q_{int}, Q_{cont} and Q_{diff} denote the factor due to surface scattering, internal losses, surface contaminants and diffraction losses respectively. In the case of microspheres the most dominant loss channels are those due to surface scattering and material absorption as typically $Q_{SS}^{-1}, Q_{abs}^{-1} \gg Q_{cont}^{-1}, Q_{RS}^{-1}, Q_{diff}^{-1}$ [97]. This gives an approximate form of the spherical WGM quality factor,

$$Q_S^{-1} \approx Q_{SS}^{-1} + Q_{abs}^{-1} \approx \frac{8\pi^2}{3}\frac{\sigma_s^2\zeta_s^2}{\lambda^4}l^{1/3} + \frac{\lambda}{2\pi n_1}\frac{\alpha_s}{4.3\times 10^3}, \tag{2.73}$$

where σ_s denotes the characteristic surface roughness, ζ_s its correlation length and α_s the attenuation in dB km^{-1} [102]. The quality factor is further reduced if M spherical nano-particles of radius r_{np} and refractive index n_{np} are placed inside the sphere, close to its surface. This loss results from the scattering of light off the nano-particles where the limiting quality factor, Q_{np}, is given by,

$$Q_{np} = \frac{2\pi n_1 V_M}{M\lambda\sigma_{np}}, \tag{2.74}$$

where σ_{np} denotes the classical cross section of the spherical nano-particle,

$$\sigma_{np} = \frac{8\pi}{3}k^4 r_{np}^6 \left(\frac{s'-1}{s'+2}\right)^2, \tag{2.75}$$

with $s' = n_1^2/n_{np}^2$ [103]. The total quality factor of the nano-particle containing spherical resonator is then,

$$Q^{-1} = Q_S^{-1} + Q_{np}^{-1}, \tag{2.76}$$

which approximates to Eq.(2.73) for small spherical scatterers.

2.3.3 Rotation of WGMs

The enhancement to the coupling rate proposed depends entirely on the ability of a spherical resonator to support many degenerate rotated WGMs. To determine if such degenerate rotated modes exist within spherical resonators, expressions for the fields of these rotated modes must first be achieved. In this section expressions for the electric fields of the rotated fundamental WGMs will be established and then used to determine how many of these modes a spherical resonator can support.

The proposed system is comprised of a spherical resonator with spins located at the north and south poles. To achieve an enhanced coupling it is essential that each of the spins interact identically with N modes of light. As mentioned previously, the N modes of light correspond to rotated fundamental WGMs, shown in Figs.2.3 and 2.8. Each of the modes must be rotated such that they each identically intersect both the north and south poles of the sphere. This rotation is required to ensure that the modes interact identically with both spins and hence are indistinguishable. To clearly perform these rotations the spherical harmonics will be expressed in ket notation, that is, Y_{lm} will be expressed as $|l, m\rangle$. As only the fundamental mode will be on resonance with the spin, where $m = l = l_{max}$, the kets become $|l, l\rangle$. The states $|l, l\rangle$ can be arbitrarily rotated using Euler angles via $\hat{R}(\alpha, \beta, \gamma) \equiv \hat{R}_z(\alpha)\hat{R}_x(\beta)\hat{R}_z(\gamma)$, through the use of the Wigner D function [104],

$$|l, l\rangle' = \sum_{m'=-l}^{l} |l, m'\rangle D^l_{m',l}(\alpha, \beta, \gamma), \tag{2.77}$$

where $D^l_{m',m}$ is the Wigner D function. This expression can be extended to VSHs to achieve expressions for the electric fields of the rotated modes [105],

$$\mathbf{E}_{lm}(\theta', \phi') = \sum_{m'=-l}^{l} \mathbf{E}_{l,m'}(\theta, \phi) D^l_{m',l}(\alpha, \beta, \gamma), \tag{2.78}$$

in terms of the new basis vectors. That is, the field can be expressed as a superposition of degenerate fields with different azimuthal mode numbers m. See Appendix B.1 for VSH form of $\mathbf{E}_{lm}$. Now, as the spins are located at the poles of the sphere, the fundamental WGM, which lays on the x-y plane, must be rotated about the x-axis by angle $\frac{\pi}{2}$. This first rotation ensures that the fundamental mode intersects both of the spins. To obtain expressions for the remaining rotated modes, a rotation of η_i about the z-axis can be performed where $0 \leq \eta_i \leq 2\pi$ and $1 \leq i \leq N$, see Fig.2.8. It is important to notice here that each of the rotated modes identically intersect the spins.

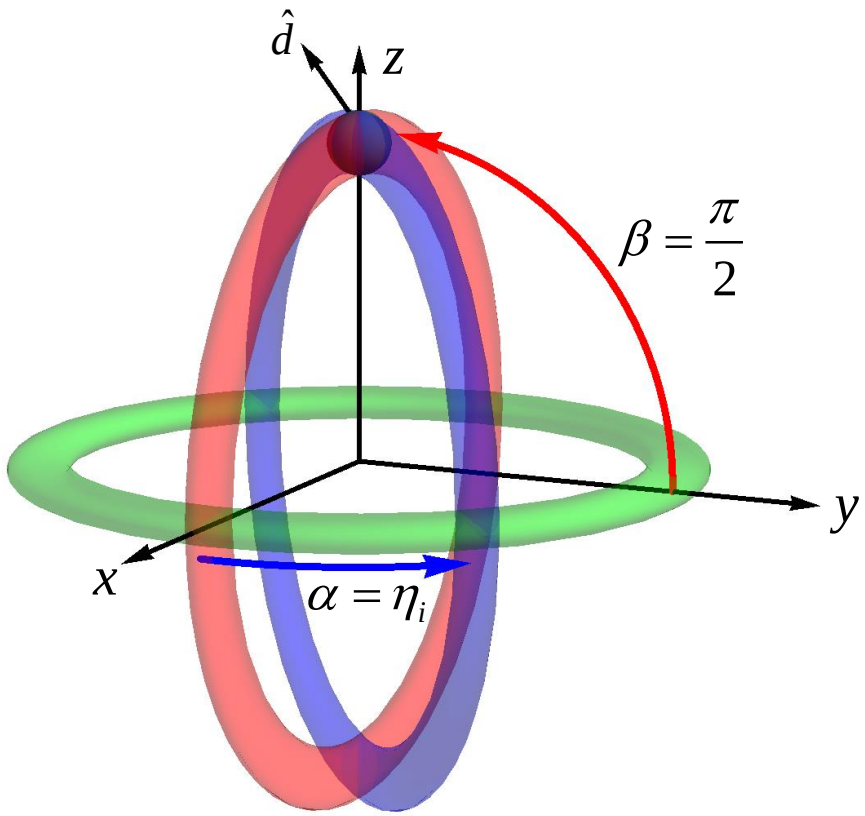

FIGURE 2.8: Depiction of the rotations which are performed to obtain expressions for the rotated WGMs. First the fundamental WGM, which lays in the x-y plane, (green tube) is rotated about the x-axis by $\frac{\pi}{2}$ (red tube). The mode now intersects the spin (black sphere) which is located on the z-axis. Next, a rotation about the z-axis by angle η_i is performed to generate the ith rotated WGM of the ensemble (blue tube).

With expressions for the rotated WGM fields achieved the orthogonality between them can be studied. To do so, in accordance with the rotations discussed above, a state that has been rotated arbitrarily by an angle η_i about the z-axis can be written,

$$|\psi(\eta_i)\rangle = \sum_{m'=-l}^{l} |l, m'\rangle D^l_{m',l}(\eta_i, \tfrac{\pi}{2}, 0). \tag{2.79}$$

The overlap between any two states rotated by either η_i or η_j about the z-axis is then,

$$|\langle\psi(\eta_i)|\psi(\eta_j)\rangle|^2 \approx \frac{1}{2^{4l}} \left|e^{i\eta_i} + e^{i\eta_j}\right|^{4l}, \tag{2.80}$$

which can be approximated by a Gaussian function with standard deviation $\sigma^2_{sd} = l^{-1}_{max}$. This allows for the number of orthogonal rotated modes that can be supported by the spherical

resonator to be approximated by,

$$N \approx \frac{2\pi}{W_{\frac{1}{2}}} = \pi\sqrt{\frac{l_{max}}{2\log 2}}, \tag{2.81}$$

where $W_{\frac{1}{2}}$ is the width at half maximum of the approximated Gaussian. Considering that $l_{max} \propto a$, it is clear that the number of orthogonal modes grows as $\sqrt{a}$ and is also dependent on the wavelength of the mode, see Eq.(2.68). Finally, it is important to note that the electric fields of the rotated TM modes are composed from both $\hat{r}$ and $\hat{\theta}$ components.

2.4 WGM-Spin Coupling

The final task is to now understand the interaction between individual spins and the ensemble of rotated WGMs. There is a large variety of spins which are used in cQED experiments and are applicable to the proposed WGM system. In particular, quantum dots and Silicon/Nitrogen vacancy (NV) centers in nanodiamond (ND) can be considered. In this section the interactions between the zero-phonon line (ZPL) of the NV center in ND and the ensemble of WGMs will be focused on as these solid state systems are relatively popular in cQED due to their many advantageous qualities. The main purpose of this section is to calculate the coupling rate, g, and determine if constructive quantum interference can be achieved by coupling the spin to either the TM or TE WGMs.

When considering the coupling between a mode of light and a single spin the orientation of the spins optical transition dipole moment is often assumed to be aligned with the mode's electric field. To achieve such alignment in most cases is quite challenging experimentally and consequently maximal coupling rates are not achieved. Here the effects of the dipole orientation and field polarisation on the coupling strength will be studied. By recalling Eq.(2.7) the coupling strength is,

$$g = \mathbf{d}\cdot\mathbf{E} = \mu\xi\sqrt{\frac{\omega}{2\hbar\epsilon_0 V_M}}\frac{|\mathbf{E}(\mathbf{r})|}{E_{max}}\hat{d}\cdot\hat{e}, \tag{2.82}$$

where μ is the optical transition dipole moment, $\hat{d}$ and $\hat{e}$ are the unit vectors of the dipole moment and the electric field respectively and ω the frequency of the field. The ratio $|\mathbf{E}(\mathbf{r})|/E_{max}$ and the Debye-Waller factor, ξ, have been introduced to incorporate the effects of the spatial variations in the electric field strength and the proportion of light which couples to the ZPL on the coupling rate. At this point a decision must be made in regards to whether TE or TM modes are ideal in achieving identical interactions between the spin

and each of the rotated modes. As a set of rotated WGMs that interact identically with the antipodal spins is essential in achieving an enhancement to the coupling, the electric fields of the modes at the poles of the sphere must be invariant under rotations about the z-axis. This essentially means a set of modes that have predominately $\hat{r}$ directed electric fields is required. In the case of the TE modes it was seen in Section 2.3.2.2 that the modes were linearly polarised in the $\hat{\theta}$ direction. This means that the rotated TE modes are linearly polarised in the $\hat{\phi}$ direction, so identical interactions between the spins and the rotated TE modes are not possible. The TM modes, in which the electric field was found to be partially circularly polarised in the $\hat{r}$ and $\hat{\phi}$ directions, are now the only remaining option. In the case of the rotated TM modes, the electric field is partially circularly polarised in the $\hat{r}$ and $\hat{\theta}$ directions while the mode also propagates in the $\hat{\theta}$ direction. Consequentially the "handedness" of this circular polarisation still depends on the direction of propagation and hence counter propagating modes are orthogonally polarised. A CW propagating mode will have $\mathbf{E} \propto \hat{r} + i\hat{\theta}$ while a CCW propagating mode will have $\mathbf{E} \propto \hat{r} - i\hat{\theta}$. This means that half of the N rotated modes are partially left hand circularly polarised (σ_L) while the other half are right hand circularly polarised (σ_R), making each mode distinguishable to the atom. This distinguishability can potentially degrade the enhancement to the coupling rate as half of the modes (σ_L) couple to $\Delta m_s = 1$ transitions while the other half (σ_R) couple to $\Delta m_s = -1$ transitions.

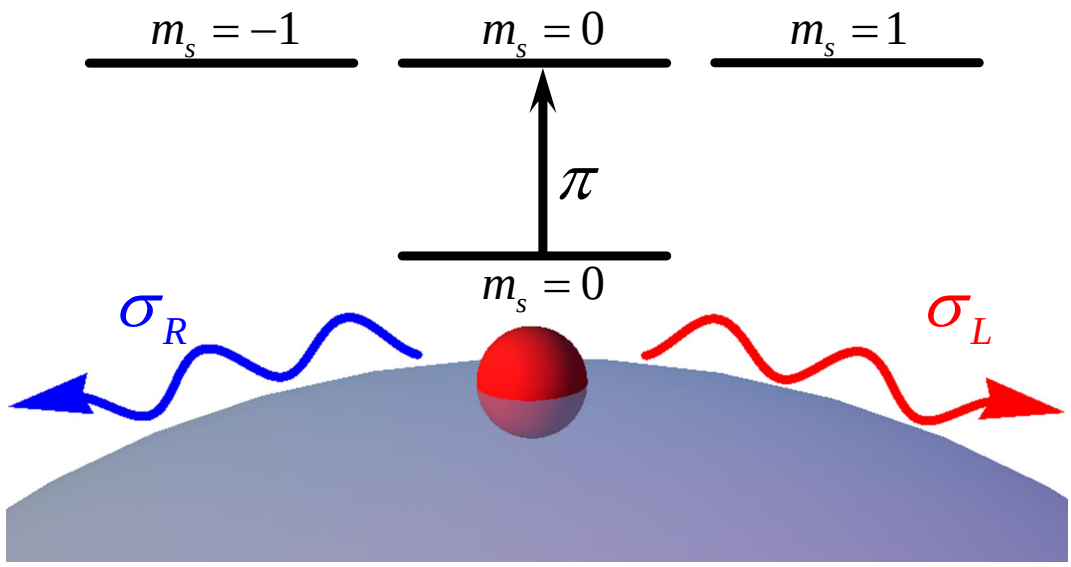

FIGURE 2.9: The north pole of the spherical resonator where a single spin (red sphere) is located. The energy level diagram of the spin is presented where the emission of a π transition into a super position of σ_L and σ_R circularly polarised light is depicted. The two circular polarisations correspond to two counter propagating fundamental WGMs.

There are two possible approaches that can be made to re-establish indistinguishability of the modes and hence the enhancement of the coupling. The first becomes apparent when considering Fig.2.7. At a specific depth inside of the sphere, the azimuthal, or, in the case of the rotated modes, polar component of the TM field is negligible while the radial component reaches a maxima. If the spins are placed at this location they will interact with the N WGMs identically and hence the coupling strength will benefit from a $\sqrt{N}$ enhancement. The second approach involves the placement of the spins away from the transversal point, where they will simultaneously interact with counter propagating modes. As mentioned above, it has been observed that the non-transversal TM fields of the WGMs couple to degenerate $\Delta m_s = \pm 1$ transitions in an atom, depending on the "handedness" of the mode's polarisation, see Fig. 2.9 [100]. If the first spin is initialised in the $m_s = 0$ level of the optically excited state while the second spin and the resonator are initialised in the ground state, the excited spin simultaneously couples to both CW (σ_L) and CCW (σ_R) WGMs. This interaction can be described by the Hamiltonian,

$$\hat{H}_I = \hbar \frac{g}{\sqrt{2}} \sum_{\text{odd } i}^{N} (\hat{\sigma}_+^{(+1)} \hat{a}_i + \hat{\sigma}_-^{(+1)} \hat{a}_i^\dagger) + \hbar \frac{g}{\sqrt{2}} \sum_{\text{even } i}^{N} (\hat{\sigma}_+^{(-1)} \hat{a}_i + \hat{\sigma}_-^{(-1)} \hat{a}_i^\dagger), \tag{2.83}$$

where $\hat{\sigma}_+^{(\pm 1)}/\hat{\sigma}_-^{(\pm 1)}$ denote the atomic raising and lowering operators associated with the $\Delta m_s = \pm 1$ transitions with zero detuning. This Hamiltonian is similar to Eq. 2.22 except here polarisation dependent coupling is considered. Under these dynamics the $m_s = 0$ optically excited spin will emit π-polarised light into a superposition of the σ_L (CW) and σ_R (CCW) polarised WGMs, see Fig. 2.9. This approach allows for the coupling enhancement to be achieved at any radial position. However, as shown in Eq. 2.83, a factor of $\sqrt{2}$ decrease of the collective enhancement occurs as CW and CCW WGMs now couple in pairs to each spin.

The sensitivity of the enhanced coupling strength to miss-positioning and miss-alignment of the two antipodal spins must now be taken into account. Such imperfections generate some level of distinguishability of the modes as they couple with the spins and hence can reduce the enhancement. There are two sources leading to distinguishability between the modes. The first stems from the spatial dependence of the electric field intensity. If the two spins are not located exactly at the antipodes of the resonator the interaction strengths with the ensemble of modes are no longer homogeneous, due to slight differences in the electric field intensities presented by each WGM to the spins. In Fig. 2.10a the latitudinal position dependence on the fundamental WGM field strength is depicted which shows that, in the case of a 33 µm fused-silica microsphere, the intensity of the TM WGM electric field only

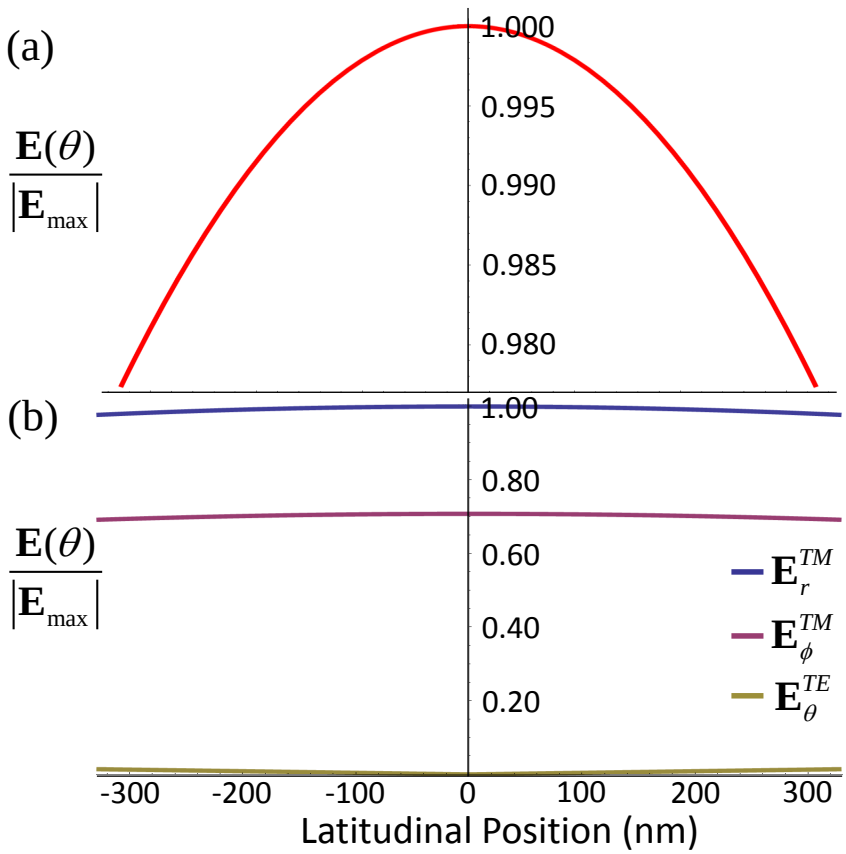

FIGURE 2.10: (a) The latitudinal variation of the TM WGM field intensity and (b) of the polarisation about the maximum intensity. The calculations were performed using a 33 μm fused-silica microsphere supporting a WGM of wavelength 637 nm.

deviates by $\sim 2\%$ at latitudinal distances ± 330 nm away from the field maximum. This means that no significant decrease in the coupling strength will be observed if the spins are located within this region, which will be confirmed in Section 2.5. Such precise positioning of nanodiamonds has been achieved through the use of an AFM tip where nanometre precision is attainable [106]. Similarly, provided the spin lies within this region, the polarisation of the modes remain essentially constant, see Fig. 2.10b. If the spin's dipole moment is not radially aligned with the electric field (i.e. if $\hat{d} \propto \hat{r} + \hat{\theta} + \hat{\phi}$), there may be coupling to both the TE and TM modes. Further, the TE modes are not degenerate with the TM modes, typically $\omega_{TM} - \omega_{TE} \approx$THz in the system studied here. This means for small linewidth spins, if the TM modes are on resonance with the spin, the TE modes are not. The effect of misalignment is then simply a reduction of the TM field coupling strength by a factor $\hat{d} \cdot \hat{e}_{TM}$.

Indistinguishability of the WGMs can also be destroyed if scatterers are introduced into the setup. Here there are two possible scatterers that must be considered. The first is

the spin itself. The solid state spins discussed above reside within nanodiamond particles which can be as small as 10 nm in diameter. The second scatterer stems from experimental requirements in studying spherical WGM resonators. Typically in experiments spherical WGM resonators are attached to the ends of fibre tips, see Fig.2.2c. The introduction of such a tip to the proposed setup will cause scattering of any modes which intersect the tip. In either case, such scattering not only reduces the quality factor of the resonator but also results in inter-mode coupling. For large scatterers inter-mode coupling can cause an undesired degeneracy breaking of counter-propagating modes, destroying mode indistinguishability [107]. If nanodiamonds as small as 10 nm in diameter are considered the effects of inter-mode coupling can be neglected as the inter-mode interaction strength,

$$g_M = 4\pi r_{nd}^3 \frac{\omega}{2V_M} \frac{s'-1}{s'+2}, \tag{2.84}$$

is small, resulting in negligible detuning between the two counter-propagating modes [76]. Here s' is that described by Eq.(2.75). In the case of the fibre tip, the degeneracy breaking can be limited in the proposed WGM-spin setup if the diameter of the tip is smaller then the

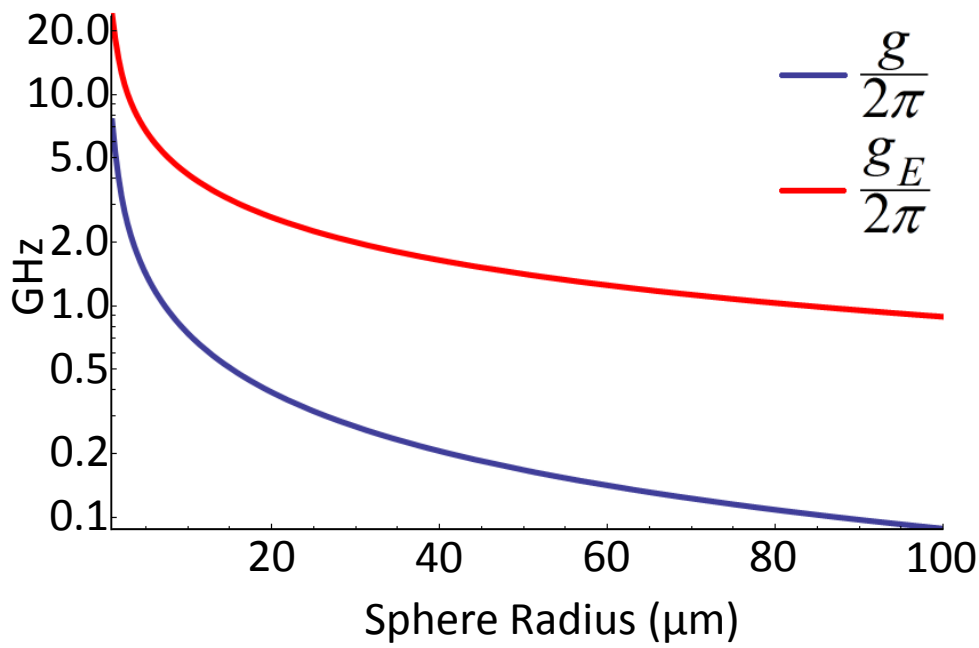

Figure 2.11: The single mode/single spin coupling rate (blue) and the multi-mode/single spin enhanced coupling rate (red) calculated as a function of sphere radius. The calculations were performed for a fused silica sphere of refractive index $n_1 = 1.46$ tuned to the ZPL of the NV center in diamond (637nm) in which the NV center, $\mu = 2.74 \times 10^{-29}$ Cm [75], was placed in the center of the fundamental WGM field maxima with a radially aligned dipole moment.

width of the fundamental WGM, $D_{tip} < W_{\frac{1}{2}}$ in Eq.(2.81). Typically this condition is met which means that the setup can be arranged such that inter-mode degeneracy breaking will only effect two of the N counter-propagating modes [108]. Thus, if the spherical resonator is attached to a fibre tip the maximal number of identical WGMs is $N - 2$.

Up until now perfect spherical symmetry has been assumed, however, in realistic experiments oblateness must be considered. In [108] a microsphere with an eccentricity of 0.001 was reported which corresponds to a deviation of less then $1\mathring{A}$ in the radius of the sphere. This small oblateness gives rise to a 100 MHz overall spread of the resonance frequencies of the WGMs, see Eq. 2.69. To address this issue, a spin with a linewidth large enough to encapsulate each of the detuned WGMs must be considered. For a microsphere of eccentricity 0.001 this requires a spin with linewidth $\gamma > 100$ MHz. A spin with such a linewidth will interact with each of the WGMs identically as the resonant frequencies of the modes each lie within the linewidth of the spin.

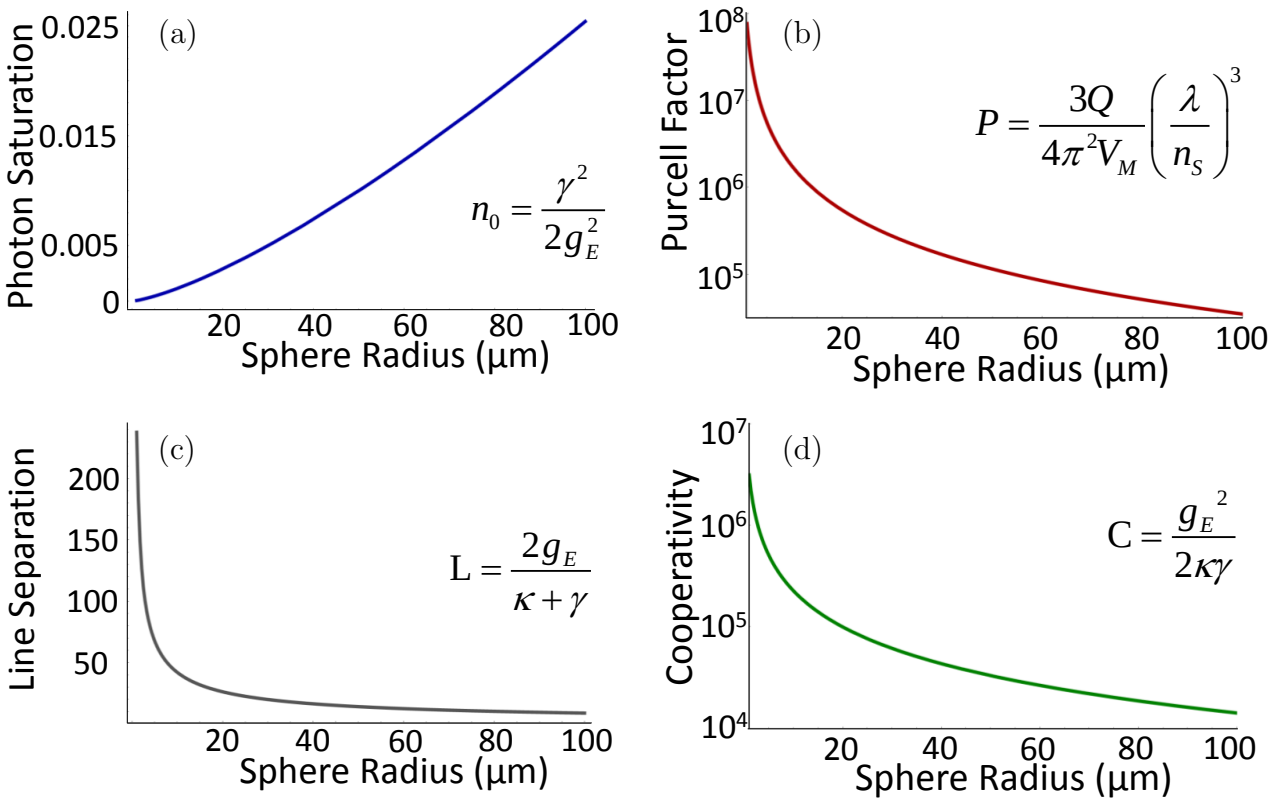

FIGURE 2.12: Ultra-strong coupling of a single spin to the collection of optical modes as a function of the microsphere radius (a) n_0 photon saturation number; (b) L the visibility of the vacuum Rabi splitting; (c) P Purcell factor; (d) C Cooperativity. For strong coupling we require $g_E > \kappa$, γ; $P \gg 1$; $L \gg 1$; $n_0 \ll 1$; $C \gg 1$.

The maximum enhancement that can be achieved for a spin located at the transversal point can now be calculated. To perform these calculations a radially aligned spin will be considered, that is, a spin with $\hat{d} \cdot \hat{r} = 1$, which is positioned in the center of the WGM field maxima ($|\mathbf{E}|/E_{max} = 1$). As mentioned above the calculations will be made using the optical transition of the NV center in ND and at low temperatures $\xi \approx 1$. Nanodiamonds of radius $r_{nd} = 5$ nm and refractive index $n_{nd} = 2.42$ will be used here as this is typically the smallest size NDs containing only a single NV center can be, minimising scattering losses. Using Eq.(2.82) and the fact that $g_E = \sqrt{N}g$, where N is given by Eq.(2.81), coupling strengths on the order of GHz can be reached using spheres with radii less than 100 μm, see Fig.2.11. In conjunction with Eq.(2.76) and $\kappa = 2\pi\omega/Q$ these results can also be used to determine whether or not the strong coupling regime can be reached using the WGM-spin setup and examine its scalability. To do so, the photon saturation number, n_0, cooperativity, C, Purcell factor, P, and the visibility of vacuum Rabi splitting, L, are plotted as a function of sphere radius, Fig.2.12, as these parameters are commonly used to analyse strong coupling. These parameters are useful as n_0 describes the number of photons required to saturate the atomic transition, the cooperativity is a measure of the coupling strength in relation to dissipation and the Purcell factor denotes the decrease in spontaneous emission due to the Purcell Effect. The spontaneous emission rate γ of the NV center in a ND ranges between $2\pi \times 10$ MHz to $2\pi \times 1$ GHz [109], depending on its temperature and internal structure. To ensure each of the rotated WGMs are encapsulated within this linewidth $\gamma = 2\pi \times 200$ MHz was used in the calculations. The results show that the strong coupling scales very nicely with the radius of the sphere and that the regime can be easily reached, even with 100 μm radius spheres.

2.5 Numerical Simulations

The theory behind the evolution of a dissipative multi-mode system as well as the interactions between individual spins and an ensemble of WGMs has now been established. By combining these results it is possible to perform realistic simulations of the proposed WGM-spin system. In this section the dynamics of several versions of this system will be considered with the aim to achieve high fidelity transfer of an excitation between two distant spins, or clusters of spins. To start, the dynamics of the interaction between a single NV center and an ensemble of identical WGMs will be simulated to demonstrate the enhancement to the coupling strength the system can achieve at low temperatures. Transfer of an excitation between two antipodal spins will then be simulated, also at low temperatures, then extended to consider inhomogeneous coupling and two antipodal clusters.

To perform these simulations a fused silica microsphere ($n_1 = 1.46$) of radius $a = 33$ µm suspended in medium of refractive index $n_2 = 1$ is considered. Through the use of Eq.(2.82) the coupling strength for such a system can be calculated to give $g = 2\pi \times 249$ MHz at low temperatures. Also, it is assumed that the spin is located at the transversal point in the center of the WGM field maxima, to ensure that it interacts with each of the rotated WGMs identically. As discussed in the previous section, an NV center in ND with linewidth $\gamma = 2\pi \times 200$ MHz will be considered and the damping rate of a cavity containing a single ND of radius $r_{nd} = 5$ nm can be calculated to give $\kappa = 2\pi \times 156$ kHz. The dynamics of the multi-mode/single spin system can be attained by solving Eqs.(2.36, 2.37) for $\kappa_i = \kappa$, $\gamma_i = \gamma$, $M = 1$ and $N = 58$, found using Eq.(2.81). To compare against previous work, where spherical symmetry was deliberately destroyed to assure only a single WGM coupled to the spin, simulations of the $M = N = 1$ case are also performed. In the case of zero detuning Fig.2.13 shows the Rabi-oscillations of the spin occupation at low temperatures when the spin is coupled to both a single WGM and an ensemble of rotated WGMs. To perform this simulation the excitation was initialised in the spin, that is, $|\psi(0)\rangle = |0\rangle|e\rangle$. The results clearly show that a much larger Rabi-frequency is achieved in the multi-mode case compared to the single mode case. This shows that the proposed WGM-spin system should be able to achieve effective coupling strengths much larger than those achieved in previous work.

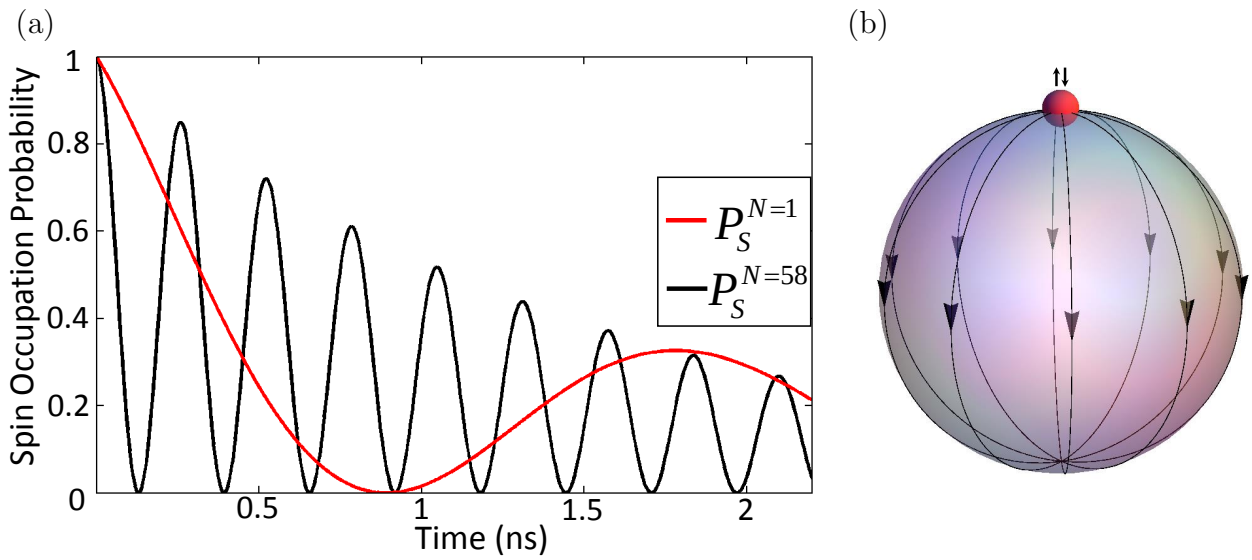

FIGURE 2.13: (a) The Rabi-oscillations of a spin which is coupled to both a single WGM (red) and an ensemble of degenerate WGMs (black) where $P_S = \mathrm{Tr}\,[\hat{\rho}\hat{\sigma}_{ee}]$. There is a clear increase in the Rabi-frequency between the two cases. Both simulations were performed using the parameters discussed in the text. A picture of the system is also shown in (b) where the spin (red sphere) is located at the north pole of the spherical resonator. The black arrows represent each of the rotated WGMs.

The next step is to determine whether or not the excitation can be efficiently transferred between two distant spins. Simulations of this excitation transfer can be performed by increasing the number of spins in the system to $M = 2$ and solving Eqs.(2.36, 2.37) in a similar manner to above. Despite this requiring the introduction of a second, antipodal ND, the increase in the optical damping rate is negligible. To visualise the excitation transfer the total spin occupation probability, $\mathrm{Tr}\left[\hat{\rho}\sum_i^2 \hat{\sigma}_{ee}^i\right]$, is plotted in Fig.2.14. In this case the system was initialised in the state $|\psi(0)\rangle = |0\rangle|e_1\rangle$, which corresponds to the first antipodal spin being excited while the second spin, and the N WGMs, are in the ground state. The results of this evolution show that the excitation is transferred between the two spins, which are located 66 μm apart, with ∼84% fidelity after ∼200 ps. The effect of inhomogeneous WGM-spin interactions on the enhanced coupling strength were also simulated, Fig. 2.14. In the case of a randomly sampled 2% decrease in the maximum coupling strength only a minor decrease to the enhanced coupling strength can be observed. To compare against previous experiments the effective interactions via a single WGM were also simulated, showing significantly lower frequency oscillations.

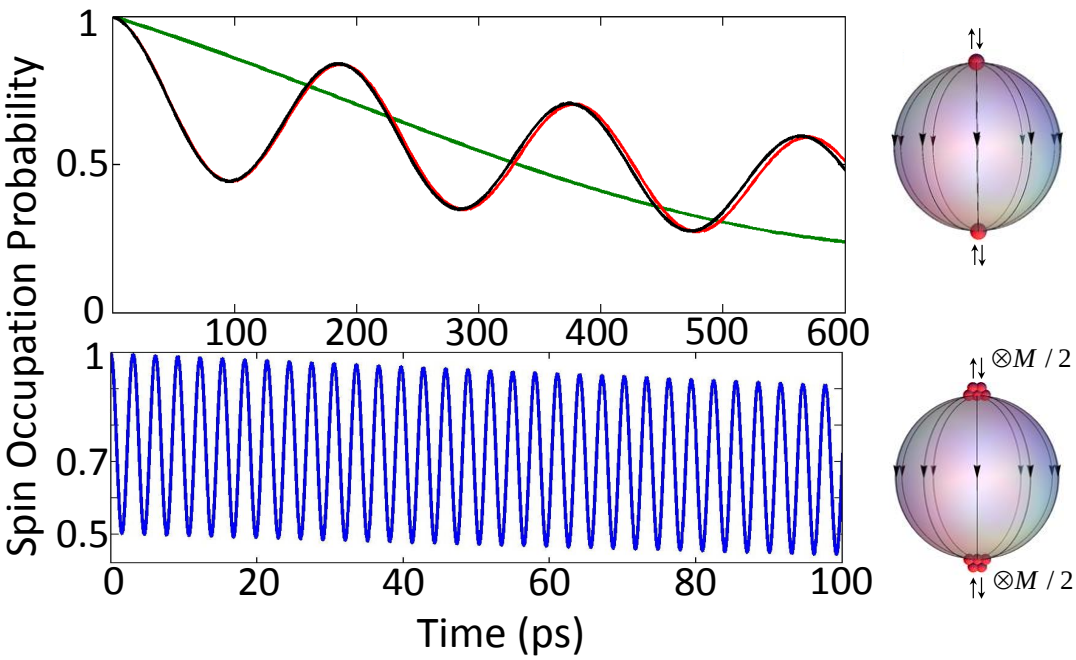

Figure 2.14: Simulations of the total spin occupation probability, $\mathrm{Tr}\left[\left(\sum_i^M \hat{\sigma}_{ee}^i\right)\hat{\rho}\right]$, for two antipodal spins coupled to a single WGM (green curve) and an ensemble of WGMs in a fused-silica resonator with homogeneous/inhomogeneous coupling (black/red curves) and two clusters of 2070 antipodal spins within a diamond resonator (blue curve). The simulations for the silica resonator were performed using $g = 2\pi \times 249$ MHz, $\kappa = 2\pi \times 156$ kHz, $\gamma = 2\pi \times 200$ MHz and a 2% random coupling inhomogeneity. For the diamond resonator $g = 2\pi \times 334$ MHz, $\kappa = 2\pi \times 109$ kHz and homogeneous coupling was considered.

As was seen in Section 2.2.4 an alternative method to achieve higher fidelity transport of the excitation involves the introduction of many spins into the multi-mode system. This is because the introduction of M spins results in a further factor of $\sqrt{M}$ enhancement to the coupling strength. Here two antipodal clusters of $M/2$ identical spins are considered. The maximum number of spins which can be included in each cluster without the loss of quantum interference can be approximated by first assuming that each of the spins are separated by $\delta = 50$ nm, to avoid spin-spin interactions. To assure that the constructive quantum interference is not lost, the WGM-spin coupling must be identical for each of the spins, which limits the largest volume the spins can occupy to λ^3. The maximum number of spins in each cluster is then,

$$\frac{M}{2} = \frac{\lambda^3}{\delta^3} \approx 2070. \tag{2.85}$$

However, this requires the placement of two antipodal NDs of volume $V_{ND} \approx \lambda^3$ inside the sphere, close to its surface. Introduction of these much larger NDs results in a significant increase to the optical damping rate and in inter-mode coupling, due to scattering. These effects can be avoided if a diamond spherical resonator is considered. Here the maximum number of spins is essentially limited by Eq.(2.85). Simulations are performed in this case where the system is initialised in the state $|\psi(0)\rangle = \sum_{i=1}^{M/2} |0\rangle|e_i\rangle$, corresponding to the excitation residing within the first cluster. At low temperatures the huge collective enhancement results in a number of $\geq$99% fidelity excitation transfers between the two antipodal clusters within 100 ps, shown in Fig.2.14.

2.6 Conclusion

In this chapter a hybrid quantum system designed to achieve strong coupling between distant spins was proposed. The proposed system consisted from a spherical WGM resonator in which spins were placed at the antipodes. It was shown that a spherical resonator of radius a could be used as a $N \propto \sqrt{a}$ degenerate mode cavity, where each of the modes corresponded to a rotated fundamental WGM. Analogous to the effective enhancement to the coupling strength achieved in the many spin extension of the JC model, it was shown that the many mode extension can provide an identical enhancement. However, achieving this enhancement required that the interaction between the spin and each of the rotated WGMs was identical, which essentially required that the spin was placed at a specific depth inside the sphere. Finally, several simulations were performed showing that enhanced coupling strengths on the order of GHz could be achieved using the WGM-spin system, an order of magnitude larger than those obtained in previous work. It was then shown that this enhancement could

be used to efficiently transport excitations between spins separated by almost 100 μm and that significantly larger coupling strengths could be achieved by considering distant clusters of spins. When two antipodal clusters were considered the system was capable of achieving a number of extremely high fidelity excitation transfers. Overall the proposed WGM-spin system was shown to provide an excellent, experimentally accessible and relatively scalable platform for achieving strong coupling which is applicable in many quantum technologies. Further, the results show that the WGM-spin system can be used to construct large, strongly coupled, cQED arrays in which each spin can be individually addressed with optical light.

Chapter 3

Deterministic Creation of Cat-States using Membrane in the Middle

3.1 Introduction

Despite current technological advances, quantum mechanical effects have yet to be observed outside of the nanoscopic realm. Observation of these effects on larger scale systems have been intensively pursued since the development of quantum mechanics as they would demonstrate the existence of quantum mechanical states which reside at the borders of the classical and quantum worlds. The creation of such 'macroscopic' quantum states is currently one of the most attractive goals in quantum mechanics allowing not only for the direct study of quantum state collapse models [28] but for their extension to potentially practical applications in quantum information, metrology, teleportation, cryptography, simulation, and even to potentially improve understanding of complicated biological processes [55, 110–115].

The most intuitive approach which has been commonly made to observe and study quantum mechanical effects on larger scales involves the up-scaling of systems which are already known to behave quantum mechanically. In particular, extensive efforts have been made to upscale the well-known double slit experiment in hope to observe wave like behaviour of particles much larger than electrons. Such experiments correspond to creating macroscopic superpositions, where here, macroscopic can refer to systems comprised from 10^2 up to 10^{10} particles or smaller size systems which exhibit quantum mechanical effects over long distances [116]. To date, wave like behaviour has been reported with the use of particles ranging from single atoms all the way to organic molecules containing several hundreds of atoms [117–119]. Macroscopic quantum tunnelling has also been addressed and observed,

for example in Josephson Junctions [120], though, it is the creation of macroscopic superpositions and entangled states which is significantly more sought after due to the broader range of applications. Of particular interest is the creation of states which are analogous to the famous Schrödinger's cat state due to both their simplicity and their completely quantum mechanical nature. In the field of quantum optics, photonic forms of the Schrödinger's cat state are also studied. These states are commonly referred to as cat states and often correspond to superpositions between two orthogonal coherent states of the electromagnetic fields in cavities.

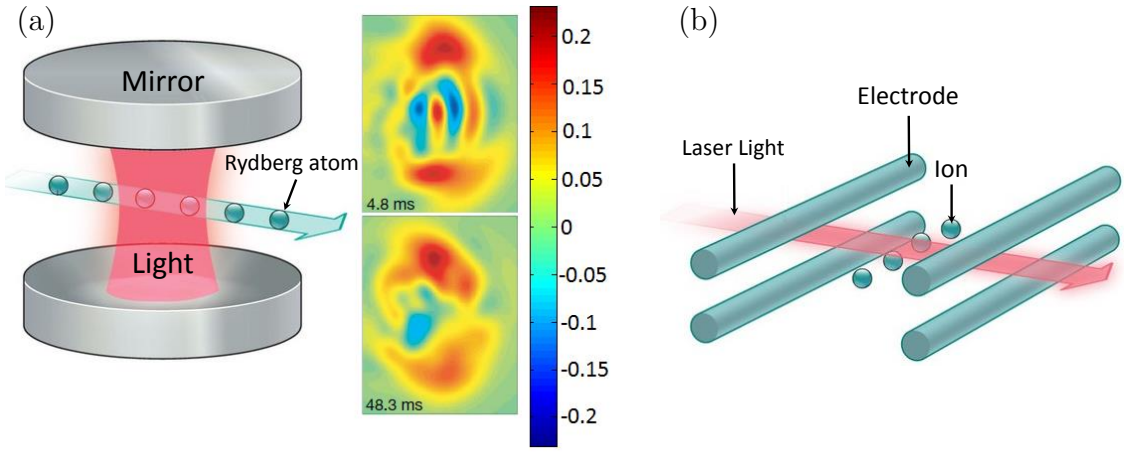

Figure 3.1: Experimental setups used by both the Haroche (a) and the Wineland (b) groups to create quantum states [121]. A cat state was created in (a) by interacting Rydberg atoms with coherent light. The Rydberg atoms entered the cavity in the state $|\psi_i\rangle \propto |e\rangle + |g\rangle$ and the resulting Stark shift induced a phase on the coherent amplitude of the cavities state. After application of a $\pi/2$ pulse the state of each atom was measured, projecting the cavity into a cat state. The Wigner function of the resulting cat state is shown in the right half of (a) where negative values depict the 'quantumness' of the state [20]. A Schrödinger's cat state was created in (b) by initialising a trapped ion in $|\psi_i\rangle$ and introducing a light field [19]. This caused the ion to be conditionally displaced depending on its internal state.

Widespread efforts have been made to construct large scale quantum states analogous to the Schrödinger's cat state. The main difficulties in the creation of these states stem from destructive interactions between the quantum system and the surrounding environment, otherwise known as decoherence. Typically these interactions increase with the size of the system causing loss of the desired quantum coherence. Of particular interest is understanding how spatial quantum superpositions become classical. Such understanding requires the creation of quantum states that correspond to an object being located in two separate positions simultaneously. Only few experiments have been conducted which have successfully created such states. The most influential were those conducted by the 2012 noble prize winners, Serge Haroche and David Wineland. The Haroche group conducted an experiment

which provided significant insights into the effects of decoherence on quantum superposition states of microwave photons confined within a cavity as these effects were continuously measured, essentially producing a video of the state decohereing, see right half of Fig.3.1a [20]. This was the first and, to date, only experiment to provide a real time visualisation of decoherence. The state which was observed was a coherent superposition state of light, often referred to as a cat state, as mentioned above. Remarkably, the state of the light field could be repeatedly measured indirectly, as each measurement was performed on atoms which were individually entangled with the field, rather than on the cavity field itself, see left half of Fig.3.1a. While the state created in this experiment is not macroscopic, it still stands as one of the largest coherent superposition states which has ever been observed. Larger scale spatially entangled states, however, have been somewhat routinely observed over the past two decades. The Wineland group was the first to observe quantum entanglement between an ions spatial position and its internal state. In this experiment the dipole force due to incident light was exploited to conditionally displace the ion depending on its internal state, see Fig.3.1b. The spatial displacement between the two ion positions achieved was 83 nm [19], which also remains one of the largest distances achieved between spatially entangled states of a single atom. To further study decoherent effects these results have been up-scaled by entangling up to six trapped ions using similar methods [122–125]. Creation of these types of quantum states with particles beyond atomic sizes, however, has yet to be achieved experimentally.

With the intention of creating macroscopic quantum states many researchers have directed their attention towards the field of optomechanics. This field of quantum optics focuses on the interactions between mechanical oscillators and light. Some of the more common optomechanical systems which are studied involve cavities that are comprised from two mirrors, one fixed and one moveable. The radiation pressure force due to the light confined within the cavity causes the second mirror to move, acting as a mechanical harmonic oscillator. Other types of optomechanical systems consider placing mechanical oscillators within Fabry-Pérot type optical cavities. Such systems have inherited the name “Membrane in the Middle” where the mechanical oscillator is referred to as the membrane [126]. Several types of membranes have been used in such setups, ranging from solid silicon nitride crystalline, flexible 2D films, through to Bose-Einstein condensates (BEC) [127–129]. There are many possible variations of these optomechanical setups which have been both studied and used as a platform for cat state creation [21–29]. Of these, perhaps the most macroscopic proposed involves a tiny mirror, consisting from 10^{14} atoms, which acts as a mechanical oscillator. However, this setup has so far only achieved spatial separations on the order of femtometres with extremely demanding experimental conditions [21].

While the creation of cat states can be somewhat guaranteed after entangling the position of an oscillator with a single photon or qubit, creating such states using larger systems requires measurement thus making the creation process probabilistic. In this chapter a novel, completely deterministic method of creating cat states of the position of a macroscopic object will be proposed. These states will be created by exploiting properties in the optomechanical Membrane In The Middle (MITM) setup [126]. It will be shown that by controlling the membrane's opacity its displacement can be driven at a rate proportional to the number of photons in the system. This will be achieved by effectively switching the membrane's opacity between a highly opaque and a transparent state, as shown in Fig.3.2. This technique will be used as a mechanism to create and deterministically grow the spatial extent of a quantum cat state. Before a cat state is produced, however, to ensure that the lifetime of the state is not limited by the finesse of the optical cavity the scheme requires disentanglement of the membrane's final position from the two cavity modes. Disentangling such a state using the MITM model alone is extremely challenging experimentally, essentially requiring that the membrane's opacity is also spatially dependent. Instead, an alternative deterministic disentanglement protocol will be proposed as the final step in creating the cat state. To demonstrate the accessibility of the cat state creation scheme a possible experimental setup

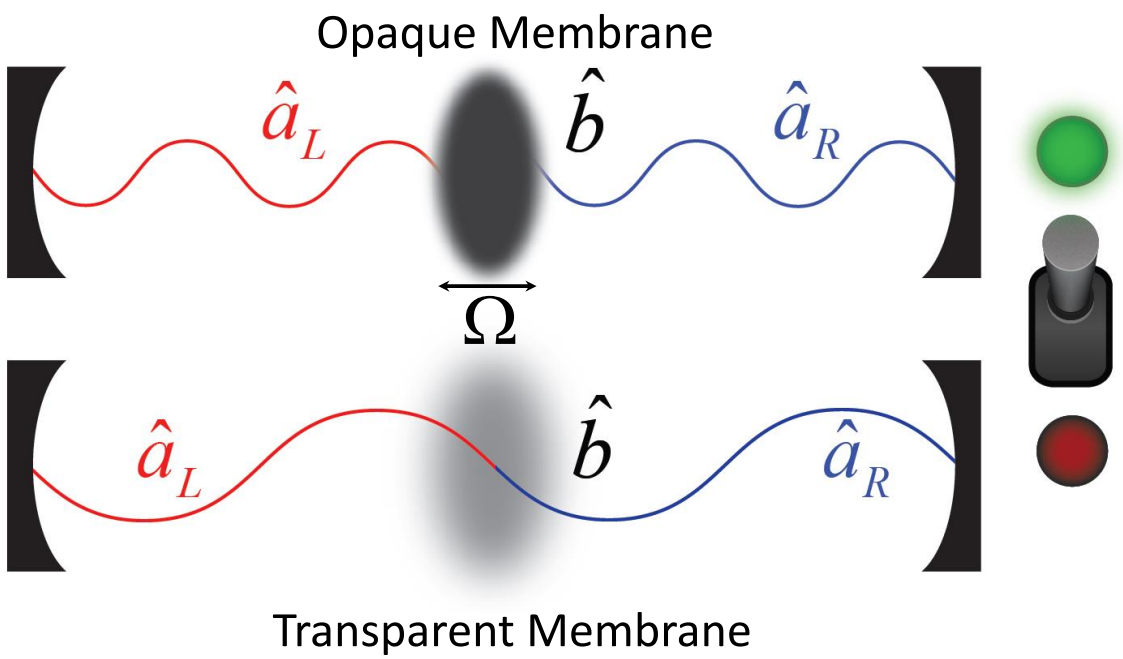

FIGURE 3.2: A depiction of the Membrane in the Middle setup is shown in two separate cases. The top cavity contains a highly opaque membrane while the bottom contains a transmissive membrane. The switch represents the control over the membrane's opacity, where 'on' corresponds to an opaque membrane and 'off' to a transmissive membrane.

using optical frequency light will be discussed. Finally, using a BEC type membrane, it will be shown that the proposed scheme is capable of creating high fidelity cat states with spatial displacements of up to ~ 300 nm using only a small photon occupation.

This chapter is dedicated to proposing a deterministic protocol for macroscopic cat state creation. To do so, the chapter will be split into four sections. Each section will correspond to a different process in the cat state creation protocol. As mentioned above the platform which will be used to generate macroscopic cat states is the MITM model. The first section of this chapter will focus on the dynamics of this model and the effects of controlling the membrane's opacity. Here the theory behind the MITM model will be briefly introduced then the dynamics of the system in the two different opacity regimes will be studied. The purpose of this section is to show that the membrane's position can be driven to achieve large spatial displacements. It is this driving of the membrane's position which will be used to 'grow' the cat state. The second section of this chapter will focus on the creation of cat states using the MITM model. It will be shown that this requires a two step process. The membrane's position must first be entangled with the two optical cavity modes and then deterministically disentangled to produce a cat state. In this section both the entanglement and the disentanglement protocols will be discussed. With the theoretical protocol established, Section 3.4 will be dedicated to proposing a possible experimental platform where effective control over the membrane's opacity can be achieved. Here the entire macroscopic cat state creation protocol will be incorporated into the experiment and a step by step explanation will be provided. The final section of this chapter will provide numerical simulations of the membrane's dynamics for several experimental conditions where the resulting macroscopic cat states will be visualised through the use of the Wigner function.

3.2 The Membrane in the Middle Model

The overarching goal of this work is to deterministically create a cat state of a mechanical object's position. As mentioned above one approach which has been previously made involves the introduction of mechanical oscillators into Fabry-Pérot type cavities (MITM). Here a similar approach will be made but with the included consideration of controlling the mechanical oscillator's opacity. To do this will first require establishing theory to describe the MITM model. The first half of this section will provide a brief introduction to the MITM model where the form of the light-matter interactions will be discussed. Next, in the second half of this section, the effects of controlling the opacity of the membrane will be studied where two extreme cases will be considered. These cases correspond to either an opaque or

a highly transmissive membrane. Finally, it will be shown that by alternating between these two opacity states the spatial displacement of the membrane can be driven.

3.2.1 Introduction to MITM

The Membrane in the Middle model describes an optomechanical system which is comprised from two degenerate modes of a cavity which interact with a physical membrane that is confined within the cavity, shown in Fig.3.2. The Hamiltonian for this model can be split into four main portions. These include; $\hat{H}_0^C$, describing the self energies of the cavity modes, $\hat{H}_0^M$, that of the membrane's motion, $\hat{H}_T$, which describes the transmission of light through the membrane and $\hat{H}_{int}$ the interaction energy. The self energy terms are given by,

$$\hat{H}_0^C = \hbar\omega \left(\hat{a}_L^\dagger \hat{a}_L + \hat{a}_R^\dagger \hat{a}_R\right), \tag{3.1}$$

$$\hat{H}_0^M = \hbar\Omega \hat{b}^\dagger \hat{b}, \tag{3.2}$$

where $\hat{a}_L/\hat{a}_R$ denote the annihilation operators of the left/right cavity modes with frequency $\omega = \omega_L = \omega_R$ and $\hat{b}$ that of the membrane's mechanical motion with frequency Ω. In what follows optical frequency modes will be focused on, for practical purposes. The transmission term describes the transfer of photons between the left/right cavity modes through the membrane. It can be described by,

$$\hat{H}_T = -\hbar J \left(\hat{a}_L^\dagger \hat{a}_R + \hat{a}_R^\dagger \hat{a}_L\right), \tag{3.3}$$

where J is the transmission rate of the membrane. Finally, the interaction term describes the photon pressure force of the cavity mode photons acting on the membrane. This interaction requires that the wavelength of the optical modes satisfies $\lambda_c \ll l, h$, where l/h represent the membrane's length/height. The photon pressure force can be expressed as $\hat{F} = -\frac{\omega}{L}\hat{x}\hat{a}^\dagger\hat{a}$, where $\hat{x} = x_{ZPF}(\hat{b}^\dagger + \hat{b})$ is the position operator of the membrane, $x_{ZPF} = (\hbar/2m\Omega)^{1/2}$ the zero point fluctuation amplitude and L is the length of the individual cavities. The interaction term is then expressed as,

$$\hat{H}_{int} = -\hbar g_0 \left(\hat{b}^\dagger + \hat{b}\right)\left(\hat{a}_L^\dagger \hat{a}_L - \hat{a}_R^\dagger \hat{a}_R\right), \tag{3.4}$$

where $g_0 = \omega x_{ZPF}/L$ is the optomechanical coupling strength. The Hamiltonian of the entire system is now $\hat{H}_{MITM} = \hat{H}_0^C + \hat{H}_0^M + \hat{H}_T + \hat{H}_{int}$. By noticing that $\left[\hat{H}_{MITM}, \hat{H}_0^C\right] = 0$

this Hamiltonian can be reduced in the interaction picture of the cavity modes to give,

$$\hat{H}_I = \hbar\Omega\hat{b}^\dagger\hat{b} - \hbar J\left(\hat{a}_L^\dagger\hat{a}_R + \hat{a}_R^\dagger\hat{a}_L\right) - \hbar g_0\left(\hat{b}^\dagger + \hat{b}\right)\hat{\Delta}, \tag{3.5}$$

where the difference operator $\hat{\Delta} = \hat{a}_L^\dagger\hat{a}_L - \hat{a}_R^\dagger\hat{a}_R$ has been introduced.

3.2.2 Controlled Transmission in the MITM Model

With the theory behind the MITM model established the effects of controlling the transmission rate, $J(t)$, can be studied. Two extreme cases of J can be considered. The first corresponds to a highly opaque membrane, in particular when $J \ll g_0,\ \Omega$. In this case $\hat{H}_I$ approximately reduces to,

$$\hat{H}_I^{(1)} = \hbar\Omega\,\hat{b}^\dagger\hat{b} - \hbar g_0\left(\hat{b}^\dagger + \hat{b}\right)\hat{\Delta}. \tag{3.6}$$

This Hamiltonian describes a driven harmonic oscillator where the driving strength is directly proportional to not only the optomechanical coupling rate but also to the difference in the photon numbers between the optical modes. In the case where $\hat{\Delta}$ is treated as a classical number Eq.(3.6) corresponds to harmonic motion about a displaced position, which will be used to interpret later results. Under the evolution of $\hat{H}_I^{(1)}$ the difference in photon numbers between the left and right cavities is conserved, as $\left[\hat{H}_I^{(1)}, \hat{\Delta}\right] = 0$, significantly simplifying the solutions to the Heisenberg equations of motion, see Appendix C. These solutions show, ignoring dissipative effects, that when starting in an initial state $|\psi_0\rangle = |\beta_M, \alpha_L, \alpha_R\rangle$, corresponding to the membrane initially in a coherent state β_M and the left/right cavity modes in coherent states α_L/α_R, the expectation value of the membrane's position evolves as,

$$\langle\hat{x}\rangle = \frac{4g_0 x_{ZPF}}{\Omega}\Delta\sin^2\left(\frac{\Omega t}{2}\right) + x_{ZPF}\left({\beta_M}^* e^{i\Omega t} + \beta_M e^{-i\Omega t}\right), \tag{3.7}$$

where $\Delta = |\alpha_L|^2 - |\alpha_R|^2$. This expectation value shows that if the state of the left and right cavity modes could be completely interchanged at times satisfying $\Omega t = \pi(2n+1)$, the position of the membrane could be driven to even larger spatial extensions, see Fig.3.3 and 3.5. The reason for this is that interchanging the state of the left and right modes effectively switches the phase on the interaction term in Eq.(3.6), that is, $-g_0\Delta \leftrightarrow g_0\Delta$. This results in the achievement of an extra membrane displacement of $4x_{ZPF}\Delta\frac{g_0}{\Omega}$ after every photon number interchange. One way to interpret the effect of the phase on the optomechanical driving term is to consider the direction of the membranes displacement. For example, if the system is initialised in the state $|\psi_0\rangle = |0_M, \alpha_L, \alpha_R\rangle$ with $\Delta > 0$ the phase on

the optomechanical driving term is $-$ and the membrane is displaced by $4x_{ZPF}\Delta\frac{g_0}{\Omega}$ in the positive x direction. Alternatively, if the system is initialised in the state $|\psi_0\rangle = |0_M, \alpha_R, \alpha_L\rangle$ the phase on the driving term will be $+$ and thus the membrane will be displaced by the same amount, but in the opposite direction. An alternative explanation can be made in the displaced harmonic oscillator picture to easily visualise the protocol described to increase the membrane's maximal displacement. The separate $\pm$ phases of the optomechanical driving term correspond to two separate quadratic potentials which are symmetrically displaced about the origin, as shown in Fig.3.3. Carefully timing the optomechanical phase switching to occur when the membrane has reached a maximal displacement in one harmonic potential is analogous to shifting the membrane to the other, displaced, harmonic potential, where the potential energy is larger. If this process is repeated by switching the membrane between the two symmetrically displaced harmonic potentials its energy can sequentially be increased to achieve larger and larger spatial displacements, Fig.3.3 and 3.5.

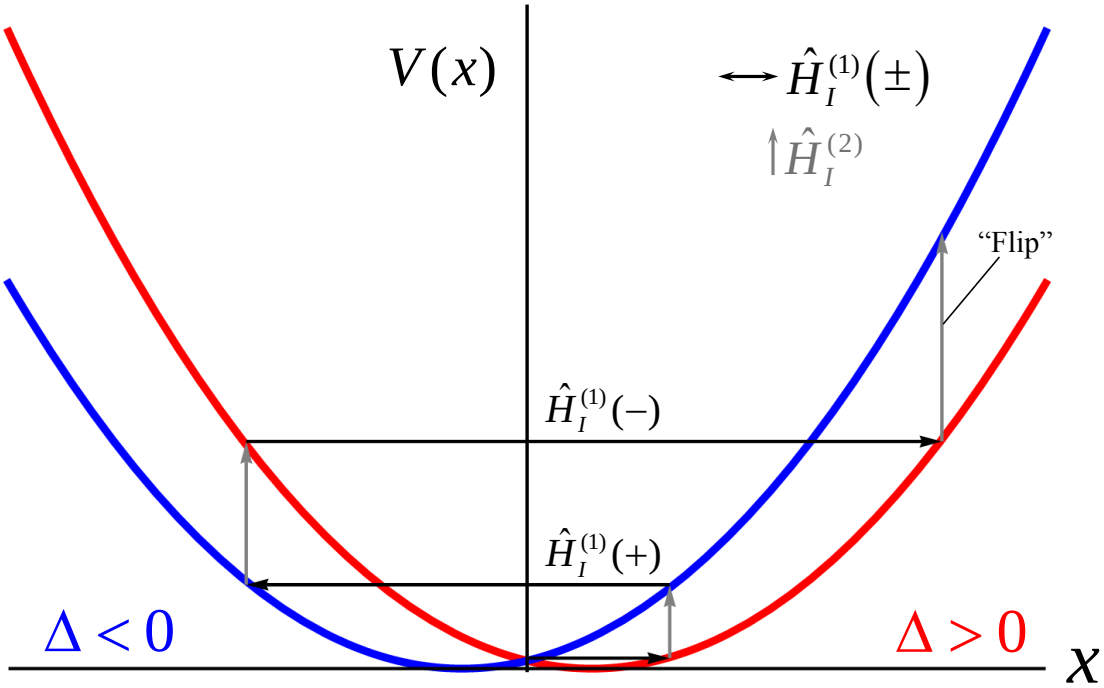

FIGURE 3.3: Classical visualisation of driving the membranes displacement by alternating the system between the two symmetrically displaced potential wells. The horizontal arrows represent the evolution of the membrane's position in the high opacity regime, $\hat{H}^{(1)}$, while the vertical arrows represent evolution in the transparent membrane regime, $\hat{H}^{(2)}$, or, the flipping of the cavity states. The sign $\hat{H}^{(1)}(\pm)$ denotes the phase on the optomechanical driving term. Here the system is initialised in the state $|\psi(0)\rangle = |0_M, \alpha_L, \alpha_R\rangle$ with $\Delta > 0$.

In order to drive the displacement of the membrane a method of interchanging the state of

the left/right cavities must first be established. As this requires the flow of photons through the membrane, the second limiting case of J will now be considered. That is, the case of an almost completely transparent membrane. In this case, as $J \gg g_0$, Ω, the transmissive term in Eq.(3.5) dominates and the Hamiltonian approximately reduces to,

$$\hat{H}_I^{(2)} = -\hbar J \left(\hat{a}_L^\dagger \hat{a}_R + \hat{a}_R^\dagger \hat{a}_L \right). \tag{3.8}$$

By again working in the Heisenberg picture the cavity mode operators can be evolved to give,

$$\hat{a}_{L,R}(t) = \hat{a}_{L,R}(0)\cos(Jt) + i\hat{a}_{R,L}(0)\sin(Jt), \tag{3.9}$$

which shows that at times satisfying $Jt = (m + \frac{1}{2})\pi$ the left and right modes can be interchanged completely. Using the initial state $|\psi_0\rangle = |\beta_M, \alpha_L, \alpha_R\rangle$ the expectation value of the mode number operators can now be evolved to give,

$$\langle \hat{a}_{L,R}^\dagger \hat{a}_{L,R} \rangle = |\alpha_{L,R}|^2 \cos^2(Jt) + |\alpha_{R,L}|^2 \sin^2(Jt). \tag{3.10}$$

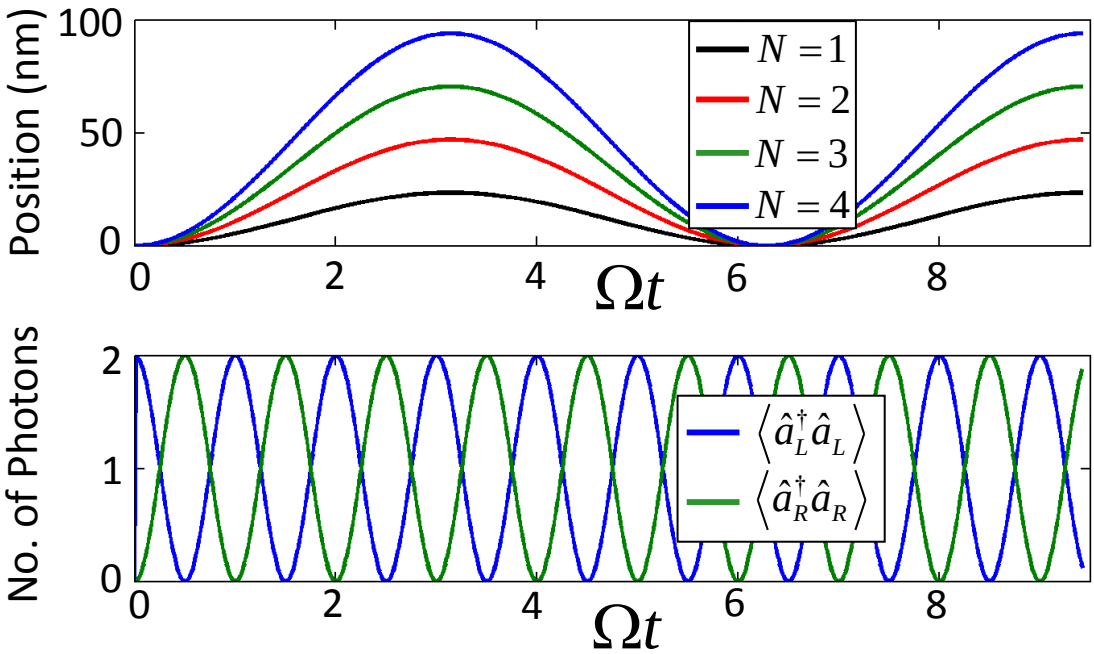

Figure 3.4: The dynamics of the MITM model in both the opaque membrane regime (top) and transparent membrane regime (bottom). In the opaque membrane regime the membrane's oscillation amplitude is directly proportional to the number of photons in the cavity N. The bottom figure shows that by evolving the system in the transparent membrane regime the number of photons in each of the cavities can be interchanged. Both results were produced via evolution of the initial state $|\psi(0)\rangle = |0_M, N, 0\rangle$ for a BEC type membrane in units of mechanical frequency.

Now that a method of interchanging, or "flipping", the state of the two cavity modes has been established the membrane's displacement can be driven in the manner shown in Fig.3.3. If the flipping process is repeated N_F times, whenever $\Omega t = \pi(2n+1)$ is satisfied, the membrane's maximal displacement will increase linearly with N_F. Ignoring dissipative effects, the unitary evolution can be expressed by,

$$|\psi(t')\rangle = \prod^{N_F} \hat{U}_2(t_2)\hat{U}_1(t_1)|\psi(0)\rangle, \tag{3.11}$$

where $\hat{U}_i = e^{-it_i\hat{H}_I^{(i)}/\hbar}$ with $\Omega t_1 = \pi(2n+1)$ and $Jt_2 = (m+\frac{1}{2})\pi$ for arbitrary integers n, m. Numerical simulations of this evolution will be performed in later sections where the effects of decoherence will be considered, however, the unitary evolution of the membrane's position is shown in Fig.3.5. This evolution will be the basis for both the creation and 'growth' of a cat state.

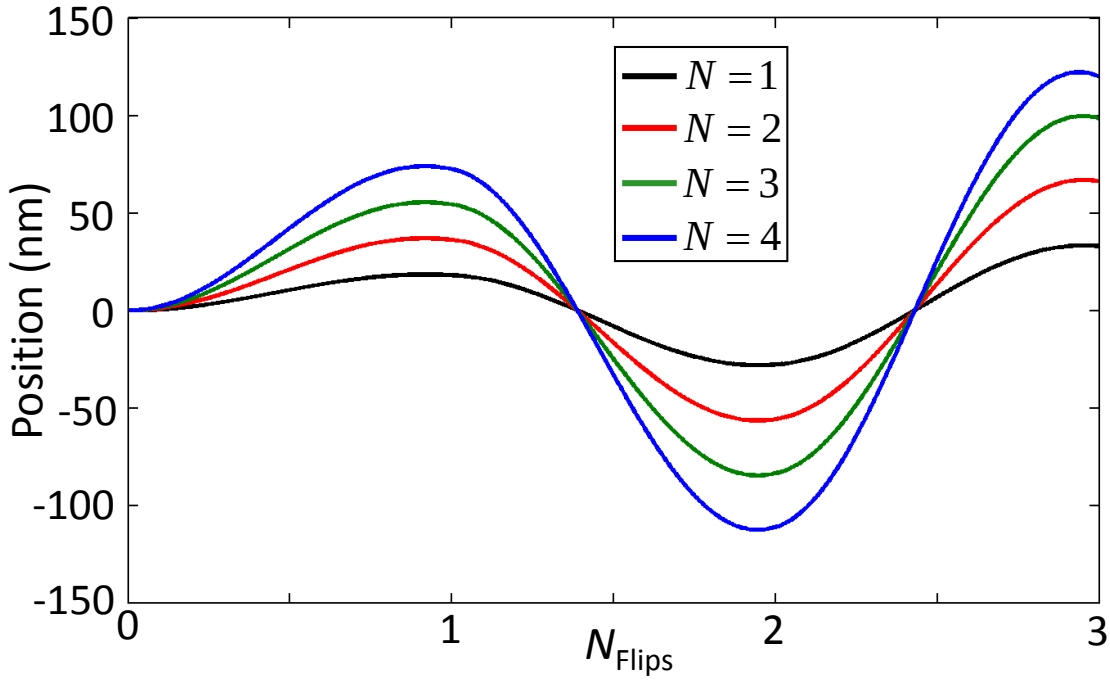

FIGURE 3.5: The dynamics of a BEC type membrane's position when evolving the initial state $|\psi(0)\rangle = |0_M, N, 0\rangle$ under the alternating evolution described by Eq.(3.11). Several values of the photon number, N, were used to demonstrate the displacement increase. The simulations were performed in units of the mechanical oscillation frequency, Ω, with $g_0 = 32.8\Omega$ and $N_{Flips} = t/\tau_{Flip} = t\frac{\Omega}{\pi}$.

3.3 Generation of a Cat State

While a possible mechanism for 'growing' the spatial extent of the mechanical cat state has been proposed, the cat state must first be created. One of the most common approaches to creating cat states is to first establish entanglement in the system. Once an entangled state is created there are many protocols which can be used to reduce the entangled state into a cat state. However, the majority of these protocols require that measurements are made on the system, projecting it into the cat state. This means that many of these protocols are completely probabilistic. In this section a similar approach to cat state creation will be made. The first half of this section will focus on establishing entanglement between the membrane's position and the two cavity modes. This entanglement will be produced by preparing the system in specific states then evolving it in the manner discussed above. Several possible initial states will be considered with the intention of maximising the spatial displacement of the membrane's position. The second half of this section will focus on disentangling the membrane from the two cavity modes to produce the desired cat state. Here, several possible disentanglement protocols which do not rely on measurement will be discussed with the use of the MITM model alone. Finally, an ensemble of atoms will be introduced into the MITM system to show that a completely deterministic and experimentally feasible disentanglement protocol is possible.

3.3.1 Initial Conditions

As mentioned above, a common approach to cat state creation is to first establish entanglement. This means that a set of initial conditions must be determined which, when evolved under Eq.(3.11), leave the system in an entangled state that can be reduced into a cat state. In the proposed system this requires the generation of quantum entanglement between the membrane's position and cavity modes. One possible approach to achieving this entanglement is to initialise the system in a state that corresponds to the membrane in its ground state while the cavity modes are in a NOON state [130]. In the MITM system the NOON state corresponds to a quantum superposition of the left cavity containing N photons while the right is empty and the right cavity containing N photons while the left is empty. The initial state can be expressed as,

$$|\psi(0)\rangle = \frac{1}{\sqrt{2}}|0_M\rangle \left(|N,0\rangle + |0,N\rangle\right). \tag{3.12}$$

By evolving this state through the use of Eq.(3.11) the membrane's position is simultaneously evolved under the two potentials depicted in Fig.3.3. After such an evolution the state of

the system is,

$$|\psi(t_E)\rangle = C\left(|\beta_M, 0, N\rangle + |-\beta_M, N, 0\rangle\right), \tag{3.13}$$

where C is a normalisation constant and β_M represents the coherent state amplitude of the membrane which depends on the number of 'flips' which have been applied as well as the number of photons in the NOON state, N. Typically NOON states are experimentally difficult to create for $N > 2$. From Eq.(3.7), it is clear that a large N is required to achieve large spatial displacements of the membrane. This means that, unless an ultra-small membrane is considered, an alternative set of experimentally feasible initial conditions is required.

There are currently two possible alternatives to initialising the cavities in a NOON state. These include (A) the coherent state analogue of the NOON state, referred to as an entangled coherent state (EC) and (B) the entangled squeezed-coherent state (ESC) [131, 132]. For possibility (A): an EC can be produced in the proposed setup by initialising the left cavity in a coherent superposition state (CSS) and the right cavity in a coherent state then evolving the system in the highly transmissive regime, Eq.(3.8) [131]. Evolution under Eq.(3.8) for the correct duration effectively acts as a 50:50 beam splitter on the two input states. If the two cavities are prepared in the states $|\psi_{CSS}\rangle = N_{CSS}\left(|\alpha\rangle + |-\alpha\rangle\right)$ and $|\psi_C\rangle = |\alpha\rangle$ then evolved under the beam splitter dynamics the state,

$$\begin{aligned} |\psi_{EC}\rangle =& \hat{B}\left(\tfrac{\pi}{2}\right)|\psi_{CSS}, \psi_C\rangle, \\ =& N_{CSS}\left(|\sqrt{2}\alpha, 0\rangle + |0, \sqrt{2}\alpha\rangle\right), \end{aligned} \tag{3.14}$$

is generated, where N_{CSS} is a normalisation constant and $\hat{B}$ the beam splitter operator,

$$\hat{B}(\eta) = e^{\frac{\eta}{2}\left(\hat{c}_1\hat{c}_2^\dagger - \hat{c}_1^\dagger\hat{c}_2\right)}, \tag{3.15}$$

for arbitrary input modes $\hat{c}_1$ and $\hat{c}_2$. While this provides a coherent state analogue of the NOON state, the creation of EC states relies directly on the generation of $|\psi_{CSS}\rangle$. Such coherent superposition states have only been demonstrated experimentally with small coherent amplitudes, $|\alpha|^2 < 3.5$, thus EC initial states with large coherent amplitudes may be beyond current experimental capabilities [20, 133].

For possibility (B): Entangled squeezed coherent states can also be generated using the proposed setup, Fig.3.2. An ESC state can be created by preparing the left mode in a squeezed state and the right mode in a coherent state then evolving the system in the highly transmissive regime, Eq.(3.8). Both squeezed vacuum states and squeezed single photon states, corresponding to initialisation with a parametrically down converted photon, have

been used to demonstrate the creation of such entangled states [134, 135]. The resulting state can be expressed by,

$$|\psi_{ESC}\rangle = \hat{B}\left(\tfrac{\pi}{2}\right)|\psi_{Sq}(s), \psi_C\rangle, \tag{3.16}$$

where the squeezed state is defined as $|\psi_{Sq}(s)\rangle = \hat{S}(s)|0\rangle$ with the squeeze operator,

$$\hat{S}(s) = e^{\frac{1}{2}\left(s^*\hat{c}^2 - s\hat{c}^{\dagger 2}\right)}. \tag{3.17}$$

The appeal of ESC states is that they strongly resemble high N NOON states where there is essentially no limit on the size of N. The largest ESC states which have been created correspond to high NOON states with $N \leq 9$ [136]. Thus, although they outperform EC states, ESC states are still far from the $N \gg 1$ NOON-like states that are needed to displace large membranes. This means that realistically only very light membranes can be considered in our proposed cat state creation protocol.

3.3.2 Disentanglement

As discussed in the previous section, to produce the desired cat state entanglement must first be established between the membrane's position and the cavity modes. This entanglement can be achieved by initialising the system in the state Eq.(3.12) and performing the evolution described by Eq.(3.11). However, this evolution leaves the system in the state, Eq.(3.13), where the membrane's position is in a completely mixed state. To reduce Eq.(3.13) into a cat state the membrane's position must be disentangled from the two cavity modes. Disentangling such states is a very difficult task and it is here that many protocols fail and become probabilistic. Achieving this disentanglement deterministically will first be studied using only the MITM setup. An ensemble of atoms will then be introduced into the system to provide a more practical disentanglement protocol.

At first glance there are two possible approaches to perform the required disentanglement of the state Eq.(3.13) using only the MITM setup. The first of these approaches involves simply allowing the N photons to decay from both cavities, potentially evolving the system into the disentangled state $|\psi\rangle \propto (|\beta_M\rangle + |-\beta_M\rangle)\,|0,0\rangle$. This approach, however, is flawed as the membrane is left in a mixed state due to the non-unitary evolution. The second approach involves conditionally flipping the state of the cavity modes, depending on the membrane's position. That is, performing the transformation,

$$|\beta_M, 0, N\rangle + |-\beta_M, N, 0\rangle \xrightarrow{\hat{P}} |\beta_M, N, 0\rangle + |-\beta_M, N, 0\rangle, \tag{3.18}$$

which could be achieved by the unitary,

$$\hat{P} = \hat{X}_+ \otimes \hat{U}_{Flip} + \hat{X}_- \otimes \hat{I}, \tag{3.19}$$

where $\hat{U}_{Flip}|\beta_M, 0, N\rangle = |\beta_M, N, 0\rangle$, and $\hat{X}_\pm = \sum_{\pm x>0} |x\rangle\langle x|$ are position projection operators. While this approach has the potential to deterministically disentangle the state, it essentially requires that the transmission rate of the membrane is also position dependent, $J(t, x)$, which is extremely experimentally challenging for pico to nano-metre displacements of the membrane.

As the two disentanglement methods discussed above either fail or are impractical an alternative disentanglement protocol must now be established. One novel method of disentangling Eq.(3.13) involves the polarisation dependent excitation of $M > N$ three level atomic systems. Here the idea is to transfer the membrane/cavity mode entanglement to entanglement between the membrane's position and the state of the atomic ensemble. Once this is achieved the entangled membrane/atomic state can be disentangled by manipulating the atomic ensemble. This entanglement transfer can be achieved if the light in the left/right cavities is left/right hand (σ_L/σ_R) circularly polarised. By quickly introducing an ensemble of M 3-level atoms into the system the photons in the left/right cavity modes are separately absorbed into the $m_s = \pm 1$ excited states of the atoms, see Fig.3.6. This process simultaneously removes the photons from both cavities while encoding the state of each cavity into the ensemble of atoms. To explore the mapping of the entanglement to the atomic ensemble the case of a single 3-level atom interacting with the σ_L/σ_R polarised photons can be considered.

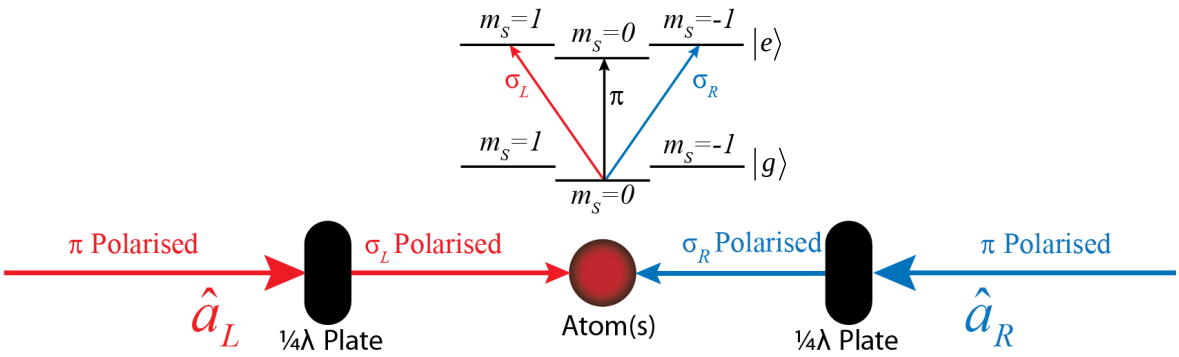

FIGURE 3.6: Depiction of the transfer of entanglement from the cavity modes to an ensemble of atoms. The left and right cavity modes are left/right hand circularly polarised then directed into a cloud of atoms. Two separate transitions are excited depending on the polarisation, shown above.

In this case the interaction is described by the Hamiltonian,

$$\hat{H}^{I}_{MLJC} = g_L \left(\hat{a}_L \hat{\sigma}^{(1)}_{+} + \hat{a}^{\dagger}_L \hat{\sigma}^{(1)}_{-} \right) + g_R \left(\hat{a}_R \hat{\sigma}^{(-1)}_{+} + \hat{a}^{\dagger}_R \hat{\sigma}^{(-1)}_{-} \right), \tag{3.20}$$

where the detuning has been set to zero and $\hat{\sigma}^{(1)}_{\pm}/\hat{\sigma}^{(-1)}_{\pm}$ are the atomic raising and lowering operators associated to the $\Delta m_s = 1/-1$ transitions with coupling strengths g_L/g_R. As discussed in Section 2.2.2 if the interaction strengths are identical this Hamiltonian can be easily extended to account for M atoms. By incorporating M atoms into the entangled state, Eq.(3.13), and evolving it under the M-atom extension of Eq.(3.20) for a specific time t_3, ensuring all photons are absorbed, the entanglement is essentially transferred from the two cavity modes to the M atoms,

$$|\psi(t_E + t_3)\rangle = \frac{1}{\sqrt{2N_E}} \sum_{i}^{N_E} \left(|\beta_M, 0, 0\rangle | - 1^i_e\rangle + | - \beta_M, 0, 0\rangle | 1^i_e\rangle \right), \tag{3.21}$$

where $N_E = M!/(N!(M-N)!)$, $| \pm 1^i\rangle$ denotes the ith permutation of the N $m_s = \pm 1$ magnetic states over the M atoms and the subscripts e, g the optical state, see Fig.3.6. This evolution requires $g_{L/R} \gg g_0, \Omega$ to avoid the effects of the changing photon pressure force on the membrane. If this condition is not met, the amplitude of the membrane's oscillation will decrease due to the decreasing number of photons in the cavity. It is also important to note here that if the cavity is initialised in an EC state, to maintain determinism, this transfer of entanglement requires that $M > |\alpha|^2$. The membrane-atom entangled state, Eq.(3.21), can now be disentangled by applying a π pulse of linearly polarised light to the atoms. As linearly polarised light is comprised of both left and right hand circularly polarised light, application of a π pulse will simultaneously send the $m_s = \pm 1$ state atoms to the ground state. The remaining $M - N$ atoms will be excited into the $m_s = 0$ optically excited state. After application of this pulse Eq.(3.21) reduces to,

$$|\psi(t_f)\rangle = \frac{1}{\sqrt{2N_E}} \sum_{i}^{N_E} \left(|\beta_M, 0, 0\rangle | 0^i_e\rangle + | - \beta_M, 0, 0\rangle | 0^i_e\rangle \right), \tag{3.22}$$

which is a pure cat state of the membrane's position. In this case $|0^i_e\rangle$ denotes the ith permutation of the $M - N$ $m_s = 0$ optically excited magnetic states over the M atoms.

3.4 Experimental Realisation

In the previous sections it was shown that, in theory, a cat state of the membrane's position can be deterministically created by controlling its transmission rate and selectively introducing M atoms into the system. The experimental realisation of such control over the membrane's opacity has, however, never been demonstrated and the well timed introduction of M atoms into the system at first glance is seemingly impossible. This section will focus on addressing each of these problems by proposing an experimental platform in which the transmission rate of the membrane and the introduction of an ensemble of atoms can be controlled.

The proposed experiment consists of a multi-cavity system where each cavity is distinguished by the polarisation of the light in the system, shown in Fig.3.7. Each of the cavities are separated through the use of appropriately positioned beam displacers and alternated between by the activation of Electro-optic quarter wave plates (EOP). For vertically polarised light, the cavity resembles that of a Fabry-Pérot cavity where the membrane is positioned in the center. The Fabry-Pérot cavity is shown in Fig.3.7 by red and blue lines, each corresponding to the left/right cavities. This means that if the light in the system is vertically polarised and the natural transmission rate of the membrane satisfies $g_0, \Omega \gg J$ the system can be described by Eq.(3.6). If the light is horizontally polarised the system corresponds to a Ring cavity containing the membrane, shown as green in Fig.3.7. In this case the effective transmission rate of the membrane drastically increases as the light can freely travel between the left/right cavities and hence the system can be described by the highly transmissive Hamiltonian, Eq.(3.8). The evolution described by Eq.(3.11), which is required to drive the displacement of the membrane, can be realised by alternating between these two cavities through the activation of the EOPs A and B in Fig.3.7. Introduction of many atoms into the system can be achieved by introducing a third cavity using a similar technique as above. At the end of the evolution, Eq.(3.11), the system remains in the high opacity regime. If at this time the EOPs C and D in Fig.3.7 are activated the system will again resemble a Ring cavity, but one which contains M atoms as well as the membrane. Provided that the atoms are each prepared in the optical ground state, $\Delta m_s = \pm 1$ transitions will be excited as the light of each mode is left/right hand polarised by two separate quarter wave plates, entangling the membrane with the atomic states.

To create a cat state with the proposed experiment a specific operational protocol must be followed. Once the system has been initialised in the state Eq.(3.12) with M ground state atoms the experiment starts with an evolution in the high opacity regime for time t_1. This evolution corresponds to driving the membrane to the maximal possible displacement in the

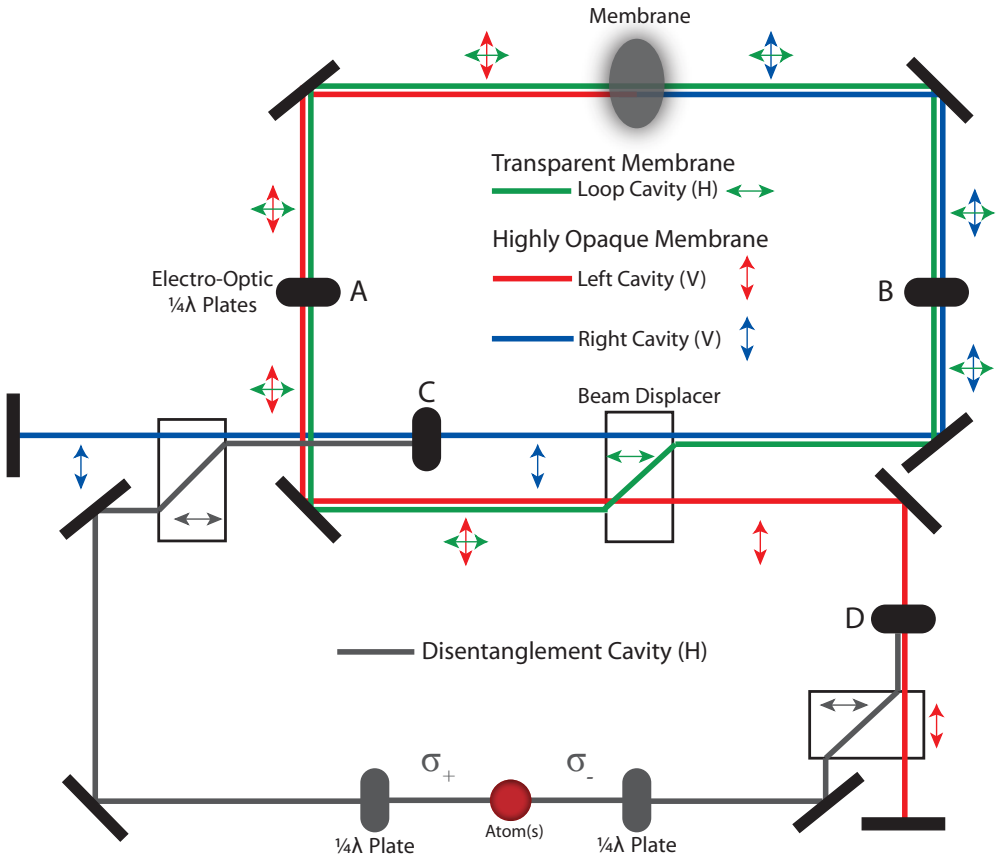

Figure 3.7: Proposed experimental configuration for effective control of the membranes opacity and the disentanglement operation. The three cavities necessary for both the preparation and disentanglement of the cat state are colour coded. The polarisation associated to each mode is also shown. The EOPs (A, B) are used to alternate the polarisation of the cavity modes to switch between the two membrane opacity regimes. EOPs (C, D) are used to introduce atoms into the system.

initial potential well. At the end of this evolution the EOPs A and B in Fig.3.7 can then be activated to switch the system into the transparent membrane regime. Evolution in this regime for time t_2 will flip the state of the cavity modes, which corresponds to displacing the harmonic potential. Deactivating these EOPs will then switch the system back into the high opacity regime but under a displaced harmonic potential, increasing the potential energy of the membrane. By evolving again in this regime for time t_1, the membrane's maximal displacement will increase in accordance with Eq.(3.7). This process can be repeated until the desired spatial displacement is acquired. Once the desired displacement is achieved the system will reside in the high opacity regime in the entangled state, Eq.(3.13). In order to create a cat state, the membrane must now be disentangled from the cavity modes. By

activating EOPs C and D in Fig.3.7, M atoms can be introduced into the system. Evolving this combined system for time t_3 will transfer the entanglement between the membrane and the cavity modes to the atoms, as shown in Eq.(3.21). Finally, by application of a linearly polarised π pulse to the atomic ensemble, a cat state of the membrane's position can be produced.

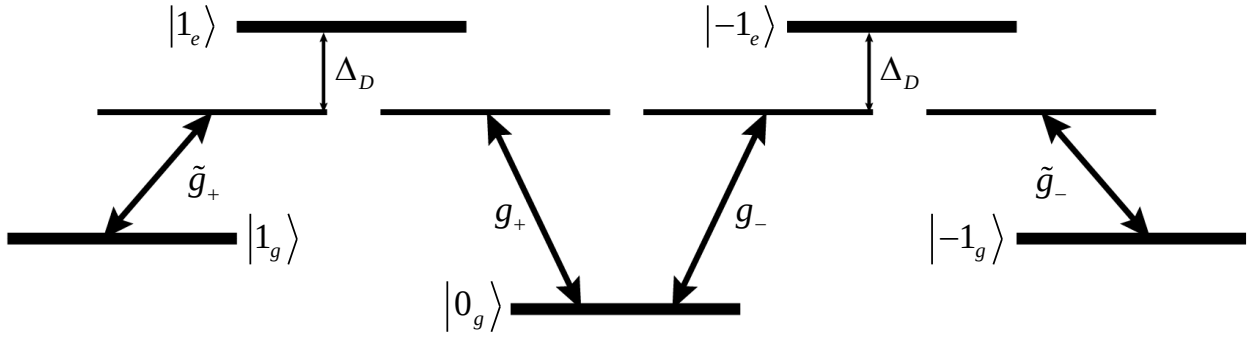

FIGURE 3.8: Depiction of the Raman transition which can be applied to the 3-level atomic system to excite the magnetic levels of the optical ground state, $|\pm 1_g\rangle$, rather than those of the optically excited state, $|\pm 1_e\rangle$. The interaction strength for each transition is denoted by the respective g.

As optical transitions are considered in the proposed experiment, application of a π pulse to the ensemble of 3-level atoms to disentangle the system is quite difficult experimentally. This difficulty stems from the short lifetimes of the optically excited states, in turn, making the disentanglement process experimentally challenging. However, the optically excited states of the 3-level atoms can be bypassed through the use of a Raman transition. The atoms can be directly excited into the $m_s = \pm 1$ levels of the optical ground state by detuning the left/right optical cavity modes from the atomic transition and introducing a similarly detuned coherent field, depicted in Fig.3.8. This is beneficial as these levels of the optical ground state are significantly longer lived, allowing for a more practical implementation of the π pulse to the atomic ensemble. Bypassing the optically excited state requires that both the left/right optical cavity modes and the classical field are off resonance with the atomic transition such that the detuning, Δ_D, satisfies $\Delta_D \gg g_\pm$, where $g_\pm$ denotes the coupling strength to the $m_s = \pm 1$ transitions, shown in Fig.3.8. An effective Hamiltonian for this process can be derived by time-averaging the dynamics of the system. For an interaction picture Hamiltonian of the form,

$$\hat{H}_I(t) = \sum_{n=1}^{N} \hat{h}_n e^{-\Delta_D t} + \hat{h}_n^\dagger e^{i\Delta_d t}, \tag{3.23}$$

the effective Hamiltonian can be expressed as [137],

$$\hat{H}_{eff} = \sum_{m,n=1}^{N} \frac{1}{\hbar\Delta_D} \left[\hat{h}_m^\dagger, \hat{h}_n\right]. \tag{3.24}$$

In the case of a single 3-level atom and a single, left hand circularly polarised optical mode, shown in the left half of Fig.3.8, the interaction picture Hamiltonian of the system before time-averaging is,

$$\hat{H}_I^R = \frac{\hbar g_+}{2}|1_e\rangle\langle 0_g|\hat{a}e^{-i\Delta_D} + \frac{\hbar\tilde{g}_+}{2}|1_e\rangle\langle 1_g|e^{-i\Delta_D t} + \frac{\hbar g_+}{2}|0_g\rangle\langle 1_e|\hat{a}^\dagger e^{i\Delta_D t} + \frac{\hbar\tilde{g}_+}{2}|1_g\rangle\langle 1_e|e^{i\Delta_D t}. \tag{3.25}$$

An identical Hamiltonian can also be written to describe a right hand circularly polarised optical mode, corresponding to the $\Delta m_s = -1$ transition, depicted in the right half of Fig.3.8. Through the use of Eq.(3.24) the effective Hamiltonian for a single atom system coupling to both left and right hand circularly polarised optical modes is $\hat{H}_R = \hat{H}_+^R + \hat{H}_-^R$ where,

$$\begin{aligned}\hat{H}_\pm^R = \frac{\hbar g_\pm^2}{4\Delta}\left(|\pm 1_e\rangle\langle\pm 1_e|\hat{a}_\pm\hat{a}_\pm^\dagger - |0\rangle\langle 0|\hat{a}_\pm^\dagger\hat{a}_\pm\right) - \frac{\hbar\tilde{g}_\pm^2}{4\Delta}\left(|\pm 1_e\rangle\langle\pm 1_e| - |\pm 1_g\rangle\langle\pm 1_g|\right)\\ + \frac{\hbar g_\pm\tilde{g}_\pm}{4\Delta}\left(|\pm 1_g\rangle\langle 0|\hat{a}_\pm + |0\rangle\langle\pm 1_g|\hat{a}_\pm^\dagger\right),\end{aligned} \tag{3.26}$$

with $\tilde{g}_\pm$ denoting the coupling rate associated with the transition between the virtual $m_s = \pm 1$ levels of the optical excited state and $m_s = \pm 1$ levels of the optical ground state, shown in Fig.3.8. By following a similar rational to that which was discussed in Section 2.2.2 this Hamiltonian can be easily extended to account for M atoms.

3.5 Numerical Simulations

Both the theory and a possible experimental realisation of the cat state creation protocol have now been established. Simulations of the proposed protocol can now be performed to determine the quality and size of the resulting cat states. In this section numerical simulations of the membrane's dynamics with the consideration of dissipative effects will first be performed to show that large displacements of the membrane can be achieved. Throughout the simulations a BEC consisting of $\sim 10^5$ Rubidium-87 atoms will be used due to its small mass and its compatibility with the MITM model [128]. The two cavity modes will then be initialised in a NOON state, Eq.(3.12), to show that, after evolution and application of the disentanglement protocol, a cat state can be created.

The dynamics of the system can be simulated by solving the full master equation,

$$\dot{\hat{\rho}} = -\frac{i}{\hbar}\left[\hat{H}(t), \hat{\rho}\right] + \kappa_c \sum_i^{L,R} \left(\hat{a}_i \hat{\rho} \hat{a}_i^\dagger - \frac{1}{2}\{\hat{a}_i^\dagger \hat{a}_i, \hat{\rho}\}\right) + \gamma_M \left(\hat{b}\hat{\rho}\hat{b}^\dagger - \frac{1}{2}\{\hat{b}^\dagger \hat{b}, \hat{\rho}\}\right), \tag{3.27}$$

where the time dependence in the Hamiltonian describes the alternation between the two different opacity regimes, Eq.(3.6) and Eq.(3.8). Here the parameters κ_c and γ_M denote the cavity and mechanical damping rates respectively. Before continuing, it will be assumed that the mechanical damping rate, γ_M, is negligible with respect to the optical damping rate during the time scales that will be considered, $\gamma_M \ll \kappa_c$ [129]. By solving Eq.(3.27) with the initial condition $|\psi(0)\rangle = |0_M, N, 0\rangle$ the driving of the membrane's displacement can be demonstrated, see Fig.3.9. To examine the dependence of the photon number difference, Δ, on the maximal displacement, simulations were performed using several experimentally achievable values of N. A linear increase in the maximal displacement with N, predicted by Eq.(3.7), can be clearly observed in Fig.3.9 where the mechanical frequency was set to $\Omega = 2\pi \times 15.2$ kHz, the mechanical coupling rate to $g_0 = 2\pi \times 0.5$ MHz, the cavity damping rate to $\kappa_c = 2\pi \times 2.6$ kHz [129], with a BEC of mass $m = 17.3$ ag [128]. The results also

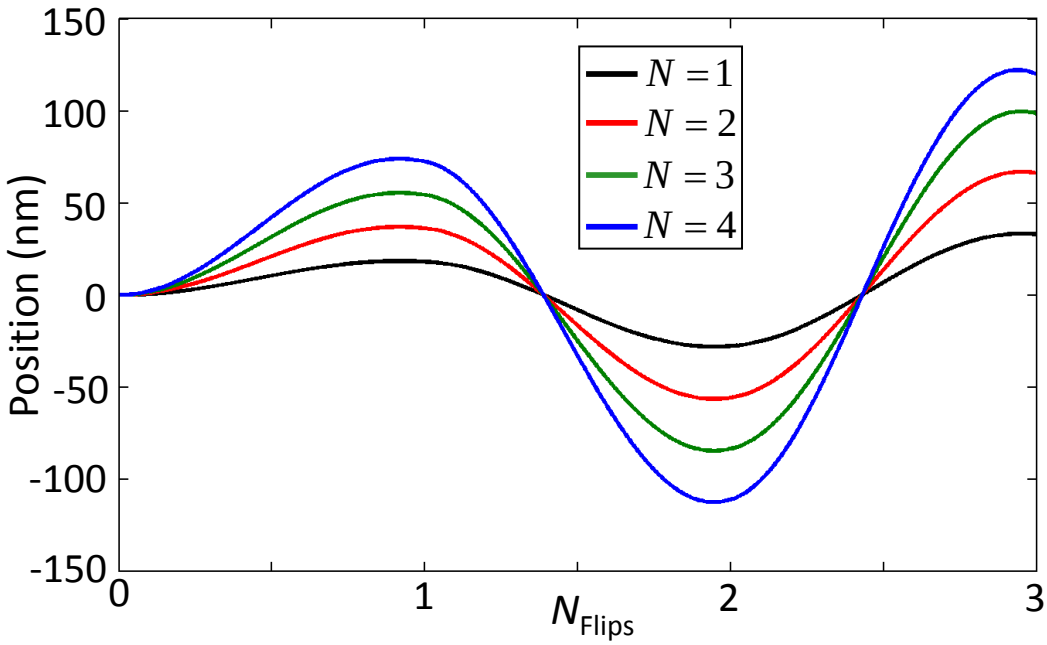

FIGURE 3.9: The dynamics of a BEC's position when the system is initialised in the state $|\psi(0)\rangle = |0_M, N, 0\rangle$. Several values of the photon number, N, were used and dissipative effects were considered. The simulations were performed in units of Ω with $g_0 = 32.8\Omega$, $\kappa_c = 0.17\Omega$ and $N_{Flips} = t/\tau_{Flip} = t\frac{\Omega}{\pi}$.

show that nanometre displacements of the BEC's center of mass position from the origin can be attained with only three flips of the two cavity states. While the results show that under these conditions initialising the cavity modes in small number states is somewhat effective for displacing the BEC, many more flips are required to achieve large spatial displacements of bigger membranes. Under these conditions performing more than five flips is not possible if the cavities are initialised in small number states as, in this case, the cavity damping rate is on the order of the mechanical frequency ($\kappa_c \sim \Omega$). This means that by the time the BEC reaches its maximal displacement a significant portion of the photons are lost from the cavity. The loss of photons from the cavity also produces a short time delay between the point in which the membrane achieves its maximal displacement and the application of the flip. This is most easily explained in the displaced harmonic oscillator picture, Fig.3.3. As the system evolves photons are lost from the cavities causing the center of the two potential wells to shift towards the origin. This results in the achievement of maximal displacements at times slightly shorter than those predicted in Eq.(3.7). The times predicted by Eq.(3.7) were used in these simulations to demonstrate this effect as realistically these short time delays must be accounted for.

In order to create a cat state of the membrane's position the cavity must be initialised in a NOON state, Eq.(3.12). In what follows the cavity will be initialised in a NOON state with $N = 2$. Of course, evolving this initial state results in $\langle \hat{x} \rangle = 0$, as the membrane is simultaneously displaced in both the $+x$ and $-x$ directions. Two approaches will be made to observe the cat state produced. The first involves the calculation the Wigner function to observe the 'quantumness' of the final state while the second involves calculating the fidelity between the cat state produced and a corresponding ideal cat state. Beforehand, however, a simplification can be made to the disentanglement process to increase the efficiency of the simulations. As the time scales of the disentanglement procedure are required to be significantly shorter than that of the standard evolution which drives the membrane's displacement, $g_{L/R} \ll \Omega$, losses during this procedure will be neglected. This also means that the disentanglement protocol can effectively be performed by application of the disentanglement unitary described in Eq.(3.19). Simulations of the disentanglement protocol are essentially those which were performed in Section 2.2.4 where instead only two modes of light must be considered. A cat state of the membrane's position can then be produced by application of the disentanglement unitary after the entire evolution has been made,

$$\hat{P}|\psi(t_E)\rangle \propto (|\beta_M\rangle + |\beta_M\rangle)\,|0,0\rangle|0_g\rangle^{\otimes M}, \tag{3.28}$$

where $|0_g\rangle^{\otimes M}$ describes the state in which all M atoms are in the optical ground state. The

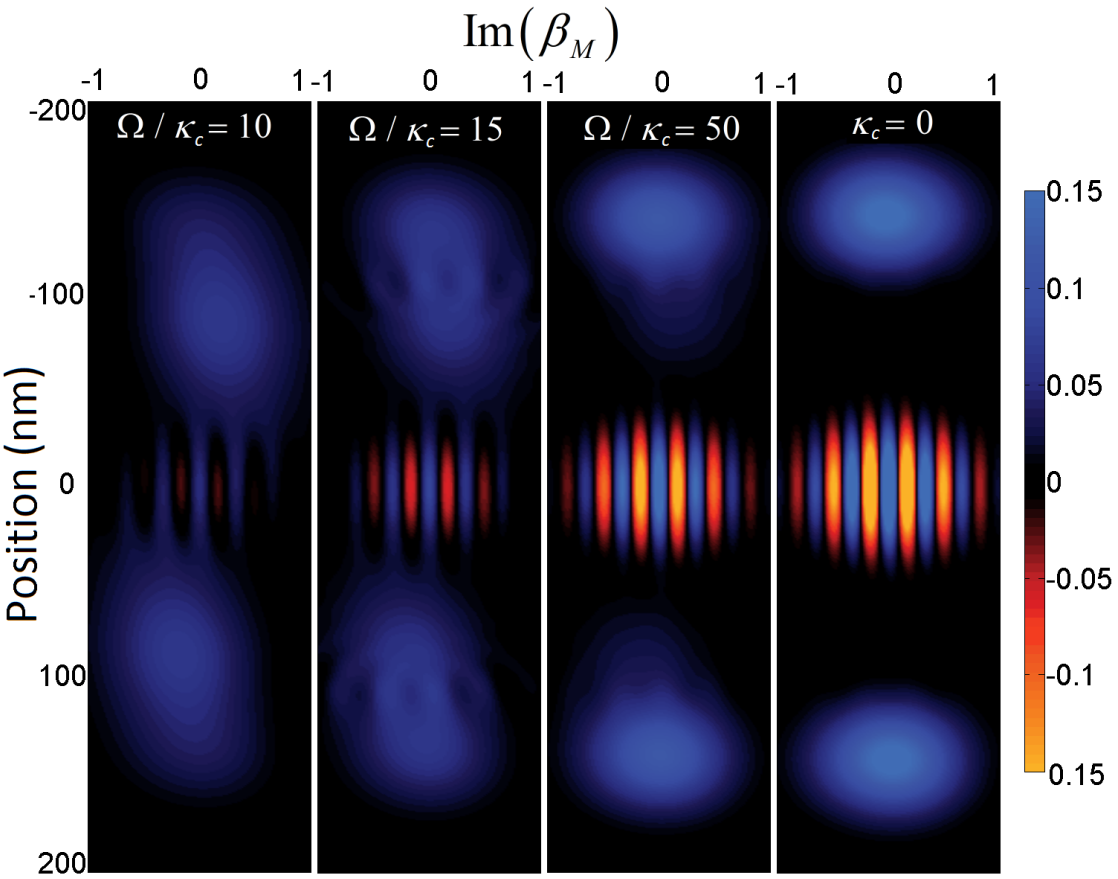

FIGURE 3.10: Density plots of the Wigner function for different cavity damping rates, κ_c. These simulations were performed using the parameters for a BEC shown above with $N = 2$ photons in the system and $N_{Flips} = 3$. The negativity of the Wigner function shows that the final state is still a quantum state [138].

resulting Wigner function of the membrane's state after application of $\hat{P}$ is presented in Fig.3.10 for several cavity damping rates. These results show that the final state strongly resembles that of a typical cat state with decoherent effects similar to those observed by Haroche, presented in Fig.3.1a. They also show that, if the ratio between the trap frequency of the BEC and the cavity loss rate can be increased by a factor of ∼10, spatial separations of up to 300 nm can be achieved between the two center of mass positions of the 10^5 atom containing BEC. This is more than double the displacement achieved in the entangled state analogue where only a single ion was used [19]. To determine the degree of resemblance between the final state, $|\psi(t_f)\rangle$, and a typical cat state $|\psi_{Cat}(t)\rangle \propto |\beta_M(t)\rangle + |-\beta_M(t)\rangle$, the fidelity can be calculated,

$$F(t) = |\langle\psi_{Cat}(t)|\psi_f\rangle|^2 . \tag{3.29}$$

The coherent amplitude, $\beta_M(t)$, corresponds to the membrane's state when evolving $|\psi(0)\rangle =$

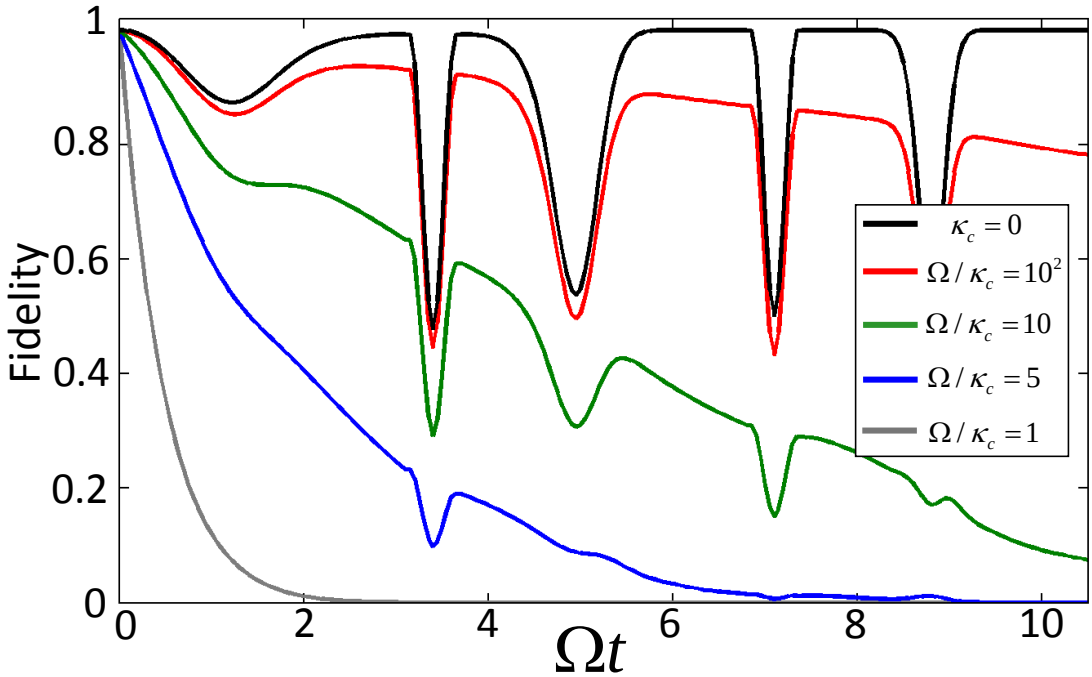

Figure 3.11: The fidelity between the evolved state at each time step with a corresponding ideal cat state using several cavity dampening rates, κ_c, and $N = 2$. The sharp peaks correspond to evolution in the transparent membrane regime whereas the thicker peaks correspond to an artefact of disentanglement projector, as the projector is only conditional on position and not momentum. The fidelity is unity initially as $F(t{=}0) = |\langle\psi_{Cat}(\beta = 0)|\psi_0\rangle|^2 = |\langle\psi_0|\psi_0\rangle|^2$.

$|0_M, N, 0\rangle$ under identical conditions, shown in Fig.C.1 of Appendix C. The results show (Fig.3.11) that with $\Omega \approx \kappa_c$ the cat state is destroyed before the first flip is performed. Using literature values, $\Omega/\kappa_c \approx 5$, the state partially survives the first cavity state flip [129]. For ideal results, $F > 80\%$, the ratio between the mechanical trap frequency of the BEC and the cavity loss rate must be increased by a factor of 20 where the cat state survives all three cavity state flips.

3.6 Conclusion

In this chapter a hybrid quantum system designed for the deterministic creation of macroscopic quantum states was proposed. The system consisted from a BEC type membrane that was placed inside a Fabry-Pérot type cavity. It was shown that by controlling the opacity of the BEC its displacement from the origin could be driven at a rate proportional to the number of photons in the system. This result was then used to produce and essentially grow the spatial extent of a cat state of the BEC's position. This required the initialisation of the two cavities in a NOON like state, which was shown generates entanglement between the membrane's position and the cavity modes after the system is evolved. To reduce this entangled state to a cat state a deterministic disentanglement procedure was proposed which involved the transfer of the entanglement to an ensemble of atoms. A possible experimental platform was then proposed which was capable of both controlling the membrane's opacity and applying the deterministic disentanglement procedure. Finally, several simulations were performed showing that large spatial displacements of the BEC could be achieved using only a small number of photons in the system. Simulations of cat state creation were also performed which showed that relatively high fidelity cat states could be produced if either slightly larger mechanical frequencies or slight smaller cavity loss rates than those achieved in previous experiments could be reached. Overall the proposed cat state creation protocol provided an experimentally feasible method of deterministically creating cat states significantly larger than the majority of previous proposals. Creation of such states are essential to further the understanding of quantum decoherence and have many potential applications in a wide range of quantum technologies.

Chapter 4

Conclusions and Outlook

With the growth of quantum science, more and more potential applications of quantum mechanical effects are being established. As many of these applications show promise in improving current technologies, significant effort is focused on the implementation of such effects to develop the technologies of the future. However, to develop such technology, quantum systems must be constructed which have the ability to generate and manipulate quantum mechanical states, store and transport quantum information over long distances and maintain quantum coherence for large system sizes at practical temperatures. This requires not only a thorough understanding of the mechanisms behind the destruction of quantum coherence, but for the engineering of versatile quantum systems. Hybrid quantum systems show potential in meeting these requirements as such systems can be designed to inherit many advantages from their comprising subsystems. In this thesis two separate hybrid quantum systems were studied where experimental platforms were proposed to either construct practical quantum technologies or create macroscopic quantum states for the study of decoherence.

4.1 cQED with WGM Resonators

One of the most successful approaches to the development of practical quantum systems involves the study of light-matter interactions (cQED). Here light-matter interactions can be used to effectively couple distant quantum systems allowing for the creation of quantum states and the transport of quantum information. However, this requires the strength of the light-matter interactions to be much larger than any dissipative effects present in the system which has proven to be very experimentally challenging. In Chapter 2 of this thesis an alternative approach to achieving strong light-matter interactions was proposed. By

considering the interaction between a single spin and an ensemble of degenerate optical modes, rather then a single mode and an ensemble of spins, it was shown that optical coupling strengths several orders of magnitude larger then previous experiments could be achieved. It was then shown that fused silica spherical resonators provide a relatively scalable experimental platform for the realisation of such strong coupling allowing for high fidelity transfer of a single excitation between spins separated by almost 100 μm. A method of further increasing this coupling was also discussed which required the use of a diamond spherical resonator. To increase the coupling strength even further there are many pathways which can now be taken. These pathways involve finding methods to reduce the mode volume, increase the maximal number of modes the resonator can support, decrease the scattering of light from the spins and minimise the non-transversal components of the TM WGM electric field. The WGM-spin model can also be extended to study the dynamics of a single excitation in one and two dimensional cQED arrays. Such extensions could then be applied in quantum simulations, computation and teleportation.

4.2 Creation of Macroscopic Quantum States

Quantum mechanical effects have yet to be observed on systems outside of the nanoscopic realm. As there is currently no fundamental postulate which limits quantum mechanical effects to such scales, the main limitations are thought to stem from experimentation. One of the more popular approaches which is made to study how quantum mechanical systems become classical involves the creation of quantum states of macroscopic objects. However, many of current protocols for the creation of such states are probabilistic, as they rely on measurements. In Chapter 3 of this thesis a novel method of deterministically creating macroscopic quantum states was proposed. It was shown that by controlling the opacity of a macroscopic membrane, quantum superpositions of its position could be created. By considering a BEC type membrane, states which corresponded to the BEC being located at two spatial positions simultaneously were deterministically created, where the separation between the two positions was as large as 300 nm. Our cat state creation protocol required the initialisation of the two cavity modes in a NOON state, which limited the maximal spatial separation as only a small number of photons could be considered. Further work could focus on developing alternative initial conditions and approaches which could be used to achieve much larger spatial separations. Our protocol also required a method of deterministically disentangling the state of the system. While a possible disentanglement protocol was proposed, future work could focus on an alternative means of disentanglement. Alternative

types of membrane's could also be considered to suggest different systems which can be used to study the transformation between the quantum and classical realms.

Appendix A

Solving the Multi-Mode Tavis-Cummings Model

A.1 The Single Excitation Basis

Simulating the dynamics of an N-mode M-spin Jaynes-Cummings system with the inclusion of dissipative effects can be extremely computationally demanding. In this section an alternative approach to the evolution of such a system will be considered and proved equivalent to the standard master equation approach. The Hamiltonian which describes the N-mode M-spin Jaynes-Cummings model can be expressed as,

$$\hat{H}_{MMTC} = \hbar \sum_{i=1}^{N} \omega_i \hat{a}_i^\dagger \hat{a}_i + \frac{1}{2}\hbar \sum_{i=1}^{M} \Omega_i \hat{\sigma}_z^i + \hbar g \sum_{j=i}^{M} \sum_{i=1}^{N} \left(\hat{\sigma}_+^j \hat{a}_i + \hat{\sigma}_-^j \hat{a}_i^\dagger \right). \tag{A.1}$$

Typically, evolution of this system with the inclusion of dissipative effects requires solving the full master equation,

$$\dot{\hat{\rho}} = -\frac{i}{\hbar}\left[\hat{H}_{MMTC}, \hat{\rho}\right] + \sum_{k=1}^{M} \gamma_k \left[\hat{\sigma}_-^k \hat{\rho} \hat{\sigma}_+^k - \tfrac{1}{2}\left[\hat{\sigma}_+^k \hat{\sigma}_-^k, \hat{\rho}\right\}\right] + \sum_{i=1}^{N} \kappa_i \left[\hat{a}_i \hat{\rho} \hat{a}_i^\dagger + \tfrac{1}{2}\left\{\hat{a}_i^\dagger \hat{a}_i, \hat{\rho}\right\}\right], \tag{A.2}$$

where γ_k denotes the spontaneous emission rate of the kth spin and κ_i the damping rate of the ith mode. An alternative approach to the evolution of this system involves solving the Schrödinger equation with the non-Hermitian Hamiltonian,

$$\hat{H}_C = \hbar \sum_{j=1}^{N} \left(\omega_j - \frac{i}{2}\kappa_j\right) \hat{a}_j^\dagger \hat{a}_j + \frac{\hbar}{2} \sum_{j=1}^{M} \left(\Omega_j \hat{\sigma}_z^j - i\gamma_j \hat{\sigma}_{ee}^j\right) + \hbar g \sum_{j=1}^{M} \sum_{k=1}^{N} \left(\hat{\sigma}_+^j \hat{a}_k + \hat{\sigma}_-^j \hat{a}_k^\dagger\right). \tag{A.3}$$

However, as a consequence of this non-Hermiticity, probability is not conserved under such an evolution. To prove that the dynamics obtained using this alternative approach are equivalent to that achieved by solving Eq.(A.2) the model must be restricted to the single excitation basis,

$$|0\rangle|e_k\rangle \equiv |0_1, ..., 0_N\rangle|g_1, g_2, ..., g_{k-1}, e_k, g_{k+1}, ..., g_M\rangle, \tag{A.4}$$

$$|1_k\rangle|g\rangle \equiv |0_1, 0_2, ..., 0_{k-1}, 1_k, 0_{k+1}, ..., 0_N\rangle|g_1, ..., g_M\rangle, \tag{A.5}$$

$$|0\rangle|g\rangle \equiv |0_1, ..., 0_N\rangle|g_1, ..., g_M\rangle. \tag{A.6}$$

In this basis the excitation can be kept track of as here it is possible to assume that any loss of probability is associated with the system evolving into the ground state $|0\rangle|g\rangle$. To begin the proof of equivalence the basis states will be relabelled as,

$$|k\rangle \equiv |1_k\rangle|g\rangle, \tag{A.7}$$

$$|N+k\rangle \equiv |0\rangle|e_k\rangle, \tag{A.8}$$

$$|0\rangle \equiv |0\rangle|g\rangle. \tag{A.9}$$

Now, in terms of the conditional Hamiltonian, the master equation becomes,

$$\dot{\hat{\rho}} = -i\left[\hat{H}_C\hat{\rho} - \hat{\rho}\hat{H}_C^\dagger\right] + \sum_{j=1}^{N}\kappa_j\hat{a}_j\hat{\rho}\hat{a}_j^\dagger + \sum_{j=1}^{M}\gamma_j\hat{\sigma}_-^j\hat{\rho}\hat{\sigma}_+^j = \hat{\mathcal{L}}_C\hat{\rho} + \hat{\mathcal{J}}\hat{\rho}, \tag{A.10}$$

where the superoperators $\hat{\mathcal{L}}_C$ and $\hat{\mathcal{J}}$ are given by,

$$\hat{\mathcal{L}}_C\hat{\rho} = -i\left[\hat{H}_C\hat{\rho} - \hat{\rho}\hat{H}_C^\dagger\right] \quad \text{and} \quad \hat{\mathcal{J}}\hat{\rho} = \sum_{j=1}^{N}\hat{\mathcal{J}}_j\hat{\rho}, \tag{A.11}$$

with,

$$\hat{\mathcal{J}}_j\hat{\rho} = \kappa_j\hat{a}_j\hat{\rho}\hat{a}_j^\dagger \quad \text{and} \quad \hat{\mathcal{J}}_{N+j}\hat{\rho} = \gamma_j\hat{\sigma}_-^j\hat{\rho}\hat{\sigma}_+^j. \tag{A.12}$$

For an arbitrary initial state containing only a single excitation, the density operator is,

$$\hat{\rho}(0) = \sum_{j_1,j_2=1}^{N+M}\rho_{j_1j_2}|j_1\rangle\langle j_2|. \tag{A.13}$$

The action of $\hat{\mathcal{L}}_C$ on the initial state, $\hat{\rho}(0)$, will evolve it into the state,

$$\hat{\rho}(t) = e^{\hat{\mathcal{L}}_C t}\hat{\rho}(0) = \sum_{j_1,j_2=1}^{N+M} \rho_{j_1 j_2}(t)|j_1\rangle\langle j_2|, \tag{A.14}$$

while $e^{\hat{\mathcal{L}}_C t}|0\rangle\langle 0| = |0\rangle\langle 0|$. Also, the action of $\hat{\mathcal{J}}$ on the density operator is,

$$\hat{\mathcal{J}}\hat{\rho} = \left(\sum_{j=1}^{N+M} \rho_{jj}\Gamma_j\right)|0\rangle\langle 0|, \tag{A.15}$$

where,

$$\Gamma_j = \begin{cases} \kappa_j & \text{for } j \leq N, \\ \gamma_j & \text{for } N < j \leq N+M, \end{cases} \tag{A.16}$$

and $\hat{\mathcal{J}}|0\rangle\langle 0| = 0$. By considering the properties of the superoperators, $e^{\hat{\mathcal{L}}_C t}|0\rangle\langle 0| = |0\rangle\langle 0|$ and $\hat{\mathcal{J}}|0\rangle\langle 0| = 0$, it is clear that the formal solution to the master equation,

$$\hat{\rho}(t) = e^{\hat{\mathcal{L}}_C t}\hat{\rho}(0) + \int_0^t dt_1 e^{\hat{\mathcal{L}}_C (t-t_1)}\hat{\mathcal{J}} e^{\hat{\mathcal{L}}_C t_1}\hat{\rho}(0) + \int_0^t dt_2 \int_0^{t_2} dt_1 e^{\hat{\mathcal{L}}_C (t-t_1)}\hat{\mathcal{J}} e^{\hat{\mathcal{L}}_C (t_2-t_1)}\hat{\mathcal{J}} e^{\hat{\mathcal{L}}_C t_1}\hat{\rho}(0) + ... \tag{A.17}$$

terminates after the second term. This reduces the formal solution to,

$$\hat{\rho}(t) = e^{\hat{\mathcal{L}}_C t}\hat{\rho}(0) + \int_0^t dt_1 e^{\hat{\mathcal{L}}_C (t-t_1)}\hat{\mathcal{J}} e^{\hat{\mathcal{L}}_C t_1}\hat{\rho}(0), \tag{A.18}$$

which, after substitution of Eqs.(A.14, A.15), can be expressed as,

$$\hat{\rho}(t) = e^{\hat{\mathcal{L}}_C t}\hat{\rho}(0) + |0\rangle\langle 0| \int_0^t \sum_{j=1}^{N+M} \Gamma_j \langle j| e^{\hat{\mathcal{L}}_C t_1}\hat{\rho}(0)|j\rangle. \tag{A.19}$$

Finally, by taking the trace of the above equation and direct substitution into Eq.(A.19) it can be shown that,

$$\hat{\rho}(t) = e^{\hat{\mathcal{L}}_C t}\hat{\rho}(0) + |0\rangle\langle 0| \left(1 - \mathrm{Tr}\left[e^{\hat{\mathcal{L}}_C t}\hat{\rho}(0)\right]\right), \tag{A.20}$$

and hence $\langle j_1|\hat{\rho}(t)|j_2\rangle = \langle j_1|\hat{\rho}_c(t)|j_2\rangle$ for $j_1, j_2 \neq 0$. This proof was originally performed in collaboration with Dr James Cresser for the Tavis-Cummings model. It was then independently extended to account for N modes.

A.2 Evolution of Multi-Mode TC Model

In this section the multi-mode Tavis-Cummings Hamiltonian, Eq.(A.3), will be expressed in the interaction picture and the Schrödinger equation will be solved. To attain a time independent interaction picture Hamiltonian, Eq.(A.3) must be expressed in terms of two commuting components, $\hat{H}_C = \hat{H}_C^0 + \hat{H}_C^1$. One convenient arrangement is,

$$\hat{H}_C^0 = \hbar\bar{\omega}\left(\sum_{j=1}^{N}\frac{\omega_j}{\bar{\omega}}\hat{a}_j^\dagger\hat{a}_j + \sum_{j=1}^{M}\sum_{j=1}^{M}\hat{\sigma}_{ee}^j\right) + \hbar\sum_{j=1}^{M}\left(\frac{\Omega_j}{2} - i\frac{\gamma_j}{2} - \bar{\omega}\right)\left(\hat{\sigma}_{ee}^j + \hat{\sigma}_{gg}^j\right) \tag{A.21}$$

$$\hat{H}_C^1 = -\hbar\sum_{j=1}^{M}\left(\Omega_j - i\frac{\gamma_j}{2} - \bar{\omega}\right)\hat{\sigma}_{gg}^j - i\frac{\hbar}{2}\sum_{j=1}^{N}\kappa_j\hat{a}_j^\dagger\hat{a}_j + \hbar g\sum_{j=1}^{M}\sum_{k=1}^{N}\left(\hat{\sigma}_+^j\hat{a}_k + \hat{\sigma}_-^j\hat{a}_k^\dagger\right), \tag{A.22}$$

where $\bar{\omega}$ is the average of all the mode frequencies. As $\left[\hat{H}_C^0, \hat{H}_C^I\right] = 0$, the interaction picture Hamiltonian is then,

$$\hat{H}_C^I = e^{i\hat{H}_C^0 t/\hbar}\hat{H}_C^1 e^{-i\hat{H}_C^0 t/\hbar} = \hat{H}_C^1. \tag{A.23}$$

In the previous section it was shown that the system can be evolved by solving the Schrödinger equation. This requires a general state which describes only a single excitation in the system. Such a state can be written as,

$$|\psi(t)\rangle = \sum_{k=1}^{N}\alpha_k(t)|0\rangle|e_k\rangle + \sum_{k=1}^{N}C_k(t)|1_k\rangle|g\rangle. \tag{A.24}$$

Substitution of Eqs.(A.22, A.24) into the Schrödinger equation yields,

$$i\hbar\sum_{k=1}^{M}\dot{\alpha}_k(t)|0\rangle|e_k\rangle + i\hbar\sum_{k=1}^{N}\dot{C}_k(t)|1_k\rangle|g\rangle = \hat{H}_C^I|\psi(t)\rangle. \tag{A.25}$$

Calculation of the right hand side of Eq.(A.25) is a little cumbersome and hence will be split into two parts. The first corresponds to the expansion of the first two terms in Eq.(A.22),

$$\begin{aligned}
&\left[-\hbar\sum_{j=1}^{M}\left(\Omega_j - i\frac{\gamma_j}{2} - \bar{\omega}\right)|g\rangle_{jj}\langle g| - i\frac{\hbar}{2}\sum_{j=1}^{N}\kappa_j\hat{a}_j^\dagger\hat{a}_j\right]|\psi(t)\rangle = \\
&-\hbar\sum_{j=1}^{M}\left(\Omega_j - i\frac{\gamma_j}{2} - \bar{\omega}\right)\sum_{k=1}^{M}\alpha_k(t)|0\rangle|e_k\rangle + \hbar\sum_{k=1}^{M}\left(\Omega_k - i\frac{\gamma_k}{2} - \bar{\omega}\right)\alpha_k(t)|0\rangle|e_k\rangle \\
&-\hbar\sum_{k=1}^{M}\left(\Omega_k - i\frac{\gamma_k}{2} - \bar{\omega}\right)\left(\sum_{j=1}^{N}C_j(t)|1_j\rangle|g\rangle\right) - i\frac{\hbar}{2}\sum_{k=1}^{N}C_k(t)|1_k\rangle|g\rangle,
\end{aligned} \tag{A.26}$$

while the second corresponds to the expansion of the final term in Eq.(A.22),

$$\left[\hbar g \sum_{j=1}^{M}\sum_{k=1}^{N}\left(\hat{\sigma}_{+}^{j}\hat{a}_k + \hat{\sigma}_{-}^{j}\hat{a}_k^{\dagger}\right)\right]|\psi(t)\rangle = \hbar g \sum_{j=1}^{M}\alpha_j(t)\sum_{k=1}^{N}|1_k\rangle|g\rangle + \hbar g \sum_{j=1}^{N}C_j(t)\sum_{k=1}^{M}|0\rangle|e_k\rangle. \tag{A.27}$$

Combining Eqs.(A.26, A.27) and equating both sides of Eq.(A.25) produces a set of coupled first order differential equations,

$$i\dot{\alpha}_k(t) = -\sum_{j=1}^{M}\left(\Omega_j - i\frac{\gamma_j}{2} - \bar{\omega}\right)\alpha_k(t) + \left(\Omega_k - i\frac{\gamma_k}{2} - \bar{\omega}\right)\alpha_k(t) + g\sum_{j=1}^{N}C_j(t), \tag{A.28}$$

$$i\dot{C}_k(t) = -\sum_{j=1}^{M}\left(\Omega_j - i\frac{\gamma_j}{2} - \bar{\omega}\right)C_k(t) - i\frac{\kappa_k}{2}C_k(t) + g\sum_{j=1}^{M}\alpha_j(t), \tag{A.29}$$

which can be efficiently solved numerically with large values of N and M.

A.3 Simulations

The simulations performed throughout Chapter 2 were done so by solving Eqs.(A.28, A.29) using MATLAB. In this section the MATLAB code used will be presented. The code is structured in the following manner: all relevant parameters are first defined, arrays and integration settings are prepared, the integration is performed by calling the function *systemofode* which stores Eqs.(A.28, A.29) and finally the results are sorted and stored for plotting.

To ensure consistency between the relevant parameters in the MATLAB notebook and those in the *systemofode* function these parameters are set as global variables.

```
global Nm Na g deltas freqsum kappas gammas
```

Next, all relevant physical constants and system parameters are introduced. Here the number of modes is labelled *Nm* and the number of spins *Na*. If two antipodal clusters containing in total *Na* spins are considered then each cluster contains $M = Na/2$ spins.

```
% Input physical constants
c = 2.99*10^8;

% Setup realistic system parameters (calculated using WGM code)
greal =1.57*10^9;                % Coupling Strength
kappareal = 982354;              % Cavity Damping Rate
```

```
wareal = 2*pi*c/(637*10^-9);    % Spin Resonance Frequency
wcreal = wareal;                % Cavity Resonance Frequency
gammareal = 4*pi*10^7;          % Spontaneous Emission Rate
scale = greal;                  % Scaling Parameter

% Setting up the model parameters and scale
Nm=58; Na = 10; g=greal/scale; kappa=kappareal/scale; wa=wareal/scale;
gamma=gammareal/scale; wc = wcreal/scale; M = Na/2;
```

For the consideration of distinguishable spins/modes several arrays are then constructed to produce Gaussian distributed resonance frequencies and damping rates.

```
% Standard deviation for Gaussian distributions
sigmaA=0;   % Standard deviation for spin frequencies
sigmaM=0;   % Standard deviation for mode frequencies
sigmaDA=0;  % Standard deviation for spin damping coefficients
sigmaDM=0;  % Standard deviation for mode damping coefficients

% Construct frequency and dissipation arrays
atomfreqs=ones(Na,1)*wa;
modefreqs=ones(Nm,1)*wc;
gammas=ones(Na,1)*gamma;
kappas=ones(Nm,1)*kappa;
atomfreqs=atomfreqs+sigmaA*randn([size(atomfreqs),1]);
modefreqs=modefreqs+sigmaM*randn([size(modefreqs),1]);
gammas=gammas+sigmaDA*randn([size(atomfreqs),1]);
kappas=kappas+sigmaDM*randn([size(modefreqs),1]);
```

To more efficiently solve Eqs.(A.28, A.29) the average of the cavity resonance frequencies as well as the rate summations are pre-calculated.

```
% Calculate average frequency \bar{omega}
Mfreqavg = mean(modefreqs);

% Setup array containing wa -igamma -omegabar for each gamma/wa
deltas = atomfreqs - Mfreqavg-1i*gammas./2;
delta = atomfreqs - Mfreqavg;
freqsum=sum(delta(1:end));
```

Next, different sets of initial conditions are generated which are selected based on the desired simulation.

```
% Generate inital conditions
inits=zeros(1,Nm+Na);   % Base array
initC = inits;
initA = inits;
% Initialise excitation in the cavity when there is 1 mode and N spins.
initC(Na+1) = 1;
% Initialise excitation in the spin when there is 1 spin and N modes.
% Also used when two antipodal spins are considered.
initA(1)=1;
% Initialise excitation within one of the antipodal clusters of M spins.
Asup = inits;
for i = 1:M
    Asup(i)=1/sqrt(M);
end
```

The final preparations which are made regard the integration. To do so, the desired initial condition is selected and the integration properties are defined.

```
% Selecting initial conditions and integration accuracy.
init=Asup;
acccc=1e-5;
options = odeset('RelTol',acccc,'AbsTol',acccc);

% Setting up integration between single time steps
dt=0.005;                       % Integration time step.
tf=5;ti=0;                      % Initial and final times of the simulation.
Nsteps = tf/dt;                 % Number of Integration iterations
ysave =zeros(Nsteps,Nm+Na);     % Array to store integral results
ysave(1,:)=init;                % Setting the initial condition
time = zeros(Nsteps,1);         % Array to store time
grnd = zeros(Nsteps,1);         % Array to store grnd state prob. amp.
```

With all required preparations made, Eqs.(A.28, A.29) are then solved using MATLAB's *ode*113 equation solver. The integration is broken into *Nsteps* steps in order to calculate the probability associated to evolution of the system into the ground state.

```
% Integration loop, integrates between t and t+dt each time
for steps=1:Nsteps

    time(steps+1,1)=dt*steps;

% Integrate the ode's between one time step
    [t,y]=ode113('systemofode',[time(steps,1) time(steps+1,1)],init,options);

% Set the initial condition for the next integral
    init=y(end,:);

% Store the result of each integral
    ysave(steps+1,:) = y(end,:);

% Store probability lost -> Prob. Amp. of Ground state |0,g>
    grnd(steps+1) = sqrt(1 - (sum(abs(y(end,:)).^2)));

end
```

Finally, the results of the integration are sorted and stored before plotting.

```
atoms = 0;
prest = 0;

% Save probability the excitation resides in the spins.
for k=1:Nsteps+1,
    atoms(k)=sum((abs(ysave(k,1:Na)).^2));
end
% Save probability the excitation resides in 1st cluster of the spins.
for k=1:Nsteps+1,
    atomC1(k)=sum(abs(ysave(k,1:M)).^2);
end
% Save probability the excitation resides in 2nd cluster of the spins.
for k=1:Nsteps+1,
    atomC2(k)=sum(abs(ysave(k,M+1:Na)).^2);
end
% Save probability the excitation resides in the modes.
```

```
for k=1:Nsteps+1,
    prest(k)=sum((abs(ysave(k,Na+1:end)).^2));
end

% Convert the integration time into nanoseconds.
f = sqrt(Nm*Na)*greal/pi/2;
Tr = 1/f;
ft = 2*sqrt(Nm*Na)/2;
Tt = (2*pi)/ft;
conv = Tr/Tt;
timeNS = conv*time*10^9;        % Time in nanoseconds.
```

The code defining the *systemofode* function which stores Eqs.(A.28, A.29) is given below.

```
function dy = systemofode(t,y)
global Nm Na g freqsum deltas kappas

dy = zeros(Nm+Na,1);
dy(1:Na) = -1i.*(deltas(1:Na)).*y(1:Na)+...
1i.*freqsum.*y(1:Na)-1i.*g.*sum(y(Na+1:end));
dy(Na+1:end) = 1i.*freqsum.*y(Na+1:end)-...
kappas(1:Nm).*y(Na+1:end)./2 -1i.*g.*sum(y(1:Na));

end
```

This function can be easily extended to consider inhomogeneous coupling rates, g_i.

Appendix B

More on Whispering Gallery Modes

B.1 Alternative Form of WGM Fields

In spherical co-ordinates the solutions to the vectorial Helmholtz equation can be expressed in terms of Vector Spherical Harmonics (VSH). The TM and TE solutions, in terms of VSHs, are,

$$\mathbf{E}^{TM}_{qlm}(r,\theta,\phi) = \frac{1}{kn(r)}\left[\frac{\partial}{\partial r}R_{ql}(r)\mathbf{Y}_{lm}(\theta) + \frac{1}{r}R_{ql}(r)\mathbf{Z}_{lm}(\theta)\right], \tag{B.1}$$

$$\mathbf{E}^{TE}_{qlm}(r,\theta,\phi) = R_{ql}(r)\mathbf{X}_{lm}(\theta), \tag{B.2}$$

where $\mathbf{X}_{ln}, \mathbf{Y}_{ln}$ and $\mathbf{Z}_{ln}$ are VSHs given by,

$$\mathbf{X}_{lm}(\theta,\phi) = \frac{im}{\sin\theta}Y_l^m(\theta,\phi)\hat{e}_\theta - \frac{\partial}{\partial\theta}Y_l^m(\theta,\phi)\hat{e}_\phi, \tag{B.3}$$

$$\mathbf{Y}_{lm}(\theta,\phi) = \hat{\mathbf{e}}_r \times \mathbf{X}_{lm}(\theta,\phi), \tag{B.4}$$

$$\mathbf{Z}_{lm}(\theta,\phi) = l(l+1)Y_l^m(\theta,\phi)\hat{\mathbf{e}}_r, \tag{B.5}$$

and Y_l^m denote spherical harmonics with polar and azimuthal mode numbers l and m.

B.2 Computation of the Modes

The calculations of the WGM electric fields along with other factors discussed in Sections 2.3 and 2.4 were performed in Mathematica. In this section the Mathematica code will be presented in a manner that will allow for straight forward reproduction of the results. This code is structured as follows: all relevant physical constants and system parameters are

defined, functions are then defined for the calculation of desired parameters and a sample figure is produced.

```
Setup Physical Constants;
c = 2.99*10^8;   (* Speed of light in m/s *)
\[Mu] = 2.74*10^-29;   (* in C m *)
hbar = 1.055*10^-34;   (* in J s*)
\[Epsilon]0 = 8.85*10^-12;  (* in F m*)
nSil = 1.46071;  (* refractive index of Silica *)
nAir = 1;  (* Refractive index of Air *)
nWater = 1.33372;   (* Refractive index of Water *)
nDia = 2.419;  (* Refractive index of Diamond *)

Setup system parameters;
a = 33;  (* Radius of the sphere in microns *)
nIn = nSil;  (* Refractive index of the sphere *)
nMed = nAir;   (* Refractive index of suspending medium *)
\[Alpha]s = 2;  (* Attenuation of fused silica in dB km^-1 *)
\[Sigma]s = 0.2;  (* Surface roughness in nm *)
Ls = 5;  (* correlation length in nm *)
\[Lambda]zpl = 637; (* Zero-phonon line wavelength of NV in nm *)
kzpl = (2 \[Pi])/\[Lambda]zpl;  (* ZPL wavenumber *)
\[Gamma]dia = 4 Pi 10^7;  (* Spont. emission rate for NV *)
```

The next segment of code generates functions which approximate the fundamental WGM mode numbers and the roots of the resonance condition discussed in Section 2.3.1.2. This method of mode number calculation was originally performed in [139].

```
SchillerExpansion[n1_, n2_, q_, x_] := (x n2 )/n1 - (
   AiryAiZero[q] x^(1/3))/(
   2^(1/3) n1/n2) - (n2/n1)^2 1/Sqrt[-1 + (n1/n2)^2] + (
   3 AiryAiZero[q]^2)/(
   10 2^(2/3) (n1/n2) x^(1/3)) - (2^(2/3) AiryAiZero[q])/(
    3 (-1 + (n1/n2)^2)^(3/2) x^(2/3)) (n1/n2)^2 (n2/n1)^6 +
   AiryAiZero[q] /(
    2^(1/3) (-1 + (n1/n2)^2)^(3/2) x^(2/3)) (n1/n2)^2 (n2/n1)^2;
SchillerExpansionTE[n1_, n2_, q_, x_] := (x n2 )/n1 - (
   AiryAiZero[q] x^(1/3))/(2^(1/3) n1/n2) - 1/Sqrt[-1 + (n1/n2)^2] + (
```

```
   3 AiryAiZero[q]^2)/(
   10 2^(2/3) (n1/n2) x^(1/3)) - (2^(2/3) AiryAiZero[q])/(
    3 (-1 + (n1/n2)^2)^(3/2) x^(2/3)) (n1/n2)^2 +
   AiryAiZero[q] /(2^(1/3) (-1 + (n1/n2)^2)^(3/2) x^(2/3)) (n1/n2)^2;

Mmode[n1_, n2_, q_, rad_, \[Lambda]_] :=
 Round[(x /.
     FindRoot[(2 Pi n2 rad)/
       SchillerExpansion[n1, n2, q, x] == \[Lambda] 10^-3, {x,
       300}]) - 0.5]
zTM[n1_, n2_, q_, rad_, \[Lambda]_] :=
  N[SchillerExpansion[n1, n2, q,
    Mmode[n1, n2, q, rad, \[Lambda]] + 0.5]];
zTE[n1_, n2_, q_, rad_, \[Lambda]_] :=
  N[SchillerExpansionTE[n1, n2, q,
    Mmode[n1, n2, q, rad, \[Lambda]] + 0.5]];
```

Next the spherical Bessel functions and their derivatives are introduced along with the integration constant B in Eq.(2.57) which is labelled here as A. Mathematica's *FindRoot* function is then utilised to more accurately approximate the resonance wavenumber and the frequency of the WGM, also performed originally in [139].

```
Bessel Function Setup;
j[l_, z_] := SphericalBesselJ[l, z];
y[l_, z_] := SphericalBesselY[l, z];

dj[l_, z_] := (D[SphericalBesselJ[l, x], x] /. x -> z);
dy[l_, z_] := (D[y[l, x], x] /. x -> z);

A[nI_, nM_, rad_, k_, M_] := j[M, nI k rad]  /y[M, nM k rad]

Calculation of resonances;
kTM[nI_, nM_, q_, rad_, M_, \[Lambda]_] :=
 k /. FindRoot[
   nM/nI dj[M, nI k rad]/j[M, nI k rad] -
     dy[M, nM k rad]/y[M, nM k rad] == 0 , {k,
    zTM[nI, nM, q, rad, \[Lambda]]/rad/nM}]
```

```
kTE[nI_, nM_, q_, rad_, M_, \[Lambda]_] :=
 k /. FindRoot[
   nI/nM dj[M, nI k rad]/j[M, nI k rad] -
     dy[M, nM k rad]/y[M, nM k rad] == 0 , {k,
    zTE[nI, nM, q, rad, \[Lambda]]/rad/nM}]
\[Omega]kTM[nI_, nM_, q_, rad_, M_, \[Lambda]_] :=
 kTM[nI, nM, q, rad, M, \[Lambda]] 10^6*c
\[Omega]kTE[nI_, nM_, q_, rad_, M_, \[Lambda]_] :=
 kTE[nI, nM, q, rad, M, \[Lambda]] 10^6*c
```

A function which calculates the radial portion of the WGM electric field is then defined. This function is then used to define functions which calculate the individual electric field components of the WGM using Eqs.(B.1, B.2).

```
Radial Function;
Ri[nI_, rad_, k_, M_, r_] := j[M, nI k r]
Ro[nI_, nM_, rad_, k_, M_, r_] := A[nI, nM, rad, k, M] y[M, nM k r]
R[nI_, nM_, rad_, k_, M_, r_] :=
 With[{x = Evaluate[Ri[nI, rad, k, M, r]],
   y = Evaluate[Ro[nI, nM, rad, k, M, r]]}, If[r < rad, x, y]]

E Field Calculation Setup;
nr[r_] := If[r < a, nIn, nMed];(* Refractive index of the Sphere *)
dRtm[nI_, nM_, rad_, k_, M_, r_] :=
 D[R[nI, nM, rad, k, M, x], x] /. x -> r
X [l_, m_, \[Theta]_] := {0,
  I m/Sin[\[Theta]] SphericalHarmonicY[l, m, \[Theta], 0],
  D[SphericalHarmonicY[l, m, x, 0], x] /. x -> \[Theta]}
Z[l_, m_, \[Theta]_] := {l*(l + 1)*
   SphericalHarmonicY[l, m, \[Theta], 0], 0, 0}
Y[l_, m_, \[Theta]_] := Cross[{1, 0, 0}, X[l, m, \[Theta]]]

E Field Functions;
ETM[r_, \[Theta]_, nI_, nM_, rad_, k_, M_] :=
 1/(k nr[r]) (Y[M, M, \[Theta]] dRtm[nI, nM, rad, k, M, r] +
    1/r  R[nI, nM, rad, k, M, r] Z[M, M, \[Theta]])
```

```
AbsETMR[r_, \[Theta]_, nI_, nM_, rad_, k_, M_] :=
 Abs[ETM[r, \[Theta], nI, nM, rad, k, M][[1]]]
AbsETM\[Theta][r_, \[Theta]_, nI_, nM_, rad_, k_, M_] :=
 Abs[ETM[r, \[Theta], nI, nM, rad, k, M][[2]]]
AbsETM\[Phi][r_, \[Theta]_, nI_, nM_, rad_, k_, M_] :=
 Abs[ETM[r, \[Theta], nI, nM, rad, k, M][[3]]]

ETE[r_, \[Theta]_, nI_, nM_, rad_, k_, M_] :=
 R[nI, nM, rad, k, M, r]  X [M, M, \[Theta]]

AbsETER[r_, \[Theta]_, nI_, nM_, rad_, k_, M_] :=
 Abs[ETE[r, \[Theta], nI, nM, rad, k, M][[1]]]
AbsETE\[Theta][r_, \[Theta]_, nI_, nM_, rad_, k_, M_] :=
 Abs[ETE[r, \[Theta], nI, nM, rad, k, M][[2]]]
AbsETE\[Phi][r_, \[Theta]_, nI_, nM_, rad_, k_, M_] :=
 Abs[ETE[r, \[Theta], nI, nM, rad, k, M][[3]]]
```

Next, functions are defined to approximate the mode volume, quality factor, light-matter coupling strength *gi*, inter-mode coupling strength *gm*, maximum number of modes *Nmodes* and the cQED parameters discussed in Section 2.4.

```
Mode Volume;
Vmode[n1_, n2_, a_, \[Lambda]_] :=
 3.4 Pi^(3/2) ((\[Lambda]*10^-9)/(2 Pi n1))^3 Mmode[n1, n2, 1,
   a, \[Lambda]]^(11/6)  (* Approximation *)

WGM Quality Factor and Loss Rate;
Qscat[nI_, nM_, nScat_, q_, rad_, radscat_, \[Lambda]_,
  Nscat_] := (6 Pi nI Vmode[nI, nM,
     rad, \[Lambda]])/(8 Pi Nscat (\[Lambda]  10^-9)  (kTM[nI, nM, q,
       rad, Mmode[nI, nM, q,
        rad, \[Lambda]], \[Lambda]] 10^6)^4 nM (radscat 10^-9)^6 ((
     nI/nScat - 1)/(nI/nScat + 2))^2)

Q[nI_, nM_, rad_, \[Lambda]_, \[Alpha]_, \[Sigma]_, L_, nScat_,
  radscat_, q_,
  Nscat_] := (((\[Lambda]*10^-9) \[Alpha])/(2 \[Pi] nI 4.3 10^3) + (
```

```
   8 \[Pi]^2 (\[Sigma]*10^-9)^2 (L*10^-9)^2)/(
   3 (\[Lambda]*10^-9)^4 Mmode[nI, nM, 1, rad, \[Lambda]]^(1/3)) +
   Qscat[nI, nM, nScat, q, rad, radscat, \[Lambda], Nscat]^-1)^-1
gM[nI_, nM_, nScat_, \[Lambda]_, radscat_, rad_] := (
  4 Pi  (radscat 10^-9)^3 ((nI^2 - nScat^2)/(nI^2 + 2 nScat^2)))/(
  2 Vmode[nI, nM, rad, \[Lambda]]) (2 Pi c)/(\[Lambda] 10^-9)

\[Kappa]appa[nI_, nM_, q_, rad_, \[Lambda]_, \[Alpha]_, \[Sigma]_, L_,
   nScat_, radscat_, Nscat_] :=
 2 Pi \[Omega]kTM[nI, nM, q, rad,
   Mmode[nI, nM, q, rad, \[Lambda]], \[Lambda]]/
  Q[nI, nM, rad, \[Lambda], \[Alpha], \[Sigma], L, nScat, radscat, q,
   Nscat]

cQED Parameters;
gi[nI_, nM_, q_,
  rad_, \[Lambda]_] := \[Mu] Sqrt[\[Omega]kTM[nI, nM, q, rad,
   Mmode[nI, nM, q, rad, \[Lambda]], \[Lambda]]/(
  2 hbar \[Epsilon]0 Vmode[nI, nM, rad, \[Lambda]])]
Nmodes[r_] :=
 N[2*\[Pi]*
   Sqrt[Mmode[nIn, nMed, 1, r, \[Lambda]zpl]]/(2*Sqrt[2*Log[2]])]

gE[nI_, nM_, q_, rad_, \[Lambda]_] :=
 Sqrt[Nmodes[rad]] gi[nI, nM, q, rad, \[Lambda]]
Coop[nI_, nM_, q_, rad_, \[Lambda]_, \[Alpha]_, \[Sigma]_, L_, nScat_,
   radscat_, Nscat_] := gE[nI, nM, q, rad, \[Lambda]]^2/(
 2 \[Kappa]appa[nI, nM, q, rad, \[Lambda], \[Alpha], \[Sigma], L,
   nScat, radscat, Nscat] \[Gamma]dia) (* Cooperativity  *)
P[nI_, nM_, rad_, \[Lambda]_, \[Alpha]_, \[Sigma]_, L_] :=
 3*((\[Lambda]*10^-9)/nI)^3 Q[nI, rad, \[Lambda], \[Alpha], \[Sigma],
   L]/(4 \[Pi]^2 Vmode[nI, nM, rad, \[Lambda]])(* Purcell Factor *)
n0[nI_, nM_, q_, rad_, \[Lambda]_] := \[Gamma]dia^2/(
 2 gE[nI, nM, q, rad, \[Lambda]]^2) (* Saturation photon number*)
LineSep[nI_, nM_, q_, rad_, \[Lambda]_, \[Alpha]_, \[Sigma]_, L_,
  nScat_, radscat_, Nscat_] := ((
```

```
 2 gE[nI, nM, q, rad, \[Lambda]])/(\[Kappa]appa[nI, nM, q,
   rad, \[Lambda], \[Alpha], \[Sigma], L, nScat, radscat,
   Nscat] + \[Gamma]dia))
```

Finally, code for the generation of a sample figure is provided. The fundamental mode number l_{max} is first determined and used to calculate the resonant wavenumber of the mode. These parameters are then used to generate a plot of the WGM electric field components.

```
M = Mmode[nIn, nMed, 1, a, \[Lambda]zpl];
ktm = kTM[nIn, nMed, 1, a, M, \[Lambda]zpl];
kte = kTE[nIn, nMed, 1, a, M, \[Lambda]zpl];

Plot[{AbsETMR[r, Pi/2, nIn, nMed, a, ktm, M]/3.2,
  AbsETM\[Phi][r, Pi/2, nIn, nMed, a, ktm, M]/3.2,
  AbsETE\[Theta][r, Pi/2, nIn, nMed, a,
    zTE[nIn, nMed, 1, a, \[Lambda]zpl]/a, M]/3.24}, {r, 32, 33.2}]
```

Appendix C

Evolution of the MITM Model

C.1 Dynamics of the MITM Model

In order to analytically analyse the dynamics of the MITM model in the high/low opacity regimes it was stated in Section 3.2.2 that the system was evolved in the Heisenberg picture. In this section the Heisenberg equations of motion will be derived and solved in both opacity regimes. The high opacity regime will first be considered. Recall that in this regime ($J \ll g, \Omega$) the interaction picture Hamiltonian is given by,

$$\hat{H}_I^{(1)} = \hbar\Omega\hat{b}^\dagger\hat{b} - \hbar g_0 \left(\hat{b}^\dagger + \hat{b}\right)\hat{\Delta}. \tag{C.1}$$

As $\hat{\Delta}$ is conserved in this regime, $\left[\hat{H}_I^{(1)}, \hat{\Delta}\right] = 0$, it can be treated as time independent. Evolution of the mechanical annihilation operator, $\hat{b}$, through the use of the Heisenberg equations of motion gives,

$$\dot{\hat{b}} = \frac{i}{\hbar}\left[\hat{H}_I^{(1)}, \hat{b}\right] = -i\Omega\hat{b} + ig_0\hat{\Delta}. \tag{C.2}$$

As $\hat{\Delta}$ is conserved, Eq.(C.2) is just a separable first order ordinary differential equation with the solution,

$$\hat{b}(t) = \left(\hat{b}(0) - \frac{g_0}{\Omega}\hat{\Delta}\right)e^{-i\Omega t} + \frac{g_0}{\Omega}\hat{\Delta}. \tag{C.3}$$

The expectation value of the membrane's position can now be calculated,

$$\begin{aligned}\langle\hat{x}\rangle &= x_{ZPF}\langle\hat{b}(t)+\hat{b}^{\dagger}(t)\rangle \\ &= x_{ZPF}\langle\beta_M,\alpha_L,\alpha_R|\hat{b}(t)+\hat{b}^{\dagger}(t)|\beta_M,\alpha_L,\alpha_R\rangle \\ &= \frac{4g_0x_{ZPF}}{\Omega}\Delta\sin^2\left(\frac{\Omega t}{2}\right)+x_{ZPF}\left({\beta_M}^*e^{i\Omega t}+\beta_M e^{-i\Omega t}\right).\end{aligned} \tag{C.4}$$

Next the dynamics in the transmissive membrane regime will be solved for. Here recall that the interaction picture Hamiltonian is,

$$\hat{H}_I^{(2)} = -\hbar J\left(\hat{a}_L^{\dagger}\hat{a}_R+\hat{a}_R^{\dagger}\hat{a}_L\right). \tag{C.5}$$

The Heisenberg EOMs for the cavity mode operators, $\hat{a}_{L/R}$, in this regime are,

$$\dot{\hat{a}}_{L,R} = \frac{i}{\hbar}\left[\hat{H}_I^{(2)},\hat{a}_{L,R}\right] = iJ\hat{a}_{R,L}. \tag{C.6}$$

Taking the derivative of this equation gives,

$$\ddot{\hat{a}}_{L,R} = \frac{i}{\hbar}\left[\hat{H}_I^{(2)},\hat{a}_{L,R}\right] = iJ\dot{\hat{a}}_{R,L}, \tag{C.7}$$

which can be reduced to a second order differential equation by substitution of Eq.(C.6),

$$\ddot{\hat{a}}_{L,R} = iJ^2\hat{a}_{L,R}. \tag{C.8}$$

Thus the solutions to the Heisenberg equations of motion for the cavity mode operators are,

$$\hat{a}_{L,R}(t) = \hat{a}_{L,R}(0)\cos(Jt)+i\hat{a}_{R,L}(0)\sin(Jt), \tag{C.9}$$

where the initial conditions $\dot{\hat{a}}_{L,R}(0) = iJ\hat{a}_{R,L}(0)$ have been applied. The expectation values of the cavity mode number operators are then,

$$\begin{aligned}\langle\hat{a}_{L,R}^{\dagger}\hat{a}_{L,R}\rangle &= \langle\beta_M,\alpha_L,\alpha_R|\hat{a}_{L,R}^{\dagger}(t)\hat{a}_{L,R}(t)|\beta_M,\alpha_L,\alpha_R\rangle \\ &= |\alpha_{L,R}|^2\cos^2(Jt)+|\alpha_{R,L}|^2\sin^2(Jt).\end{aligned}$$

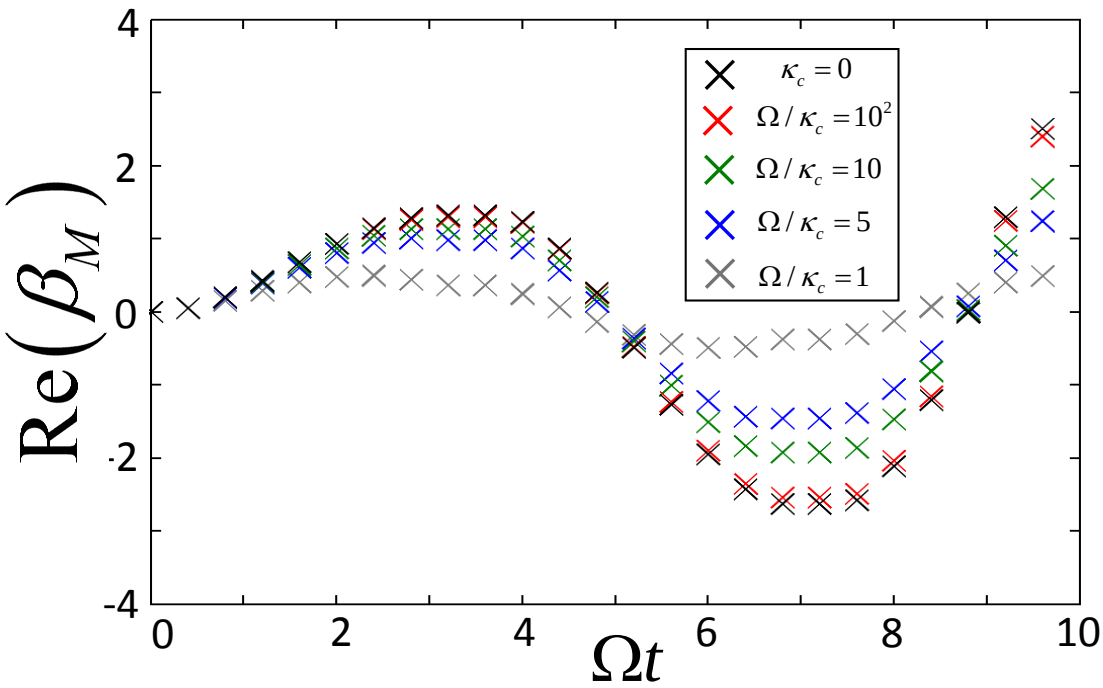

Figure C.1: The dynamics of a BEC's position when the system is initialised in the state $|\psi(0)\rangle = |0_M, 2, 0\rangle$ using several cavity dampening rates, κ_c. The simulations were performed in units of Ω with $g_0 = 32.8\Omega$ and $N_{Flips} = t/\tau_{Flip} = t\frac{\Omega}{\pi}$.

C.2 Simulations

The simulations performed throughout Chapter 3 were performed through the use of the MATLAB qotoolbox package. This package was used to evolve the MITM system by solving the full master equation. While simulations were also performed in QuTip, the successor of qotoolbox, it was found that the QuTip's time dependant Hamiltonian solver was not completely compatible with the fast alternation between the high opacity regime Hamiltonian and the transmissive regime Hamiltonian. The code is structured in the following manner: all relevant parameters are first defined, operators are then constructed and integration settings selected then finally integration is performed using qotoolbox's master equation solver.

The first segment of code is dedicated to defining all relevant parameters for the system. Here the simulations were performed by rescaling the system with respect to the mechanical frequency. A further scaling of the optomechanical coupling rate was required to significantly reduce the size of the membrane's Hilbert space, allowing for efficient simulations and the ability to calculate the Wigner function of the final state. The only effect this scaling has on the dynamics is to reduce the magnitude of the membrane's displacement by the scaling factor. For this reason, this scaling is reversed in the calculation of the zero point fluctuation

amplitude to give the unscaled displacement.

```
% Input system parameters Realistic parameters from BEC paper:
greal = 2*pi*0.5*10^6;        % Optomechanical coupling rate
wmreal = 2*pi*15.2*10^3;      % Mechanical frequency
kappareal = 2*pi*2.6*10^3;    % Cavity Damping Rate

% Rescale the model in units of wm:
kappa = kappareal/wmreal;
g = greal/wmreal/100;         % Scale by 100 for simulation
wm = 1;

% Input physical parameters
hbar = 1.055*10^-34;
nRb = 1.2*10^5;               % Number of Rb87 atoms
massRb = 86.9;                % mass of Rb87 in amu
amutokg = 1.6605*10^-27;      % convert amu to kg
m=nRb*massRb*amutokg;         % mass in kg
xzpf = sqrt(hbar/(2*m*wmreal));
xnm = xzpf/10^-9;
xnmreal = xnm*100;            % Undo scaling g by 100
pzpf = sqrt(m*hbar*wmreal/2); % in kg m/s
pg = pzpf*1000;               % in g m/s
pnm = pg*10^18;               % in ng nm /s

% Setting up size of Hilbert spaces and # of photons in cavity:
Nmax = 3;       % Number of photons in the entire cavity
NL=3;           % Number of photons in the left - 1
NR=1;           % Number of photons in the right - 1
Nt=40;          % Size of membrane Hilbert space
J=30*pi;        % Membrane transmision rate
```

Next the membrane and cavity operators are constructed and a coherent state generating function is introduced. The operators are then used to construct the two Hamiltonians and the Liouvillian operators for the consideration of dissipative effects. In this segment of code the projection operator is also constructed through the use of the *make_projector* function.

```
% Setting up the identities
```

```
% Identity for the cavity modes:
id_cav=identity(Nmax);

% Identity of membrane:
id_mem=identity(Nt);

% Cavity mode operators
aL = tensor(id_mem, destroy(Nmax), id_cav);
aR = tensor(id_mem, id_cav,destroy(Nmax));

% The membrane annihilation operator
b=tensor(destroy(Nt),id_cav,id_cav);

% The membrane's position operator
x = (b'+b);

% Introduce a function which can be used to generate coherent states
coh = destroy(Nt);
coherent =@(a)expm(a*coh'-a'*coh);

% The Hamiltonian in the high opacity regime (opaque)
Ho = wm*(b)'*b-g*(b + b')*(aL'*aL - aR'*aR);

% The Hamiltonian in the low opacity regime (transmissive)
Ht = -J*(aL'*aR+aR'*aL);

% Set up the flipping operator for the disentanglement projector
Hflip = (pi/2)*(-aL'*aR + aL*aR');
Uflip = expm(Hflip);

% The disentanglement projector
[neg_proj,pos_proj]=make_projector(Nt);
projector =Uflip*tensor(pos_proj,id_cav,id_cav)+...
 tensor(neg_proj,id_cav,id_cav);

% Start setting up the operators to solve the full master equation
```

```
% The collapse operators
CL = sqrt(kappa)*aL;
CR = sqrt(kappa)*aR;
CLdCL = CL'*CL;
CRdCR = CR'*CR;

% The Liouvillian
% In the unitary case:
LHo = -1i * (spre(Ho) - spost(Ho));
LHt = -1i*(spre(Ht) - spost(Ht));
% With the consideration of dissipation:
LL = spre(CL)*spost(CL')-0.5*spre(CLdCL)-0.5*spost(CLdCL);
LR = spre(CR)*spost(CR')-0.5*spre(CRdCR)-0.5*spost(CRdCR);
LHoD = LHo+LL+LR;
LHtD = LHt + LL +LR;
```

With the system parameters prepared and the operators constructed the integration settings are defined and initial conditions selected. As two evolutions are performed simultaneously, one to generate a cat state and the other to determine its size for the fidelity calculations, two separate initial conditions are required.

```
% Set up equation solver options
options.lmm = 'ADAMS';
options.iter = 'FUNCTIONAL';
options.reltol = 1e-8;
options.abstol = 1e-8;

% Set up an integration loop
Nflips = 1;                 % Number of flips (Uflip applications)
dt = 0.05;                  % Integration timestep
tlist1 = 0:dt:pi/wm;        % Ho Propergation time
tlist2 = 0:dt:30*pi/(2*J);  % Ht Propergation time
tlist3 = 0:dt:pi/wm+dt;     % Final Ho prop time
xvec = -10:0.1:10;          % Dimensions for Wigner function
Nfid = length(tlist1)+length(tlist2);
fid1 = 0.*(0:Nflips*(length(tlist1)+length(tlist2))+length(tlist3)-1);
fid2 = fid1;
```

```
as = fid1;

% Here the type of evolution is selected
% Switch to LHo and LHt for unitary evolution
Lo = LHo;
Lt = LHt;

% Setup the initial states which will be used
% Initialise the cavity modes in a NOON state and the membrane in its
% ground state - this is for creating a cat state.
psisup = sqrt(0.5)*tensor(basis(Nt,1),...
    tensor(basis(Nmax,NL),basis(Nmax,NR))...
    +tensor(basis(Nmax,NR),basis(Nmax,NL)));
% Initialise the cavity modes in number states and the membrane in its
% ground state - this is for simulating the membrane's displacement.
psiclean = tensor(basis(Nt,1), basis(Nmax,NL),basis(Nmax,NR));

% Set initial condition:
psi0 = psisup;
% Initial state for cat state creation
rho0=psi0*psi0';
% Initial state for membrane displacement
rhoclean = psiclean*psiclean';
```

The next segment of code is dedicated to evolving the system. As qotoolbox is not compatible with time dependant Hamiltonians the evolution is made by sequentially evolving under each of the Hamiltonians. The repeated application of flips is achieved through the use of a loop where at the end the system is finally evolved in the high opacity regime. Within this loop the results are stored within appropriately labelled arrays. The final segment concludes with the calculation of the Wigner function of the final state.

```
% Evolve the system
for i =  0:Nflips-1
%%%%%%%%%%%%%%%%%%%%%%%%%%%%%%%%%%%%%%%%%%%%%%%%%%%%%%%%%%%%%%%%%%%%%%%%%%%%%%%%
%%%%%%%%%%%%%%% Simulation of the membrane's displacement %%%%%%%%%%%%%%%
%%%%%%%%%%%%%%%%%%%%%%%%%%%%%%%%%%%%%%%%%%%%%%%%%%%%%%%%%%%%%%%%%%%%%%%%%%%%%%%%
% Evolve the system under Ho
```

```
ode2file('file1.dat',Lo,rhoclean,tlist1,options);
odesolve('file1.dat','file2.dat');
fid = fopen('file2.dat','rb');
rhoa1 = qoread(fid,dims(rhoclean),size(tlist1));
fclose(fid);

% Calculate the membrane's coherent amplitude under this evolution
for ns = 1:length(tlist1)
    as(i*Nfid +ns) = trace(b*rhoa1{ns});
end
rhoa1end = rhoa1{length(tlist1)};

% Evolve the system under Ht
ode2file('file1.dat',Lt,rhoa1end,tlist2,options);
odesolve('file1.dat','file2.dat');
fid = fopen('file2.dat','rb');
rhoa2 = qoread(fid,dims(rhoa1end),size(tlist2));
fclose(fid);

% Calculate the membrane's coherent amplitude under this evolution
for ns = 1:length(tlist2)
    as(i*Nfid +length(tlist1)+ns) = trace(b*rhoa2{ns});
end
rhoclean = rhoa2{length(tlist2)};

%%%%%%%%%%%%%%%%%%%%%%%%%%%%%%%%%%%%%%%%%%%%%%%%%%%%%%%%%%%%%%%%%%%%%%%%%%
%%%%%%%%%%%%%%%%%% Simulation of cat state generation %%%%%%%%%%%%%%%%%%%%
%%%%%%%%%%%%%%%%%%%%%%%%%%%%%%%%%%%%%%%%%%%%%%%%%%%%%%%%%%%%%%%%%%%%%%%%%%

% Evolve the system under Ho
ode2file('file1.dat',Lo,rho0,tlist1,options);
odesolve('file1.dat','file2.dat');
fid = fopen('file2.dat','rb');
rho = qoread(fid,dims(rho0),size(tlist1));
fclose(fid);
```

```
% Save the evolved state
rhobf=rho{length(tlist1)};

% Calculate the fidelity of the membrane's state with a cat state
for alphas = 1:length(tlist1)

    % Generate odd and even cat states
    alpha = as(i*Nfid +alphas);
    cat1 = tensor(coherent(alpha)*basis(Nt,1)+...
     coherent(-alpha)*basis(Nt,1),basis(Nmax,NL),basis(Nmax,NR));
    norm = cat1'*cat1;
    norm = full(norm(:,:));
    cat1 = cat1/sqrt(norm);
    cat2 = (tensor(coherent(alpha)*basis(Nt,1)+...
     coherent(-alpha)*basis(Nt,1),basis(Nmax,NR),...
     basis(Nmax,NL)))/sqrt(norm);
    % Calculate the fidelity
    fid1(i*Nfid+alphas)=cat1'*projector*rho{alphas}*projector'*cat1;
    fid2(i*Nfid+alphas)=cat2'*projector*rho{alphas}*projector'*cat2;

end

% Evolve the system under Ht
ode2file('file1.dat',Lt,rhobf,tlist2,options);
odesolve('file1.dat','file2.dat');
fid = fopen('file2.dat','rb');
rhoaf = qoread(fid,dims(rhobf),size(tlist2));
fclose(fid);

% Calculate the fidelity of the membrane's state with a cat state
for alphas = 1:length(tlist2)
    % Generate odd and even cat states
    alpha = as(i*Nfid +length(tlist1)+alphas);
    cat1 = tensor(coherent(alpha)*basis(Nt,1)+...
     coherent(-alpha)*basis(Nt,1),basis(Nmax,NL),basis(Nmax,NR));
    norm = cat1'*cat1;
```

```
    norm = full(norm(:,:));
    cat1 = cat1/sqrt(norm);
    cat2 = (tensor(coherent(alpha)*basis(Nt,1)+...
     coherent(-alpha)*basis(Nt,1),basis(Nmax,NR),...
         basis(Nmax,NL)))/sqrt(norm);
    % Calculate the fidelity
    fid1(i*Nfid+length(tlist1)+alphas)=cat1'*...
     projector*rhoaf{alphas}*projector'*cat1;
    fid2(i*Nfid+length(tlist1)+alphas)=cat2'*...
     projector*rhoaf{alphas}*projector'*cat2;

end

% Save rho after flip
rho0 = rhoaf{length(tlist2)};

end

% Propergate under Ho for a bit longer for beta's:
ode2file('file1.dat',Lo,rhoclean,tlist3,options);
odesolve('file1.dat','file2.dat');
fid = fopen('file2.dat','rb');
rhoa1 = qoread(fid,dims(rhoclean),size(tlist3));
fclose(fid);

% Calculate the membrane's coherent amplitude under this evolution
for ns = 1:length(tlist3)
    as(Nflips*Nfid +ns) = trace(b*rhoa1{ns});
end

% Evolve under Ho for fids:
ode2file('file1.dat',Lo,rho0,tlist3,options);
odesolve('file1.dat','file2.dat');
fid = fopen('file2.dat','rb');
rho = qoread(fid,dims(rho0),size(tlist3));
fclose(fid);
```

```
% Calculate the fidelity of the membrane's state with a cat state
for alphas = 1:length(tlist3)
    % Generate odd and even cat states
    alpha = as(Nflips*Nfid+alphas);
    cat1 = tensor(coherent(alpha)*basis(Nt,1)+...
     coherent(-alpha)*basis(Nt,1),basis(Nmax,NL),basis(Nmax,NR));
    norm = cat1'*cat1;
    norm = full(norm(:,:));
    cat1 = cat1/sqrt(norm);
    cat2 = (tensor(coherent(alpha)*basis(Nt,1)+...
    coherent(-alpha)*basis(Nt,1),basis(Nmax,NR),...
     basis(Nmax,NL)))/sqrt(norm);
    % Calculate the fidelity
    fid1(Nflips*Nfid+alphas)=cat1'*projector*rho{alphas}*projector'*cat1;
    fid2(Nflips*Nfid+alphas)=cat2'*projector*rho{alphas}*projector'*cat2;

end

% Calculate the Wigner function of the final state
rhomemz = ptrace(projector*rho{32}*projector',1);
Wigzcalc = wfunc(rhomemz,xvec,xvec,2);
```

The code which defines the *make_projector* function is presented below. This function takes the dimension of the membrane's Hilbert space and produces the eigenstates of the position operator.

```
function [nneg_proj,ppos_proj]=make_projector(Nt)

b=destroy(Nt);
x=(b+b')/2;
xx=full(x(:,:));
[mat1,eig1]=eig(xx);
diageig=diag(eig1);
[sorteig,ii]=sort(diageig);
vecs=zeros(size(mat1));
[nn,mm]=size(vecs);
```

```
for j=1:mm,
    vecs(:,j)=mat1(:,ii(j));
end
identity1=zeros(size(mat1));
neg_proj=zeros(size(mat1));
pos_proj=zeros(size(mat1));


for j=1:(Nt),
    identity1=identity1+vecs(:,j)*vecs(:,j)';
end
icut=find(sorteig>0,1)-1;
for j=1:icut,
    neg_proj=neg_proj+vecs(:,j)*vecs(:,j)';
end

for j=icut+1:Nt,
    pos_proj=pos_proj+vecs(:,j)*vecs(:,j)';
end
ppos_proj=qo(pos_proj);
nneg_proj=qo(neg_proj);
```

List of Symbols

The following list is neither exhaustive nor exclusive, but may be helpful.

Chapter 2

ω ..... resonance frequency.

ϵ_0 ..... vacuum permittivity constant.

$\hbar$ ..... Planck constant.

c ..... speed of light.

E_0 ..... electric field normalisation constant.

g ..... interaction rate between a single spin and a single mode of light.

Δ_D ..... atom/cavity detuning.

Ω_R ..... Rabi-frequency.

κ ..... cavity damping rate of a cavity mode.

γ ..... spontaneous emission rate of a spin.

$\bar{\omega}$ ..... average of the mode resonance frequencies.

a ..... radius of the spherical resonator.

n ..... refractive index.

ζ_q ..... q^{th} root of the Airy function.

l_{max} ..... polar mode number of the fundamental WGM.

ϵ_s ..... eccentricity of the spherical resonator.

V_{mode} ..... the mode volume.

Q ..... quality factor.

σ_{np} ..... classical cross section of a spherical nano-particle.

ξ ..... Debye-Waller factor.

σ_L/σ_R ..... Left/Right hand circularly polarised light.

$\alpha(t)$ ..... probability amplitude that a spin is excited.

$C(t)$ ..... probability amplitude that a mode is excited.

$\psi(r,\theta,\phi)$ .... solution to the scalar Helmholtz equation.

j_l/y_l ..... spherical Bessel functions of the first/second kinds.

J_l ..... Bessel function of the first kind.

h_l ..... Hankel function.

P_l^m/Q_l^m ..... associated Legendre functions of the first/second kinds.

Y_l^m ..... Spherical Harmonics.

$D^l_{m',l}$ ..... Wigner D function.

$\hat{H}$ ..... Hamiltonian operator.

$\hat{a}$ ..... cavity mode annihilation operator.

$\hat{a}^\dagger$ ..... cavity mode creation operator.

$\hat{\sigma}_z$ ..... Pauli z spin operator.

$\hat{\mathbf{d}}$ ..... atomic dipole operator.

$\hat{\mathbf{E}}$ ..... cavity mode electric field operator.

$\hat{I}$ ..... identity operator.

$\hat{\sigma}_+/\hat{\sigma}_-$ ..... atomic raising/lowering operators.

$\hat{\Sigma}_\pm$ ..... collective spin raising and lowering operators.

$\hat{A}$ ..... collective mode annihilation operator.

$\hat{\rho}$ ..... density operator.

$\mathbf{H}$ ..... magnetic vector potential.

$\mathbf{D}$ ..... electric displacement vector.

$\mathbf{B}$ ..... magnetic field vector.

Chapter 3

Ω ..... mechanical frequency of the membrane.

J ..... transmission rate of the membrane.

x_{ZPF} ..... zero point fluctuation amplitude.

g_0 ..... optomechanical coupling strength.

Δ ..... difference between the left/right cavity photon numbers.

β_M ..... coherent amplitude of the membrane.

γ_M ..... mechanical damping rate.

κ_c ..... optical damping rate.

$\hat{a_L}/\hat{a_R}/\hat{b}$ ..... annihilation operators of the left/right cavity modes and the mechanical mode.

$\hat{x}$ ..... position operator of the membrane.

$\hat{\Delta}$ ..... photon number difference operator.

$\hat{B}$ ..... Beam Splitter operator.

$\hat{S}$ ..... Squeezing operator.

$\hat{P}$ ..... disentanglement projector.

References

[1] G. D. Fuchs, G. Burkard, P. V. Klimov, and D. D. Awschalom. *A quantum memory intrinsic to single nitrogen-vacancy centres in diamond.* Nature Physics **7**(10), 789 (2011).

[2] K. Saeedi, S. Simmons, J. Z. Salvail, P. Dluhy, H. Riemann, N. V. Abrosimov, P. Becker, H.-J. Pohl, J. J. L. Morton, and M. L. W. Thewalt. *Room-temperature quantum bit storage exceeding 39 minutes using ionized donors in silicon-28.* Science **342**(6160), 830 (2013).

[3] P. C. Maurer, G. Kucsko, C. Latta, L. Jiang, N. Y. Yao, S. D. Bennett, F. Pastawski, D. Hunger, N. Chisholm, M. Markham, D. J. Twitchen, J. I. Cirac, and M. D. Lukin. *Room-temperature quantum bit memory exceeding one second.* Science **336**(6086), 1283 (2012).

[4] W. F. Koehl, B. B. Buckley, F. J. Heremans, G. Calusine, and D. D. Awschalom. *Room temperature coherent control of defect spin qubits in silicon carbide.* Nature **479**(7371), 84 (2011).

[5] F. Jelezko, T. Gaebel, I. Popa, A. Gruber, and J. Wrachtrup. *Observation of coherent oscillations in a single electron spin.* Physical Review Letters **92**(7), 076401 (2004).

[6] M. J. Holmes, K. Choi, S. Kako, M. Arita, and Y. Arakawa. *Room-temperature triggered single photon emission from a III-nitride site-controlled nanowire quantum dot.* Nano Letters **14**(2), 982 (2014).

[7] M. V. G. Dutt, L. Childress, L. Jiang, E. Togan, J. Maze, F. Jelezko, A. S. Zibrov, P. R. Hemmer, and M. D. Lukin. *Quantum register based on individual electronic and nuclear spin qubits in diamond.* Science **316**(5829), 1312 (2007).

[8] I. Aharonovich, S. Castelletto, D. A. Simpson, C.-H. Su, A. D. Greentree, and S. Prawer. *Diamond-based single-photon emitters.* Reports on Progress in Physics **74**(7), 076501 (2011).

[9] E. Neu, D. Steinmetz, J. Riedrich-Mller, S. Gsell, M. Fischer, M. Schreck, and C. Becher. *Single photon emission from silicon-vacancy colour centres in chemical vapour deposition nano-diamonds on iridium.* New Journal of Physics **13**(2), 025012 (2011).

[10] A. D. Boozer, A. Boca, R. Miller, T. E. Northup, and H. J. Kimble. *Reversible state transfer between light and a single trapped atom.* Physical Review Letters **98**(19), 193601 (2007).

[11] L.-M. Duan, M. D. Lukin, J. I. Cirac, and P. Zoller. *Long-distance quantum communication with atomic ensembles and linear optics.* Nature **414**(6862), 413 (2001).

[12] M. A. Sillanp, J. I. Park, and R. W. Simmonds. *Coherent quantum state storage and transfer between two phase qubits via a resonant cavity.* Nature **449**(7161), 438 (2007).

[13] S. Ritter, C. Nlleke, C. Hahn, A. Reiserer, A. Neuzner, M. Uphoff, M. Mcke, E. Figueroa, J. Bochmann, and G. Rempe. *An elementary quantum network of single atoms in optical cavities.* Nature **484**(7393), 195 (2012).

[14] A. Boca, R. Miller, K. M. Birnbaum, A. D. Boozer, J. McKeever, and H. J. Kimble. *Observation of the vacuum rabi spectrum for one trapped atom.* Physical Review Letters **93**(23), 233603 (2004).

[15] M. Steiner, H. M. Meyer, C. Deutsch, J. Reichel, and M. Khl. *Single ion coupled to an optical fiber cavity.* Physical Review Letters **110**(4), 043003 (2013).

[16] P. F. Herskind, A. Dantan, J. P. Marler, M. Albert, and M. Drewsen. *Realization of collective strong coupling with ion coulomb crystals in an optical cavity.* Nature Physics **5**(7), 494 (2009).

[17] M. Cetina, A. Bylinskii, L. Karpa, D. Gangloff, K. M. Beck, Y. Ge, M. Scholz, A. T. Grier, I. Chuang, and V. Vuleti. *One-dimensional array of ion chains coupled to an optical cavity.* New Journal of Physics **15**(5), 053001 (2013).

[18] Y. Colombe, T. Steinmetz, G. Dubois, F. Linke, D. Hunger, and J. Reichel. *Strong atomfield coupling for boseeinstein condensates in an optical cavity on a chip.* Nature **450**(7167), 272 (2007).

[19] C. Monroe, D. M. Meekhof, B. E. King, and D. J. Wineland. *A schrdinger cat superposition state of an atom.* Science **272**(5265), 1131 (1996).

[20] S. Delglise, I. Dotsenko, C. Sayrin, J. Bernu, M. Brune, J.-M. Raimond, and S. Haroche. *Reconstruction of non-classical cavity field states with snapshots of their decoherence.* Nature **455**(7212), 510 (2008).

[21] W. Marshall, C. Simon, R. Penrose, and D. Bouwmeester. *Towards quantum superpositions of a mirror.* Physical Review Letters **91**(13), 130401 (2003).

[22] D. Vitali, S. Gigan, A. Ferreira, H. R. Bhm, P. Tombesi, A. Guerreiro, V. Vedral, A. Zeilinger, and M. Aspelmeyer. *Optomechanical entanglement between a movable mirror and a cavity field.* Physical Review Letters **98**(3), 030405 (2007).

[23] S. Bose, K. Jacobs, and P. L. Knight. *Preparation of nonclassical states in cavities with a moving mirror.* Physical Review A **56**(5), 4175 (1997).

[24] C. Wipf, T. Corbitt, Y. Chen, and N. Mavalvala. *Route to ponderomotive entanglement of light via optically trapped mirrors.* New Journal of Physics **10**(9), 095017 (2008).

[25] Z.-q. Yin, T. Li, X. Zhang, and L. M. Duan. *Large quantum superpositions of a levitated nanodiamond through spin-optomechanical coupling.* Physical Review A **88**(3), 033614 (2013).

[26] O. Romero-Isart, A. C. Pflanzer, F. Blaser, R. Kaltenbaek, N. Kiesel, M. Aspelmeyer, and J. I. Cirac. *Large quantum superpositions and interference of massive nanometer-sized objects.* Physical Review Letters **107**(2), 020405 (2011).

[27] Y. Chen. *Macroscopic quantum mechanics: theory and experimental concepts of optomechanics.* Journal of Physics B: Atomic, Molecular and Optical Physics **46**(10), 104001 (2013).

[28] A. Bassi, K. Lochan, S. Satin, T. P. Singh, and H. Ulbricht. *Models of wave-function collapse, underlying theories, and experimental tests.* Reviews of Modern Physics **85**(2), 471 (2013).

[29] Z.-q. Yin, T. Li, X. Zhang, and L. M. Duan. *Large quantum superpositions of a levitated nanodiamond through spin-optomechanical coupling.* Physical Review A **88**(3), 033614 (2013).

[30] K. Hennessy, A. Badolato, M. Winger, D. Gerace, M. Atature, S. Gulde, S. Fält, E. L. Hu, and A. Imamoglu. *Quantum nature of a strongly coupled single quantum dot–cavity system.* Nature **445**(7130), 896 (2007).

[31] Y.-C. Liu, Y.-F. Xiao, B.-B. Li, X.-F. Jiang, Y. Li, and Q. Gong. *Coupling of a single diamond nanocrystal to a whispering-gallery microcavity: Photon transport benefitting from Rayleigh scattering.* Science **319**(5866), 1062 (2008).

[32] J. D. Thompson, T. G. Tiecke, N. P. de Leon, J. Feist, A. V. Akimov, M. Gullans, A. S. Zibrov, V. Vuletic, and M. D. Lukin. *Coupling a Single Trapped Atom to a Nanoscale Optical Cavity.* Science **340**(6137), 1202 (2013).

[33] W. Chen, K. M. Beck, R. Bucker, M. Gullans, M. D. Lukin, H. Tanji-Suzuki, and V. Vuletic. *All-Optical Switch and Transistor Gated by One Stored Photon.* Science **341**(6147), 768 (2013).

[34] A. D. Greentree, C. Tahan, J. H. Cole, and L. C. L. Hollenberg. *Quantum phase transitions of light.* Nat Phys **2**(12), 856 (2006).

[35] M. J. Hartmann, F. G. S. L. Brandao, and M. B. Plenio. *Strongly interacting polaritons in coupled arrays of cavities.* Nat Phys **2**(12), 849 (2006).

[36] D. Rossini and R. Fazio. *Mott-Insulating and Glassy Phases of Polaritons in 1D Arrays of Coupled Cavities.* Phys Rev Lett **99**(18), 186401 (2007).

[37] M. J. Hartmann, F. G. S. L. Brandao, and M. B. Plenio. *Quantum many-body phenomena in coupled cavity arrays.* Laser & Photonics Review **2**(6), 527 (2008).

[38] I. Buluta and F. Nori. *Quantum Simulators.* Science **326**(5949), 108 (2009).

[39] H. J. Kimble. *The quantum internet.* Nature **453**(7198), 1023 (2008).

[40] W. J. Munro, A. M. Stephens, S. J. Devitt, K. A. Harrison, and K. Nemoto. *Quantum communication without the necessity of quantum memories.* Nature Photon **6**(1), 777 (2012).

[41] S. Ritter, C. Nölleke, C. Hahn, A. Reiserer, A. Neuzner, M. Uphoff, M. Mücke, E. Figueroa, J. Bochmann, and G. Rempe. *An elementary quantum network of single atoms in optical cavities.* Nature **484**(7393), 195 (2012).

[42] W. J. Munro, K. A. Harrison, A. M. Stephens, S. J. Devitt, and K. Nemoto. *From quantum multiplexing to high-performance quantum networking.* Nature Photon **4**(1), 792 (2010).

[43] A. Stephens, Z. Evans, S. Devitt, A. Greentree, A. Fowler, W. Munro, J. O'Brien, K. Nemoto, and L. Hollenberg. *Deterministic optical quantum computer using photonic modules.* Phys Rev A **78**(3), 032318 (2008).

[44] C.-H. Su, A. Greentree, W. Munro, K. Nemoto, and L. Hollenberg. *High-speed quantum gates with cavity quantum electrodynamics.* Phys Rev A **78**(6), 062336 (2008).

[45] S. J. Devitt, A. G. Fowler, A. M. Stephens, A. D. Greentree, L. C. L. Hollenberg, W. J. Munro, and K. Nemoto. *Architectural design for a topological cluster state quantum computer.* New J Phys **11**(8), 083032 (2009).

[46] K. Nemoto, M. Trupke, S. J. Devitt, A. M. Stephens, B. Scharfenberger, K. Buczak, T. Nbauer, M. S. Everitt, J. Schmiedmayer, and W. J. Munro. *Photonic architecture for scalable quantum information processing in diamond.* Physical Review X **4**(3), 031022 (2014).

[47] T. Niemczyk, F. Deppe, H. Huebl, E. P. Menzel, F. Hocke, M. J. Schwarz, J. J. Garcia-Ripoll, D. Zueco, T. Hmmer, E. Solano, A. Marx, and R. Gross. *Circuit quantum electrodynamics in the ultrastrong-coupling regime.* Nature Physics **6**(10), 772 (2010).

[48] A. Wallraff, D. I. Schuster, A. Blais, L. Frunzio, R.-S. Huang, J. Majer, S. Kumar, S. M. Girvin, and R. J. Schoelkopf. *Strong coupling of a single photon to a superconducting qubit using circuit quantum electrodynamics.* Nature **431**(7005), 162 (2004).

[49] A. A. Abdumalikov, O. Astafiev, Y. Nakamura, Y. A. Pashkin, and J. Tsai. *Vacuum rabi splitting due to strong coupling of a flux qubit and a coplanar-waveguide resonator.* Physical Review B **78**(18), 180502 (2008).

[50] L. DiCarlo, J. M. Chow, J. M. Gambetta, L. S. Bishop, B. R. Johnson, D. I. Schuster, J. Majer, A. Blais, L. Frunzio, S. M. Girvin, and R. J. Schoelkopf. *Demonstration of two-qubit algorithms with a superconducting quantum processor.* Nature **460**(7252), 240 (2009).

[51] M. Neeley, R. C. Bialczak, M. Lenander, E. Lucero, M. Mariantoni, A. D. OConnell, D. Sank, H. Wang, M. Weides, J. Wenner, Y. Yin, T. Yamamoto, A. N. Cleland, and J. M. Martinis. *Generation of three-qubit entangled states using superconducting phase qubits.* Nature **467**(7315), 570 (2010).

[52] A. Fedorov, L. Steffen, M. Baur, M. P. da Silva, and A. Wallraff. *Implementation of a toffoli gate with superconducting circuits.* Nature **481**(7380), 170 (2012).

[53] L. DiCarlo, M. D. Reed, L. Sun, B. R. Johnson, J. M. Chow, J. M. Gambetta, L. Frunzio, S. M. Girvin, M. H. Devoret, and R. J. Schoelkopf. *Preparation and measurement of three-qubit entanglement in a superconducting circuit.* Nature **467**(7315), 574 (2010).

[54] M. Hofheinz, H. Wang, M. Ansmann, R. C. Bialczak, E. Lucero, M. Neeley, A. D. O'Connell, D. Sank, J. Wenner, J. M. Martinis, and A. N. Cleland. *Synthesizing arbitrary quantum states in a superconducting resonator.* Nature **459**(7246), 546 (2009).

[55] L. Steffen, Y. Salathe, M. Oppliger, P. Kurpiers, M. Baur, C. Lang, C. Eichler, G. Puebla-Hellmann, A. Fedorov, and A. Wallraff. *Deterministic quantum teleportation with feed-forward in a solid state system.* Nature **500**(7462), 319 (2013).

[56] M. Tavis and F. W. Cummings. *Exact solution for an n-moleculeradiation-field hamiltonian.* Phys. Rev. **170**(2), 379 (1968).

[57] D. Englund, B. Shields, K. Rivoire, F. Hatami, J. Vuckovic, H. Park, and M. D. Lukin. *Deterministic coupling of a single nitrogen vacancy center to a photonic crystal cavity.* Nano Letters **10**(10), 3922 (2010).

[58] K. Hennessy, A. Badolato, M. Winger, D. Gerace, M. Atatre, S. Gulde, S. Flt, E. L. Hu, and A. Imamolu. *Quantum nature of a strongly coupled single quantum dotcavity system.* Nature **445**(7130), 896 (2007).

[59] J. Wolters, A. W. Schell, G. Kewes, N. Nsse, M. Schoengen, H. Dscher, T. Hannappel, B. Lchel, M. Barth, and O. Benson. *Enhancement of the zero phonon line emission from a single nitrogen vacancy center in a nanodiamond via coupling to a photonic crystal cavity.* Applied Physics Letters **97**(14), 141108 (2010).

[60] A. Badolato, M. Winger, K. J. Hennessy, E. L. Hu, and A. Imamolu. *Cavity QED effects with single quantum dots.* Comptes Rendus Physique **9**(8), 850 (2008).

[61] M. Nomura, N. Kumagai, S. Iwamoto, Y. Ota, and Y. Arakawa. *Laser oscillation in a strongly coupled single-quantum-dotnanocavity system.* Nature Physics **6**(4), 279 (2010).

[62] J. Riedrich-Mller, L. Kipfstuhl, C. Hepp, E. Neu, C. Pauly, F. Mcklich, A. Baur, M. Wandt, S. Wolff, M. Fischer, S. Gsell, M. Schreck, and C. Becher. *One- and two-dimensional photonic crystal microcavities in single crystal diamond.* Nature Nanotechnology **7**(1), 69 (2012).

[63] G. Khitrova, H. M. Gibbs, M. Kira, S. W. Koch, and A. Scherer. *Vacuum rabi splitting in semiconductors.* Nature Physics **2**(2), 81 (2006).

[64] N. Le Thomas, U. Woggon, O. Schps, M. V. Artemyev, M. Kazes, and U. Banin. *Cavity QED with semiconductor nanocrystals.* Nano Letters **6**(3), 557 (2006).

[65] K. Srinivasan and O. Painter. *Linear and nonlinear optical spectroscopy of a strongly coupled microdiskquantum dot system.* Nature **450**(7171), 862 (2007).

[66] P. E. Barclay, K.-M. C. Fu, C. Santori, and R. G. Beausoleil. *Chip-based microcavities coupled to nitrogen-vacancy centers in single crystal diamond.* Applied Physics Letters **95**(19), 191115 (2009).

[67] T. Aoki, B. Dayan, E. Wilcut, W. P. Bowen, A. S. Parkins, T. J. Kippenberg, K. J. Vahala, and H. J. Kimble. *Observation of strong coupling between one atom and a monolithic microresonator.* Nature **443**(7112), 671 (2006).

[68] A. Faraon, P. E. Barclay, C. Santori, K.-M. C. Fu, and R. G. Beausoleil. *Resonant enhancement of the zero-phonon emission from a colour centre in a diamond cavity.* Nature Photonics **5**(5), 301 (2011).

[69] P. E. Barclay, K.-M. C. Fu, C. Santori, A. Faraon, and R. G. Beausoleil. *Hybrid nanocavity resonant enhancement of color center emission in diamond.* Physical Review X **1**(1), 011007 (2011).

[70] Y.-S. Park, A. K. Cook, and H. Wang. *Cavity QED with diamond nanocrystals and silica microspheres.* Nano Letters **6**(9), 2075 (2006).

[71] D. W. Vernooy, A. Furusawa, N. P. Georgiades, V. S. Ilchenko, and H. J. Kimble. *Cavity QED with high-q whispering gallery modes.* Physical Review A **57**(4), R2293 (1998).

[72] S. Gtzinger, L. de S Menezes, A. Mazzei, S. Khn, V. Sandoghdar, and O. Benson. *Controlled photon transfer between two individual nanoemitters via shared high-q modes of a microsphere resonator.* Nano Letters **6**(6), 1151 (2006).

[73] S. Schietinger and O. Benson. *Coupling single NV-centres to high-q whispering gallery modes of a preselected frequency-matched microresonator.* Journal of Physics B: Atomic, Molecular and Optical Physics **42**(11), 114001 (2009).

[74] S. Schietinger, T. Schrder, and O. Benson. *One-by-one coupling of single defect centers in nanodiamonds to high-q modes of an optical microresonator.* Nano Letters **8**(11), 3911 (2008).

[75] Y.-F. Xiao, Y.-C. Liu, B.-B. Li, Y.-L. Chen, Y. Li, and Q. Gong. *Strongly enhanced light-matter interaction in a hybrid photonic-plasmonic resonator.* Physical Review A **85**(3), 031805 (2012).

[76] X.-C. Yu, Y.-C. Liu, M.-Y. Yan, W.-L. Jin, and Y.-F. Xiao. *Coupling of diamond nanocrystals to a high-q whispering-gallery microresonator.* Physical Review A **86**(4), 043833 (2012).

[77] T. A. Brun and H. Wang. *Coupling nanocrystals to a high-q silica microsphere: Entanglement in quantum dots via photon exchange.* Physical Review A **61**(3), 032307 (2000).

[78] P.-B. Li, S.-Y. Gao, H.-R. Li, S.-L. Ma, and F.-L. Li. *Dissipative preparation of entangled states between two spatially separated nitrogen-vacancy centers.* Physical Review A **85**(4), 042306 (2012).

[79] W. Yang, Z. Xu, M. Feng, and J. Du. *Entanglement of separate nitrogen-vacancy centers coupled to a whispering-gallery mode cavity.* New Journal of Physics **12**(11), 113039 (2010).

[80] W. L. Yang, Z. Q. Yin, Z. Y. Xu, M. Feng, and J. F. Du. *One-step implementation of multiqubit conditional phase gating with nitrogen-vacancy centers coupled to a high-q silica microsphere cavity.* Applied Physics Letters **96**(24), 241113 (2010).

[81] P.-B. Li, S.-Y. Gao, and F.-L. Li. *Quantum-information transfer with nitrogen-vacancy centers coupled to a whispering-gallery microresonator.* Physical Review A **83**(5), 054306 (2011).

[82] M. L. Gorodetsky, A. A. Savchenkov, and V. S. Ilchenko. *Ultimate q of optical microsphere resonators.* Optics Letters **21**(7), 453 (1996).

[83] D. K. Armani, T. J. Kippenberg, S. M. Spillane, and K. J. Vahala. *Ultra-high-q toroid microcavity on a chip.* Nature **421**(6926), 925 (2003).

[84] C. Emary. *Dark-states in multi-mode multi-atom jaynes-cummings systems.* Journal of Physics B: Atomic, Molecular and Optical Physics **46**(22), 224008 (2013).

[85] T. Taneichi and T. Kobayashi. *Enhanced entanglement of two atoms confined in a multi-mode optical cavity.* Chemical Physics Letters **378**(56), 576 (2003).

[86] P. Strack and S. Sachdev. *Dicke quantum spin glass of atoms and photons.* Physical Review Letters **107**(27), 277202 (2011).

[87] A. Wickenbrock, M. Hemmerling, G. R. M. Robb, C. Emary, and F. Renzoni. *Collective strong coupling in multimode cavity QED.* Physical Review A **87**(4), 043817 (2013).

[88] C. Gerry and P. Knight. *Introductory Quantum Optics* (Cambridge University Press, 2005).

[89] H. Tanji. *Few-Photon Nonlinearity with an Atomic Ensemble in an Optical Cavity.* Ph.D. thesis, Harvard University (2011).

[90] E. T. J. Frederick Williams Cummings. *Comparison of quantum and semiclassical radiation theories with application to the beam maser.* IEEE Special Issue (1963).

[91] J. Gea-Banacloche. *Jaynes-cummings model with quasiclassical fields: The effect of dissipation.* Physical Review A **47**(3), 2221 (1993).

[92] O. Tsyplyatyev and D. Loss. *Classical and quantum regimes of the inhomogeneous dicke model and its ehrenfest time.* Phys. Rev. B **82**(2), 024305 (2010).

[93] J. Dalibard, Y. Castin, and K. Mlmer. *Wave-function approach to dissipative processes in quantum optics.* Phys. Rev. Lett. **68**(5), 580 (1992).

[94] A. N. Oraevsky. *Whispering-gallery waves.* Quantum Electron. **32**(5), 377 (2002).

[95] S. Schiller. *Asymptotic expansion of morphological resonance frequencies in mie scattering.* Applied Optics **32**(12), 2181 (1993).

[96] A. Mazzei. *Cavity enhanced optical processes in microsphere resonators.* Ph.D. thesis, Humboldt University (2007).

[97] V. B. Braginsky, M. L. Gorodetsky, and V. S. Ilchenko. *Quality-factor and nonlinear properties of optical whispering-gallery modes.* Physics Letters A **137**(78), 393 (1989).

[98] V. V. Klimov, V. S. Letokhov, and M. Ducloy. *Quantum theory of radiation of an excited atom placed near a microresonator containing a single-photon wavepacket: Photon correlation properties.* Laser Physics **17**(7), 912 (2007).

[99] S. M. Spillane, T. J. Kippenberg, K. J. Vahala, K. W. Goh, E. Wilcut, and H. J. Kimble. *Ultrahigh-q toroidal microresonators for cavity quantum electrodynamics.* Physical Review A **71**(1), 013817 (2005).

[100] C. Junge, D. OShea, J. Volz, and A. Rauschenbeutel. *Strong coupling between single atoms and nontransversal photons.* Phys. Rev. Lett. **110**(21), 213604 (2013).

[101] C. Phelan, T. Hennessy, and T. Busch. *Shaping the evanescent field of optical nanofibers for cold atom trapping.* Optics Express **21**(22), 27093 (2013).

[102] L. Guoping. *Fabrication and characterization of optical microcavities functionalized by rare-earth oxide nanocrystals: realization of a single-mode ultra-low threshold laser.* Ph.D. thesis, Xiamen University (2010).

[103] I. Grudin. *Crystalline Whispering Gallery Mode Resonators for Quantum and Nonlinear Optics.* Ph.D. thesis, California Institute of Technology (2008).

[104] M. A. Morrison and G. A. Parker. *A guide to rotations in quantum mechanics.* Aust. J. Phys. **40**(4), 465 (1987).

[105] J. T. Rubin and L. Deych. *On optical forces in spherical whispering gallery mode resonators.* Optics Express **19**(22), 22337 (2011).

[106] T. Junno, K. Deppert, L. Montelius, and L. Samuelson. *Controlled manipulation of nanoparticles with an atomic force microscope.* Applied Physics Letters **66**(26), 3627 (1995).

[107] A. Mazzei, S. Gtzinger, L. de S. Menezes, G. Zumofen, O. Benson, and V. Sandoghdar. *Controlled coupling of counterpropagating whispering-gallery modes by a single rayleigh scatterer: A classical problem in a quantum optical light.* Physical Review Letters **99**(17), 173603 (2007).

[108] R. Ma, A. Schliesser, P. Del'Haye, A. Dabirian, G. Anetsberger, and T. J. Kippenberg. *Radiation-pressure-driven vibrational modes in ultrahigh-q silica microspheres.* Optics Letters **32**(15), 2200 (2007).

[109] H.-Q. Zhao, M. Fujiwara, M. Okano, and S. Takeuchi. *Observation of 1.2-GHz linewidth of zero-phonon-line in photoluminescence spectra of nitrogen vacancy centers in nanodiamonds using a fabry-perot interferometer.* Optics Express **21**(24), 29679 (2013).

[110] D. P. DiVincenzo. *Quantum computation.* Science **270**(5234), 255 (1995).

[111] T. D. Ladd, F. Jelezko, R. Laflamme, Y. Nakamura, C. Monroe, and J. L. OBrien. *Quantum computers.* Nature **464**(7285), 45 (2010).

[112] M. Hillery, V. Buek, and A. Berthiaume. *Quantum secret sharing.* Physical Review A **59**(3), 1829 (1999).

[113] D. Leibfried, M. D. Barrett, T. Schaetz, J. Britton, J. Chiaverini, W. M. Itano, J. D. Jost, C. Langer, and D. J. Wineland. *Toward heisenberg-limited spectroscopy with multiparticle entangled states.* Science **304**(5676), 1476 (2004).

[114] E. J. OReilly and A. Olaya-Castro. *Non-classicality of the molecular vibrations assisting exciton energy transfer at room temperature.* Nature Communications **5** (2014).

[115] M. Arndt, T. Juffmann, and V. Vedral. *Quantum physics meets biology.* HFSP Journal **3**(6), 386 (2009).

[116] S. Nimmrichter and K. Hornberger. *Macroscopicity of mechanical quantum superposition states.* Physical Review Letters **110**(16), 160403 (2013).

[117] O. Carnal and J. Mlynek. *Youngs double-slit experiment with atoms: A simple atom interferometer.* Physical Review Letters **66**(21), 2689 (1991).

[118] M. Arndt, O. Nairz, J. Vos-Andreae, C. Keller, G. van der Zouw, and A. Zeilinger. *Waveparticle duality of c60 molecules.* Nature **401**(6754), 680 (1999).

[119] S. Gerlich, S. Eibenberger, M. Tomandl, S. Nimmrichter, K. Hornberger, P. J. Fagan, J. Txen, M. Mayor, and M. Arndt. *Quantum interference of large organic molecules.* Nature Communications **2**, 263 (2011).

[120] R. F. Voss and R. A. Webb. *Macroscopic quantum tunneling in 1-m nb josephson junctions.* Physical Review Letters **47**(4), 265 (1981).

[121] E. Hinds and R. Blatt. *NOBEL 2012 physics: Manipulating individual quantum systems.* Nature **492**(7427), 55 (2012).

[122] D. Leibfried, E. Knill, S. Seidelin, J. Britton, R. B. Blakestad, J. Chiaverini, D. B. Hume, W. M. Itano, J. D. Jost, C. Langer, R. Ozeri, R. Reichle, and D. J. Wineland. *Creation of a six-atom schrdinger cat state.* Nature **438**(7068), 639 (2005).

[123] Z. Zhao, Y.-A. Chen, A.-N. Zhang, T. Yang, H. J. Briegel, and J.-W. Pan. *Experimental demonstration of five-photon entanglement and open-destination teleportation.* Nature **430**(6995), 54 (2004).

[124] C. A. Sackett, D. Kielpinski, B. E. King, C. Langer, V. Meyer, C. J. Myatt, M. Rowe, Q. A. Turchette, W. M. Itano, D. J. Wineland, and C. Monroe. *Experimental entanglement of four particles.* Nature **404**(6775), 256 (2000).

[125] H. Hffner, W. Hnsel, C. F. Roos, J. Benhelm, D. Chek-al kar, M. Chwalla, T. Krber, U. D. Rapol, M. Riebe, P. O. Schmidt, C. Becher, O. Ghne, W. Dr, and R. Blatt. *Scalable multiparticle entanglement of trapped ions.* Nature **438**(7068), 643 (2005).

[126] J. D. Thompson, B. M. Zwickl, A. M. Jayich, F. Marquardt, S. M. Girvin, and J. G. E. Harris. *Strong dispersive coupling of a high-finesse cavity to a micromechanical membrane.* Nature **452**(7183), 72 (2008).

[127] T. P. Purdy, P.-L. Yu, R. W. Peterson, N. S. Kampel, and C. A. Regal. *Strong optomechanical squeezing of light.* Phys. Rev. X **3**(3), 031012 (2013).

[128] F. Brennecke, S. Ritter, T. Donner, and T. Esslinger. *Cavity optomechanics with a bose-einstein condensate.* Science **322**(5899), 235 (2008).

[129] H. Seok, L. F. Buchmann, E. M. Wright, and P. Meystre. *Multimode strong-coupling quantum optomechanics.* Physical Review A **88**(6) (2013).

[130] P. Kok, H. Lee, and J. P. Dowling. *Creation of large-photon-number path entanglement conditioned on photodetection.* Phys. Rev. A **65**(5), 052104 (2002).

[131] B. Yurke and D. Stoler. *Generating quantum mechanical superpositions of macroscopically distinguishable states via amplitude dispersion.* Physical Review Letters **57**(1), 13 (1986).

[132] J. P. Dowling. *Quantum optical metrology the lowdown on high-n00n states.* Contemporary Physics **49**(2), 125 (2008).

[133] A. Ourjoumtsev, F. Ferreyrol, R. Tualle-Brouri, and P. Grangier. *Preparation of nonlocal superpositions of quasi-classical light states.* Nat Phys **5**(3), 189 (2009).

[134] H. Vahlbruch, M. Mehmet, S. Chelkowski, B. Hage, A. Franzen, N. Lastzka, S. Goßler, K. Danzmann, and R. Schnabel. *Observation of squeezed light with 10-dB quantum-noise reduction.* Phys. Rev. Lett. **100**(3), 033602 (2008).

[135] M. Mehmet, H. Vahlbruch, N. Lastzka, K. Danzmann, and R. Schnabel. *Observation of squeezed states with strong photon-number oscillations.* Phys. Rev. A **81**(1), 013814 (2010).

[136] I. Afek, O. Ambar, and Y. Silberberg. *High-NOON states by mixing quantum and classical light.* Science **328**(5980), 879 (2010).

[137] D. F. James and J. Jerke. *Effective hamiltonian theory and its applications in quantum information.* Canadian Journal of Physics **85**(6), 625 (2007).

[138] A. Kenfack and K. Życzkowski. *Negativity of the wigner function as an indicator of non-classicality.* J. Opt. B: Quantum Semiclass. Opt. **6**(10), 396 (2004).

[139] J. Dobrindt. *Bio-sensing using toroidal microresonators and Theoretical cavity optomechanics.* Ph.D. thesis, University of Munich (2012).